EXTENDING THE POTENTIAL OF THIN-FILM OPTOELECTRONICS VIA OPTICAL ENGINEERING

by

Yida Lin

A dissertation submitted to The Johns Hopkins University in conformity
with the requirements for the degree of Doctor of Philosophy

Baltimore, Maryland
September 2020

Abstract

Optoelectronics based on nanomaterials have become a research focus in recent years, which bridge the fields of solid state physics, electrical engineering and materials science. The rapid development in optoelectronic devices in the last century has both benefited from and spurred advancements in the science and engineering of photon detection and manipulation, image sensing, high-efficiency light emission, displays, communications and renewable energy harvesting. A particularly promising material class for optoelectronics is the colloidal nanomaterials, thanks to their exotic properties in terms of light-matter interaction, low-dimensionality, and solution-processability which dramatically reduces the time and cost for device fabrication, and at the same time provides wide compatibility with existing interfaces and device structures. This thesis focuses on exploring and assessing the capabilities of lead sulfide quantum dot-based solar cells and photodetectors. The discussion involves advances in techniques such as implementing photonic structures, designing and building novel characterization systems and methods, and coupling to external optical structures and components.

This thesis comprises three sections. The first focuses on the design of photonic structures to tailor the response of photovoltaics or other absorption-based optoelectronics for specific applications. In the first part, we introduce the complete multi-layer thin film interference effects into the design of solar cells. By numerical calculation and optimization as well as the precise fabrication control, devices with specific target colors or optical transparencies were achieved. In the second part, we investigate the presence of

2D photonic crystal bands in absorbing materials that can be readily incorporated into nanomaterial thin films. We carried out simulations and theoretical analyses and proposed strategies for simultaneous selectivity in all optical spectra of the devices that are critical for optoelectronic applications.

The next section focuses on designing and building a multi-modal microscopy system for thin-film optoelectronic devices, accompanied with analyses and explanation of complex experimental data. The goal of the system is to provide simultaneous 2D spatial measurements of, including but not limited to, photoluminescence spectra, time-resolved photocurrent and photovoltage responses, and a rich variety of all the possible combinations of these measurements and their associated derived quantities, collected with micrometer resolution. The multi-dimensional data help us understand the intercorrelation between local defective regions in films and the entire device behavior, as well as a more comprehensive profile of mutual relationships between solar cell figures of merit.

In the last section, we discuss an implementation of miniature solar concentrator arrays for quantum dot solar cells. First, we design and analyze the effects of a lens-type concentrator made from polydimethylsiloxane, a flexible organosilicon polymer. The concentrators are optimized with the aid of ray-tracing simulations to achieve the best performance coupled with nanomaterial-based devices. Experimentally, we produce an concentrator system delivering 20-fold current and power enhancements close to the theoretical predictions. Our measurements also enables the explanation of rarely-explored carrier dynamics critical to the high-power operation schemes of thin film solar cells. Next, we design a wide-acceptance-angle dielectric solar concentrator that can be adapted to various of high-efficiency small-area solar cells. The design is generated based on rigorous ray-optical models, and is verified with optical simulations to deliver significant improvement over non-concentrated systems. To sum up, we discuss and assess the strategies for extending the possibilities of nanomaterial-based optoelectronics for future challenges in energy production and related applications.

Thesis Committee

Primary Readers

Dr. Susanna M. Thon (Primary Advisor)
Assistant Professor
Department of Electrical and Computer Engineering
Johns Hopkins University

Dr. Jacob B. Khurgin
Professor
Department of Electrical and Computer Engineering
Johns Hopkins University

Dr. Mark A. Foster
Associate Professor
Department of Electrical and Computer Engineering
Johns Hopkins University

Contents

List of Tables

List of Figures

Chapter 1

Introduction and Motivation

The field of modern optoelectronics began in the mid-20th century, thanks to advances in quantum mechanics and solid-state physics, and has undergone a tremendous and rapid development in the following decades. The discoveries and innovations in optoelectronics have transformed society and human lives via its three core functions: sourcing, detecting and controlling light. This is done in a wide variety of ways including energy harvesting, optical sensing, displays, image reproduction and so on. By just looking at modern cell phones, one will realize the omnipresence of optoelectronics: displays based on light-emitting diodes (LEDs),various near- infrared (NIR) emitters and sensors for distance sensing, vertical-cavity surface emitting lasers (VCSEL) [1–3] for 3D face recognition, a combination of high-resolution CMOS-based image sensors [4, 5] and more.

The successes in the field of optoelectronics were made possible largely due to major progress in related fields including physics, chemistry, materials science, electrical engineering and even computer science, and optoelectronics, in turn, facilitates important research in these fields, by providing technology and enhancements for experimentation, instrumentation, data visualization, data transfer and communications. Therefore, the field of optoelectronics will undoubtedly continue to be one of the most important and popular research focuses of the 21st century.

Despite rapid advances in science and technology, the sustainability of economic growth and societal development will always be the ultimate goal of these fields, and the key to achieving this goal lies in long-term consistent access to energy. The world's population has more than doubled from 1970 to 2019, and continues to grow at an annual rate of about 1.1% [6]. Meanwhile, the global gross domestic product (GDP, in units of 2010 trillion US dollars), although more subject to fluctuation, has grown from $19.2 in 1970 to $82.5 in 2018 [6]. Despite the dramatic shift of the global economy away from energy intensive industries, as well as the continuous efforts to improve energy efficiencies in the past few decades, which has significantly reduced the energy consumption per capita and per unit GDP, the total global energy use is projected to keep growing until at least 2040-2050 **Figure 1-1a**[7]. Given the fact that fossil fuels will eventually run out, as well as the widespread consensus that limiting carbon dioxide emissions is necessary to keep global temperature rises under control [8], renewable energy sources that do not involve the combustion of carbon will take on increasingly important roles in the foreseeable future.

Among all the types of renewable energy sources, solar energy is considered one of the most promising due to its advantages in availability, coverage, safety during operation, etc. The earth receives over 12 000 TW of solar power constantly. Even if only 0.5% of this amount can be utilized after land restrictions and conversion losses, the output would still be far beyond the forecast demand for 2040. **Figure 1-1b** [9] shows the past and predicted future power generation from various sources of energy from 1995 to 2050, displaying a clear accelerating trend of growth in renewable sources, with solar becoming the primary source by 2050, accounting for nearly 40% of the share as opposed to below 10% currently.

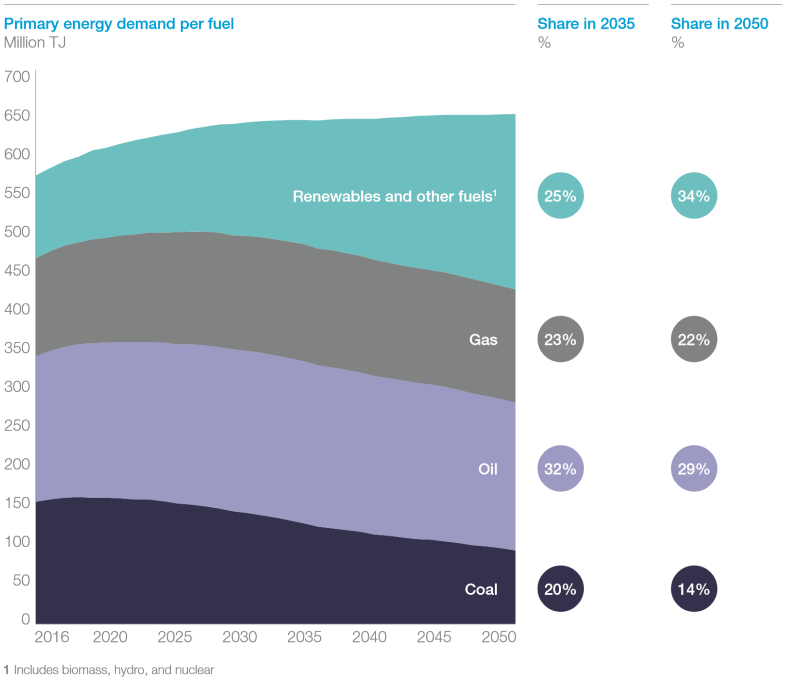

(a)

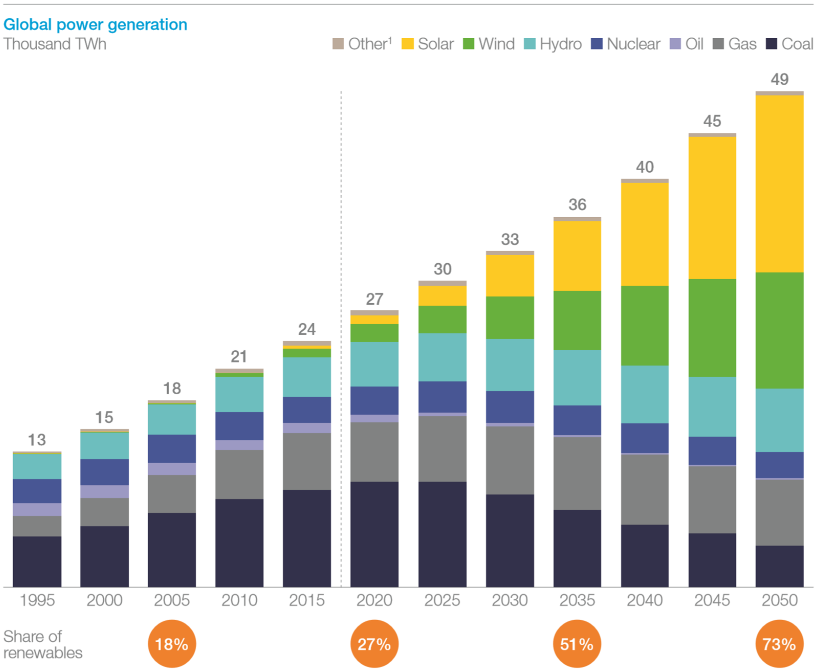

(b)

Figure 1-1. a. Global annual energy demand in millions of TJ projected to 2050[9]. **b.** Global power generation by various sources projected to 2050[7].

There are two main ways to utilize solar energy: solar thermal and photovoltaics

(PV). While the former presents an intuitive method for direct heat generation or heat generation followed by electricity generation using steam-propelled turbine systems, the latter serves as a much more direct method for electricity generation. PV overtook solar thermal in total installed capacity around 2017-2018, reaching almost 600 GW in 2019, and is estimated to at least double in the next decade, becoming the leading technology in a cleaner and more sustainable energy industry.

PV systems convert the radiation energy from the sun directly into electricity via excitation of electrons to form currents and voltages in a solar cell. The first practical solar cell was introduced in 1954 by Bell Labs, made of silicon, and converted about 6% of the sun's power to electrical power. Since then, the industry has experienced countless innovations which boosted the power conversion efficiencies (PCEs) by a factor of four in silicon-based cells and created many alternative material technologies with much lower manufacturing costs and new capabilities. The stability of crystalline silicon-based solar cells was also drastically improved, enabling wide-scale commercialization beginning in the 1980s. Solar cells today come in all kinds of materials, with III-V multi-junction cells providing over 46% PCE [10], crystalline silicon cells approaching their theoretical limit, and new generation materials offering other advantages such as flexibility and spectral tunability. However, in order to meet the goal of rapid expansion and popularization of PV technology in the near future, there are still many improvements to be made. For example, solar cells made of new materials with advantages in terms of mechanical flexibility and cost- effectiveness have yet to reach PCEs comparable to those of crystalline silicon.

In the meantime, solar cells, as a prototypical class of optoelectronic devices, have benefited from almost every major advance in the field of optoelectronics. Development in fabrication processes such as thin film deposition and micro- or nano-patterning, can be applied to a large variety of materials and structures implemented across different optoelectronic technologies. As another example, materials processing and chemical treatments that help reduce recombination centers in solar cell materials so as to improve open circuit voltage also produce higher sensitivity and lower noise in photodiode detectors, which are the most widely used devices for photosensing and imaging. Similarly, light emitting diodes (LED)s also share many properties and working principles with solar cells, especially considering that suppression of nonradiative recombination is a critical issue for both solar cells and LEDs. Additionally, longevity and long-term stability have become increasingly important as optoelectronics based on non-bulk-semiconductor materials, including organic and colloidal materials, have started to replace their traditional counterparts in consumer markets. A solution to any of these problems found for one type of device can potentially help clear the obstacles for the development and deployment of other types of optoelectronics.

Thus, research in the field of optoelectronics lays the foundation and paves the way to enhance and broaden the functionality in all technologies based on sensing, imaging, displays and communication, all of which are indispensable components that support a rapidly changing and progressing society. Optoelectronics research also aims to provide a means to a future powered with clean and sustainable energy in great abundance. This thesis focuses on seeking and exploring solutions to improve the performance of optoelectronic devices using optical engineering and photonics, including but not limited to engineering absorptivity and related spectral response tuning, as well as add-on optical structures for energy harvesting and photon detection. We also discuss ways to extend the characterization technologies available for probing devices under optical excitation. In this thesis, the majority of the studies are based on colloidal nanomaterials, which have seen increasing research interest in recent decades due to their promise in providing more economical, scalable and customizable manufacturing processes and eventually enabling fully flexible devices. Nonetheless, the ideas and conclusions from our work are also applicable to similar optoelectronics based on crystalline and non-crystalline semiconductor materials.

References

[1]C. Chang-Hasnain, “Tunable VCSEL,” IEEE Journal of Selected Topics in Quantum Electronics **6**, 978–987 (2000).

[2]R. Michalzik, “VCSEL Fundamentals,” in *VCSELs: Fundamentals, Technology and Applications of Vertical-Cavity Surface-Emitting Lasers*, edited by R. Michalzik, Springer Series in Optical Sciences (Springer, Berlin, Heidelberg, 2013), pp. 19–75.

[3]F. Koyama, “Recent Advances of VCSEL Photonics,” Journal of Lightwave Technology **24**, 4502–4513 (2006).

[4]A. El Gamal, “Trends in CMOS image sensor technology and design,” in Digest. International Electron Devices Meeting, (Dec. 2002), pp. 805–808.

[5]A. El Gamal and H. Eltoukhy, “CMOS image sensors,” IEEE Circuits and Devices Magazine **21**, 6–20 (2005).

[6]*World Bank Open Data* (The World Bank Troup).

[7]*Annual Energy Outlook 2020* (U.S Energy Information Administration, Jan. 2020).

[8]*The Paris Agreement | UNFCCC* (Nov. 2016).

[9]*Global Energy Perspective 2019: Reference Case* (McKinsey, Jan. 2019).

[10]M. A. Green, E. D. Dunlop, J. Hohl-Ebinger, M. Yoshita, N. Kopidakis, and A. W. Y. Ho-Baillie, “Solar cell efficiency tables (Version 55),” Progress in Photovoltaics: Research and Applications **28**, 3–15 (2020).

Chapter 2

Colloidal Quantum Dots and Optoelectronics

The concept of quantum-confined nanomaterials usually refers to solid-state materials formed from bulk crystalline materials that are significantly spatially confined in one, two, or all three dimensions. They are known accordingly as quantum wells, quantum wires or rods and quantum dots (QDs). This distinction and classification only make sense when the spatial confinement is strong enough such that the physical properties, especially those related to energy transitions and transport, are significantly modified. Although scientists have long been able to predict in detail the novel behaviors of systems on scales much smaller than the micron-level using standard quantum mechanics, practical physical structures or devices based on nanomaterials were difficult to realize without later developments in chemistry and materials engineering. For QDs, syntheses, processing and fabrication in the form of colloidal nanoparticles comprise a workflow of much lower cost, more versatility and relative ease of materials engineering compared to their bulk crystalline counterparts. This workflow also enables QDs to be integrated with existing structures and enables mass production for practical devices.

2.1 Physics of Colloidal Quantum Dots

The charge carriers, electrons and holes, are strongly spatially confined in all directions in QDs rather than possessing a continuous band of energy states where they can move freely across the material. This quantum confinement gives rise to their unique electronic and optical properties, and, for this to occur, the size of the QD must be significantly smaller than the Bohr exciton radius of the bulk material, which is given by $a = \frac{\hbar}{\mu c \alpha}\epsilon_r$, where μ, c, α and ϵ_r are the reduced carrier mass, the speed of light, the fine structure constant and the relative dielectric constant of the bulk material, respectively. Given that the Bohr radius of the hydrogen atom is 53 pm, it can be deduced that for a semiconductor material to satisfy this condition, it must simultaneously have a very large dielectric constant and small effective mass for at least one carrier type; otherwise the required size of the QD would be smaller than the volume of a few atoms. In this scenario, the crystal structure would not be maintained, and the materials physics would fail to be described by solid-state theories. For this reason, IV-VI lead chalcogenides including PbS, PbSe and PbTe become ideal candidates thanks to their ϵ_r in the range of ∼15-20 [1, 2], and lighter carrier masses below $0.1m_e$ [3, 4].

The simplest electronic model of a QD is based on effective mass theory[5], with the terminations of the crystal planes treated as infinite potential barriers enclosing the charge carriers. Thus solving the envelope function of the carrier wave function result in the allowed energy states above the original conduction or valence bandedges. Given the ideal spherical shape of a QD, and taking the electron as an example, the time-independent Helmholtz wave equations yield energy eigenvalues $E_n = \frac{\hbar^2 \eta_{n,l}^2}{2m_e a^2}$, where a is the radius of the sphere, and $\eta_{n,l}$ is the n^{th} zero of the spherical Bessel function of l^{th} order ($j_l(x)$). The lowest energy levels are therefore taken with the smallest values of $\eta_{n,l}^2$: π^2 (1S), 4.5^2 (1P), 5.8^2 (1D), $4\pi^2$, (2S), etc., with S,P,D, ... denoting the conventional angular momentum number l.

For holes, the energies are calculated accordingly using the hole effective mass, and are then subtracted from the valence band edge. As a result, the band gap (E_g) of the QD system, is now the smallest optical transition energy, which is the bulk E_g plus the additional confinement energies for electron and holes. Thus a wide E_g tuning range can be achieved by making the QDs sufficiently small. This effect is depicted in **Figure 2-1**. For PbS with a bulk E_g of 0.41eV, which has long been used as a photodetection material for the mid-infrared range, the corresponding QDs have band gap energies that can be reliably tuned from approximately 0.7 to 1.6 eV, enabling their use in optoelectronics suitable for the visible and near-infrared (NIR) ranges, including solar energy harvesting.

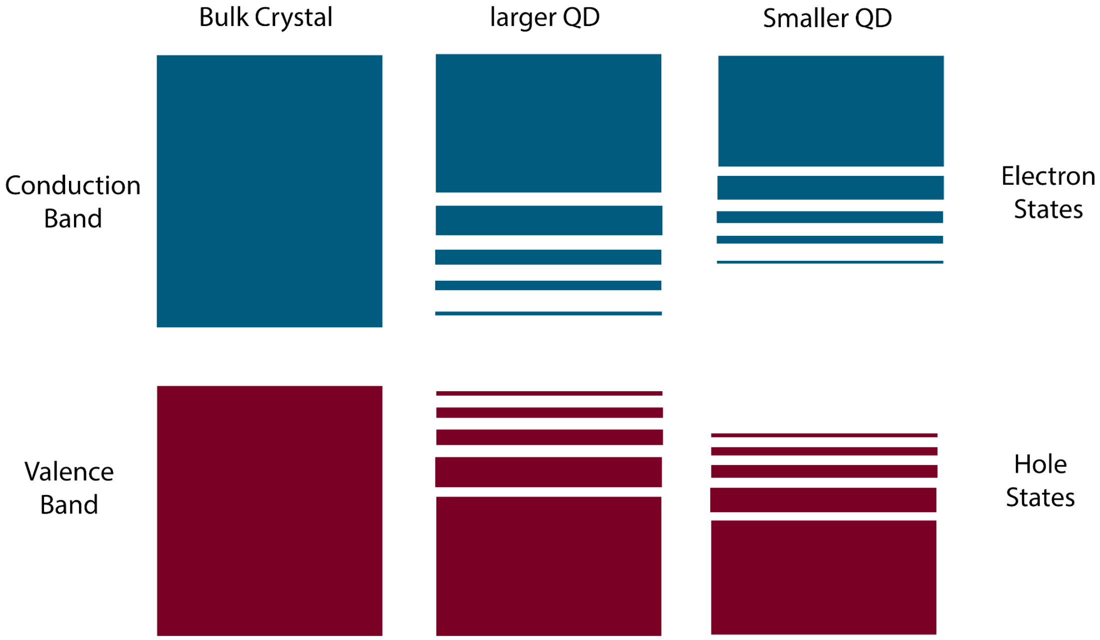

Figure 2-1. Quantum confinement effect illustrated for quantum dots of varying sizes. The blue and magenta shades indicate allowed conduction and band valence states, respectively, while the closest distance between them in each case defines the bandgap E_g.

If the electrostatic attraction between the electron and hole is taken into account, the total energy of the system will be lowered due to the last term in the following equation, known as the Brus equation[6]

$$E_g = \frac{\hbar^2\pi^2}{2a^2}\left(\frac{1}{m_e}+\frac{1}{m_h}\right) - \frac{1.786e^2}{4\pi\epsilon_0\epsilon_r a} \tag{2.1}$$

This equation is still not accurate enough to account for the majority of types of QDs used in optoelectronics. For II-VI cadmium chalcogenides such as CdS and CdSe QDs, the prerequisite that the QD sizes have to be much smaller than the Bohr exciton radius (widely known as the ”strong confinement” regime), is hard to satisfy, necessitating a larger contribution from additional correction terms including exchange and correlation energies [6]. Therefore, PbS and PbSe are considered as close-to-ideal materials for strong confinement regime. However, even for PbS and PbSe, the deviation from parabolic bandedges for these two materials, i.e., the deviation from the basic effective mass approximation, yields overestimation of the confinement energies themselves[7, 8]. The situation is even more complicated if the coupling Hamiltonian of 4 equivalent L valleys at the bulk bandedges is considered, leading to different effective masses along different directions of motion and the unavoidable spin-orbital interactions in PbS and PbSe [9]. A more comprehensive model has been proposed to account for most of these factors, involving interactions between four bandedge states with spin-orbital coupling take into account[10], which provides much more accurate predictions of the 1st and 2nd exciton energies for PbS and PbSe QDs of diameters from 2 to 14 nm.

The discrete energy levels give rise to optical transitions that directly lead to features in the form of exciton peaks in absorption and photoluminescence (PL) spectra. **Figure 2-2** shows the absorbance spectra for various sizes of PbS QDs. The broadening of the exciton peak features is largely caused by the size distribution of the QD ensemble, known as inhomogeneous broadening. Meanwhile, homogeneous broadening arises from electron-phonon coupling and transitions between various vibrational states [11–13] but was shown to have minimal effect on the width of the exciton peaks in colloidal QD

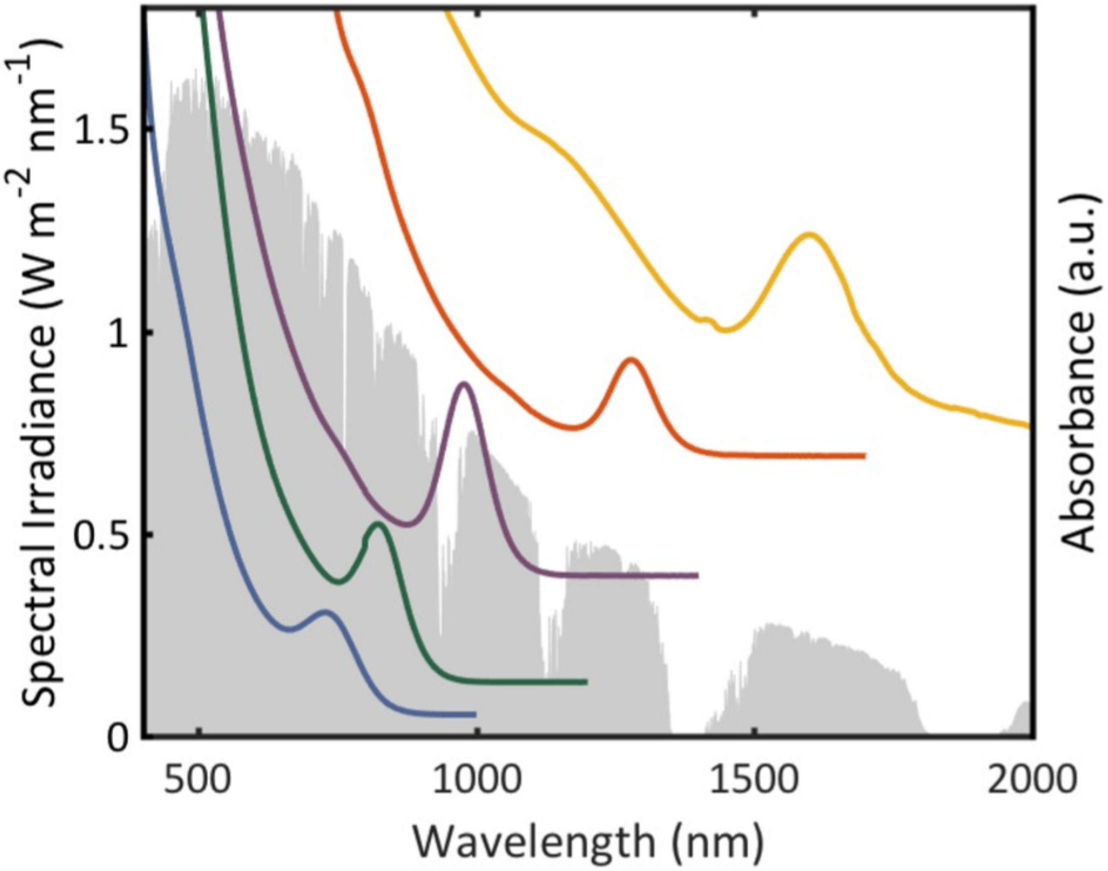

Figure 2-2. PbS CQD Absorbance Spectra of PbS CQDs in solution phase, with exciton peaks at wavelengths of 730, 820, 980, 1280 and 1600 nm. Spectra are offset for clarity. Additionally, the AM1.5 Global Horizontal Irradiance solar spectra is plotted.

ensembles. The increasing background in the absorption spectra is believed to be a result of a much higher chance of scattering and more allowed transitions to nearby states with increasing energy, approaching a band-like continuum as in bulk semiconductors [14]. Interestingly, it has been shown[15], for excitation energy much higher than E_g (in the case of PbS, $> 2\,5$eV), the absorption spectra, which consists of only the continuous background, overlap almost completely in terms of shape, regardless of the size of the QDs. The molar extinction coefficient is found to be proportional to the volume of the QD, which leads to a constant absorption coefficient at higher energies independent of sizes, if the QDs are assumed to occupy the entire space [14]. This finding justifies the use of QDs for optoelectronics relying on absorption and emission, as the material usage should be comparable to those based on bulk semiconductors for similar purposes with high energy photons.

Just as in bulk semiconductors, the excited states in QDs upon absorption of photons with energy higher than E_g, are only meta-stable and carriers will undergo various processes to relax to their band edges, before subsequent interband recombination occurs. In the early years of QD research, it was believed that hot carriers could be effectively maintained because the discretization of energies in quantum confined nanostructures would inhibit relaxation via phonon scattering [16, 17]. However, later experimental observations confirmed that relaxation of hot carriers still occurs at very high rates, though usually via different pathways than in bulk semiconductors[18, 19]. This reduces the chance to utilize the energy from hot carriers in optoelectronics. On the other hand, similar mechanisms could be responsible facilitating much more efficient multiple exciton generation (MEG) processes than in bulk semiconductors [20–22], where more than one electron-hole pair are generated upon absorption of a single high energy photon (usually $> 3E_g$), which could potentially lead to useful current multiplication in photodetectors and solar cells.

2.2 Synthesis, ligand exchange and surface modification of PbS Quantum Dots

There are many complex factors affecting the properties of individual QDs and QD assemblies. These include the nature of being physically isolated, as well as the existence of surfaces in both large quantities and areas for a given volume of QDs. Even the earliest physical models for QDs predict a strong energy dependence on their surfaces and surrounding media [6]. Therefore, the properties of QD assemblies and the performance of related devices rely heavily on the exact processes through which the QDs are created, modified and assembled. In fact, in the last decade, most of the efforts in the field of QD optoelectronics have been dedicated to the discovery and invention of synthesis, treatment and deposition methods that reliably, consistently, tunably and scalably provide QD materials with high performance and excellent stability with regards to different properties of interest.

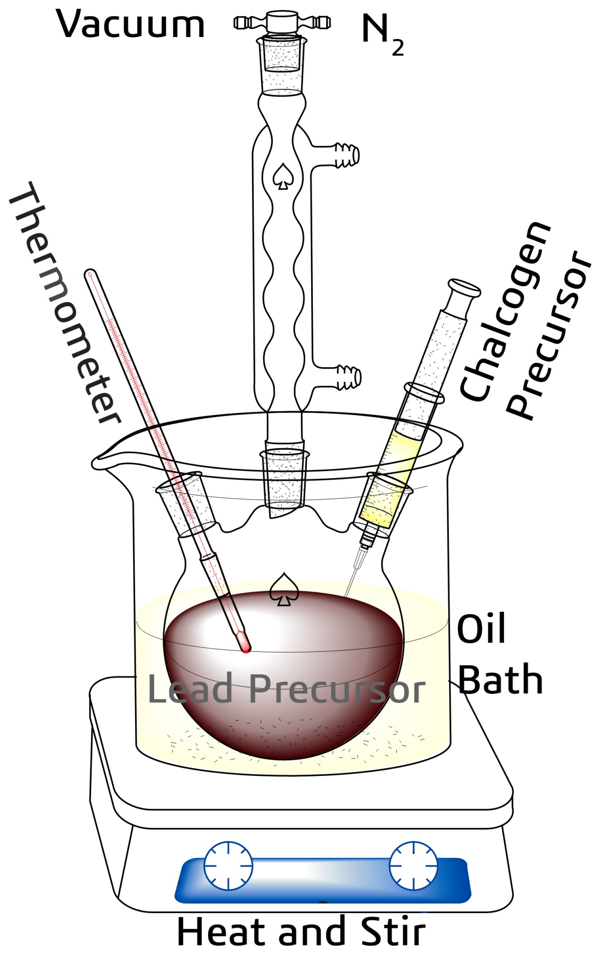

Figure 2-3. The setup for synthesizing PbS/PbSe QDs in laboratories. A three-neck flask is connected to a Schlenk line to be placed under vacuum or inert environment when needed. The heating of the lead precursor is monitored and controlled in a closed-loop cycle. The chalcogen precursor is injected once the lead solution is stabilized at the target temperature

The syntheses of PbS and PbSe CQDs usually follow a ”bottom-up” route[23], in which the QDs are grown from atomic and molecular precursors dispersed uniformly in a solvent medium. Specifically [24], the precursors containing lead cations are dissolved in a temperature-controlled coordinating solvent, and the chalcogenide reagent is rapidly injected into the heated mixture, starting the nucleation of the QDs. The particle growth following nucleation is uniform providing that the mixture is vigorously stirred, and growth becomes slower as the particle size increases. The concentration of the precursors is kept below the threshold to prevent further nucleation. Concurrently, remaining small nuclei are dissolved and added to the growth of larger particles in a process known as Ostwald ripening [25], which further helps control the particle size distribution. This type of synthesis method is usually referred to as a ”hot injection” method, owing to the high temperature at which the chalcogenide precursor injection occurs.

The exact configurations and conditions to make PbS CQDs have been studied and improved extensively. PbS CQD synthesis methods primarily fall into two categories, the Hines[26] approach and the Cademartiri [27] approach. The Hines method is based on a reaction between lead oleate and bis(trimethylsilyl)-sulfide (or hexamethyldisilathiane) (TMS_2S) dissolved in octadecene (ODE) as the sulfur precursor. The Cadematiri method employs lead(II) chloride and elemental sulfur dissolved in oleylamine as the precursors, with optional tri-n-octylphosphine (TOP) as a controlling agent[28]. Both methods follow the aforementioned principles of synthesis and are able to achieve PbS CQDs with high monodispersity (size variation of <10%). While the Cadematiri method produces slightly more air-stable samples, the Hines method is more common in synthesizing smaller QDs with $E_g > 1\,\text{eV}$, suitable for solar cells and short-wavelength photodetectors. A schematic of the setup for PbS/PbSe synthesis is depicted in **Figure 2-3**

The average sizes of the CQDs are determined by control over the concentrations of the precursors, the temperature at which the nucleation is initiated, and the dynamics of the subsequent cooling process. For the Hines method, it has been found [29] that by controlling the temperature and the concentration of oleic acid (OA) alone, QDs with sizes corresponding to absorption peaks from 900 nm to 2300 nm can be reliably obtained.

Forced termination of the growth by active cooling may be required to achieve PbS QDs of even smaller sizes. Also, the methods have been proven to be scalable with high yield, laying the foundation for energy-tunable optoelectronics based on PbS CQDs.

PbS and PbSe QDs are dispersed in a nonpolar solvent immediately after synthesis, usually toluene, octane or hexane. The suspension can remain chemically stable up to several months, thanks to the long-chain ligand passivation of the CQD surfaces. OA is the most common ligand, and is sourced from the precursors. The CQD solution can be deposited into thin-film solids which exhibit signatures of quantum confinement in their optical spectra; however, the long and insulating surface ligands almost completely prevent carrier transport in the film phase that is crucial for the operation of all optoelectronics. Therefore, performing a ligand exchange by replacing the OA chains with much shorter linker molecules becomes a necessary process during device fabrication. Other than enhancing the carrier transport properties, ligand exchanges can also dramatically modify the doping density of the CQD films, as well as shift their overall energy levels [30], providing a wide variety of possibilities to form semiconductor heterojunctions.

PbS and PbSe QDs have been shown to be highly non-stoichiometric, with Pb-rich surfaces that can reach Pb:S ratios of over 1.30[15]. This large imbalance requires surface Pb atoms to be passivated with anionic functional groups to avoid the formation of excessive surface trap states detrimental to the energy and carrier transport processes within the QD film. The first few generations of PbS QD-based optoelectronic devices utilized bidentate thiols[31], and mercaptocarboxylic acids [32], Ethanedithiol (EDT) and mercaptopropionic acid (MPA) were the most commonly used for QD solar cells, given the strong binding between Pb and S atoms as well as the short inter- dot distances they enabled to facilitate charge transport. Mercaptocarboxylic acids of different lengths have also been used to modulate the inter-dot distances to achieve a balance between efficient charge transport and reduced rates of exciton dissociation to maximize the efficiency of radiative recombination in QD LEDs [33].

Later improvements in surface passivation and carrier mobility were achieved by employing atomic halide ligands (Cl^-,Br^-,I^-,etc.) [34, 35] and passivation of exposed unsaturated anions by Cd . These strategies led to QD assemblies with better surface qualities and higher mobilities. They were also used to create films that were more n-type in character compared to the materials resulting from traditional organic-ligand treatments[30], making it possible to form more controllable full p-n or p-i-n architectures and considerably improving device PCE and stability. These methods were originally implemented using a layer-by-layer (LBL) solid-state exchange process, in which a QD thin films was deposited, then treated by reacting it with a solution containing the replacement ligand, and then the original ligands were washed away using a solvent treatment. This process was then repeated several times to build up a film of desired thickness.

In recent years, more advanced techniques [36, 37] have been developed that initiate the ligand exchange with halides entirely in the solution-phase, succeeded by a series of phase-transfer-assisted purification steps, which guarantee more thorough surface reactions and removal of unwanted materials. The resulting CQD ”ink” enables the use of a single-step process to finish the CQD deposition during device fabrication, which significantly reduces the non-uniformity and excessive ligand stripping that can be the result of LBL processes.

CQD surface modification via ligand exchange has become one of the main focuses in PbS CQD optoelectronics research due to the impact that the CQD surfaces have on device operation. The development of new ligand exchange strategies has been the leading factor in creating the CQD solar cells with the highest efficiencies to date.

2.3 Photovoltaics and Photodetectors

2.3.1 Fundamental Efficiency Limit of Photovoltaics

Solar cell operate via photovoltaic effect, which describes the conversion of absorbed photon flux to energetic charge carriers that power external circuits, in the form of sustained currents at non-zero voltages. Modern photovoltaics devices utilize semiconductor materials, in which only charge carriers with energies greater than the bandgap E_g, can be excited . The number of excited electron-hole pairs is, at most, the same number of absorbed photons (neglecting MEG and other nonlinear effects). These pairs are also known as excitons, and they carry energies of, at most, close to but less than E_g. These final energies are arrived at after an initial energy relaxation (thermalization) phase, which occurs much more quickly than any subsequent processes in most systems. In fact, the useful portion of the energy, the Gibbs free energy, is even smaller than E_g. Inside semiconductors, free energies carried by excitons can be represented as the difference between their chemical potentials, $\eta = \mu_e - \mu_h$, which, in turn, is equal to the effective photovoltage across the semiconductor in the best-case scenario. The power supplied to the external circuit is therefore, in theory, the product of photocurrent and the free energy of excitons: $P = J_{\text{ph}}\eta = J_{\text{ph}}(\mu_e - \mu_h)$.

The photocurrent is determined by the absorbed photon flux and the chemical potential difference $\mu_e - \mu_h$. In the best case, all incident photons with energy larger than E_g contribute an equal amount of photocurrent:

$$J_{\text{ph}} = q \int_0^\infty a(\omega) j_{\text{sol}}(\omega) d\omega \tag{2.2}$$

where $a(\omega)$ is the material absorptivity, and $j_{\text{sol}}(\omega)$ is the spectral photon number flux density. However, loss in the form of radiative recombination that causes exciton loss via emission of photons back to the environment must be included, at minimum. The recombination current follows the generalized Planck's law of radiation [38]:

$$J_{\text{rad}} = q \int_0^\infty \frac{\Omega}{4\pi^3 c^2} a(\omega) \frac{\omega^2 d\omega}{\exp\left(\frac{\hbar\omega - \eta}{kT}\right) - 1} \tag{2.3}$$

where Ω is the solid angle into which the photons are emitted, and c is the speed of light inside the material. To simplify, the absorptivity $a(\omega)$ can be taken as unity for $\hbar\omega > E_g$ for a sufficiently thick material. Therefore, one can estimate the optimal power output and PCE from a device without further knowledge of the exact physical structure as,

$$P_{\text{out}} = \left(J_{\text{ph}} - J_{\text{rad}}\right) V = \left(J_{\text{ph}} - J_{\text{rad}}\right) \frac{\eta}{q} \tag{2.4a}$$

$$P_{\text{in}} = \int_0^\infty j_{\text{sol}}(\omega)\hbar\omega d\omega \tag{2.4b}$$

and $PCE = P_{\text{in}}/P_{\text{out}}$. This set of equations yields the theoretical efficiency limit of a single bandgap absorber solar cell, known as the Shockley-Quiesser limit[39]. The maximum efficiency is hence a function of E_g only and can be calculated given the exact spectral photon flux density received on the earth from the sun. In **Figure 2-4**, we show the maximum PCE curve for different E_gs, based on the AM1.5 global normal irradiance spectrum. The best efficiency 33.7% is achieved with $E_g = 1.34eV$, close to the bandgap of GaAs. Due to the nature of the solar spectrum, materials with E_gs from approximately 1.1 to 1.5 eV can all achieve similar results.

For a single junction solar cell, i.e., a solar cell made from a material with a single bandgap, the primary losses come from two sources: the inability to absorb photons less energetic than E_g, and the loss of energy in excess of E_g from thermalization of carriers. The losses can be addressed if multiple materials with different E_gs are employed, so that higher-energy photons are absorbed by the higher E_g material, leaving lower-energy photons to be absorbed in the underlying lower E_g material. In this way, thermalization

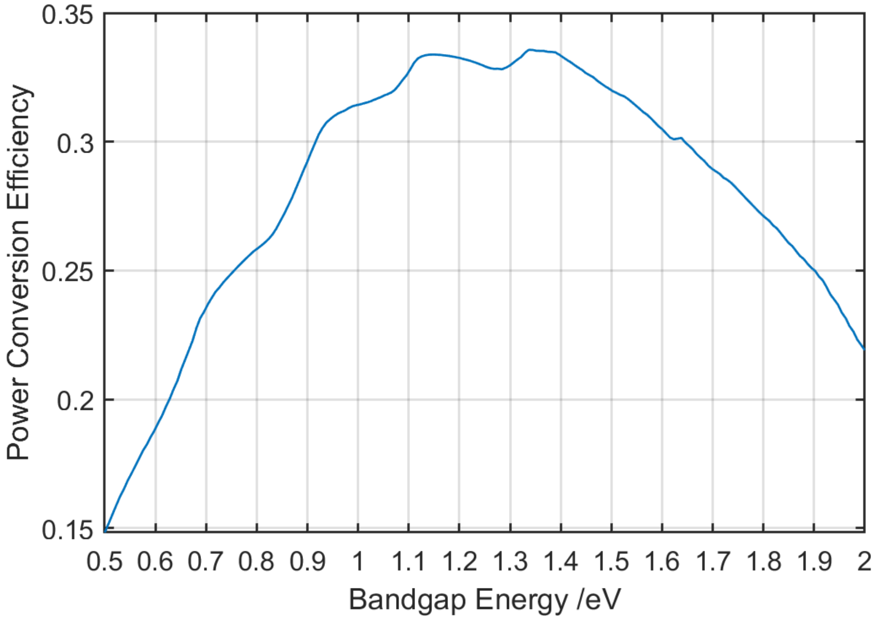

Figure 2-4. Theoretical power conversion efficiencies limits of single-junction solar cells as a function of bandgap energy under the AM1.5 Global Horizontal Irradiance spectrum.

losses can also be simultaneously reduced.

The other theoretical factor affecting the efficiency is the solid angle from which the material absorbs the solar power. The sun subtends a solid angle of 6.8×10^{-5}, while the absorber is usually considered to emit over the maximum possible solid angle π. If the solid angle that the absorber receives energy from can be extended to match the emission solid angle, which is called the ”maximum concentration” condition, the PCE can be further improved. Calculations[40] show that the efficiency limit for 2, 3 and 4-junction solar cells are 42% (55%), 49% (63%), 53% (68%), respectively, with the limits under maximum concentration given in the parentheses. Eventually, if the a series of absorbers with very small differences in their E_gs are stacked in a way such that each layer only absorbs photons with energies just above its bandgap energy, thus eliminating the thermalization losses, and if the number of such absorbers approaches infinity so that the entire incident spectrum is covered, the theoretical maximum PCE of a multi-junction solar cell under maximum concentration can reach 86%[40, 41]. This scenario is then equivalent to the thermodynamic limit, which treats the solar cell as a heat engine that receives heat flow from the sun, less the emission back to the sun, to be converted to work as a Carnot engine. The efficiency is therefore:

$$PCE = \left(1 - \frac{\Omega_{\text{emis}} T_A^4}{\Omega_{\text{abs}} T_S^4}\right)\left(1 - \frac{T_0}{T_A}\right) \tag{2.5}$$

With $\Omega_{\text{emis}} = \Omega_{\text{abs}}$, the maximum efficiency is achieved at 2480K when the sun is treated as a 5800K black body.

In practice, besides the fundamental factors causing efficiency loss described above, photovoltaic devices are inevitably subject to other loss mechanisms. These include sub-optimal absorptivity near E_g, additional recombination processes due to electronic trap states and the existence of surfaces and interfaces, accumulated loss of chemical potential η at the electrodes due to contact resistance. Addressing these issues has been the strongest driving force in the field.

2.3.2 Operation of Semiconductor p-n Junctions

Almost all semiconductor devices function based on single or multiple p-n junctions. For solar cells and photodiode-type photodetectors, p-n junctions are the core principle of operation. The electronic responses generated across the p-n junctions upon receiving light signals are the keys to realizing device functions. P-n junctions are formed when semiconductor materials with different Fermi levels, usually resulting from opposite-type doping, are placed in contact. If the two materials share a bandgap, electron affinity and ionization energy, a homojunction is formed with smooth spatial transitions in all energy levels. Otherwise, heterojunctions are formed with offsets in E_c and E_v that depend on the isolation values in the two materials. To balance the electrochemical potential or the E_F difference, carriers will redistribute, with electrons flowing into the p-type material from the n-type material, and vice versa. In this way, regions depleted of their majority carriers are formed on both sides of the junction, and become oppositely charged.

As a lowest-order approximation, the depletion region can be considered to carry a uniform charge density up to a certain distance from the junction. In **Figure 2-5a**, a p-n homojunction without any bias or illumination is illustrated; the widths of the depletion regions on the n- and p-side of the junction are marked as x_p and x_n, respectively. The electric field strength as well as the potential gradient across the junction can be calculated from Poisson's equation in the material $\nabla^2\Phi = -\frac{\varrho}{\epsilon}$, where Φ is the electrostatic potential and $\mathbf{E} = -\nabla\Phi$ is the electric field. The widths of the depletion regions, the total charge and the total potential difference across the junction can then be solved for a one-dimensional junction [42, 43]:

$$x_p = \left[\frac{2\epsilon}{e}\frac{N_D V_{\text{bi}}}{N_A(N_A+N_D)}\right]^{1/2} \tag{2.6a}$$

$$x_n = \left[\frac{2\epsilon}{e}\frac{N_A V_{\text{bi}}}{N_D(N_A+N_D)}\right]^{1/2} \tag{2.6b}$$

$$W = x_p + x_n = \left[\frac{2\epsilon V_{\text{bi}}}{e}\frac{N_D+N_A}{N_A N_D}\right]^{1/2} \tag{2.6c}$$

$$Q_p = Q_n = \left[2e\epsilon V_{\text{bi}}\frac{N_A N_D}{N_A+N_D}\right]^{1/2} \tag{2.6d}$$

where W is the total width of the depletion region and Q denotes the charge on each side. V_{bi} is the built-in potential that depends only on the relative doping difference across the junction, and can be written as $V_{\text{bi}} = E_{\text{fe}} - E_{\text{fh}}$, when two sides of the junction are separate. It can be seen from **Equation 2.6** that the depletion region on the side with the lower doping magnitude is wider. Since doping densities usually differ by orders of magnitudes in practice, creating a junction from a minimally-doped material and a heavily doped material can result in a depletion region that spans almost the entire width of the lower-doped material.

The regions outside of the depletion region are almost free of any net charge and have constant (flat) energy levels. These regions are called the quasi-neutral regions.

When a forward bias is applied to the junction, the chemical potential on the n-side, E_{fe} is raised with respect to E_{fh} on the p-side. When the bias is not too large, the net effect of the applied bias can be treated as a reduced V_{bi}, with depletion widths x_n, x_p and net charge changed accordingly. This is shown in **Figure 2-5b**. The depletion region width as well as the potential are both decreased. Under illuminated forward bias, the Fermi levels for electrons and holes separate within a certain distance from the junction, which causes an increased recombination rate that outpaces the steady-state generation rate from background radiation. This causes a gradual change in both current components due to the universal relation $\nabla \cdot \mathbf{J_s} + \frac{\partial s}{\partial t} = G_s - R_s$, with $s \in \{e, h\}$ assuming that the time derivative of the carrier concentrations vanishes in steady-state conditions. This allows us to calculate the contribution to the total current from the quasi- neutral regions.

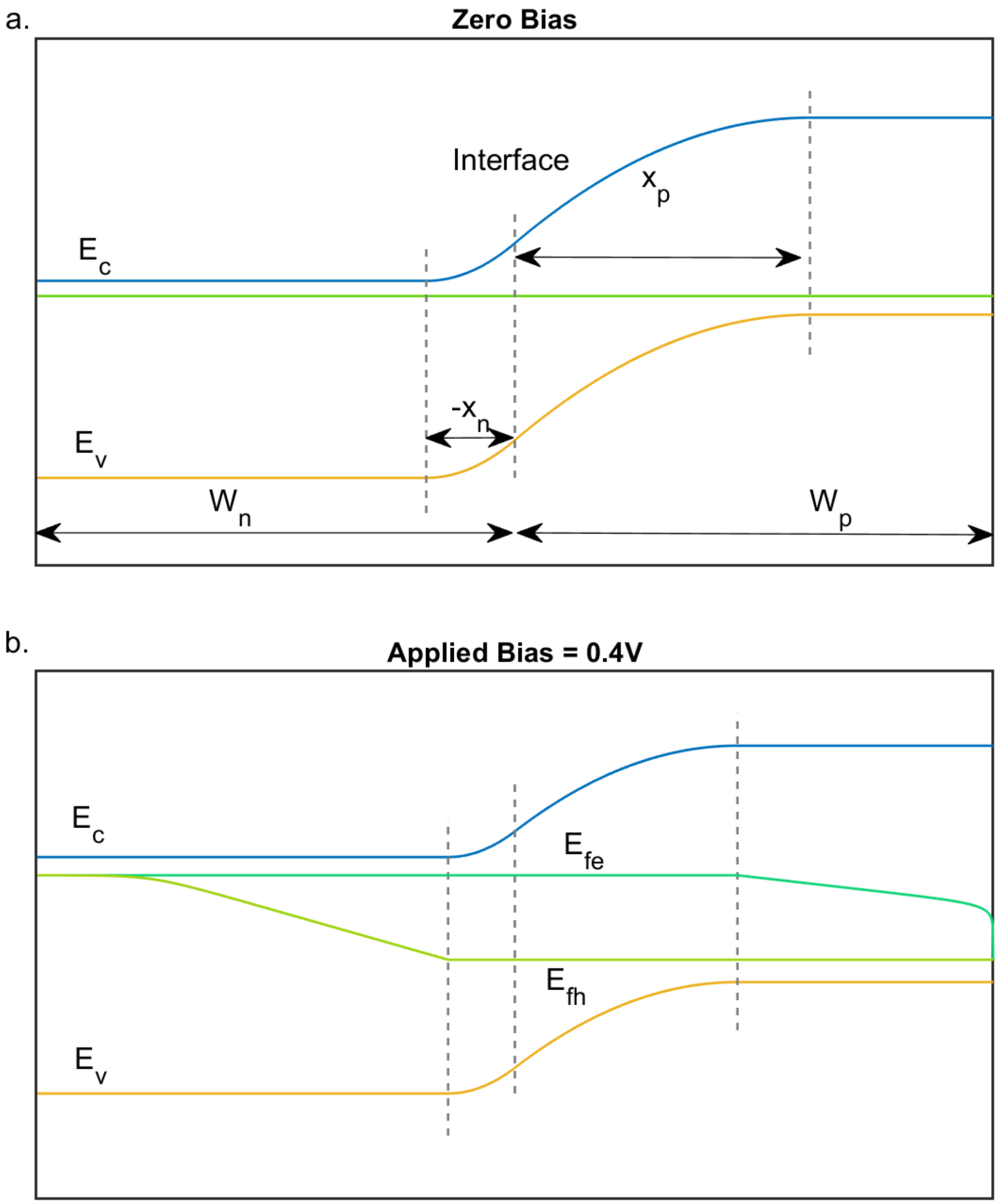

Figure 2-5. Example Band diagrams of p-n homojunctions.**a.**Equilibrium band diagram (no bias). **b.**The same junction under a forward bias of 0.4 V

The recombination of carriers can in most cases be express as $R = B \cdot np$ with the net recombination rate being $R - G_0 = B \cdot (np - n_0 p_0)$. In the quasi-neutral regions, the majority carrier concentration is almost unchanged while the minority carrier concentration undergoes a modulation of several orders of magnitudes. Taking the electron as an example, this gives: $R - G_0 = B \cdot (n - n_0)p_0 = \frac{n-n_0}{\tau_e}$, i.e., the recombination rate is linear in the excess minority carrier concentration, where τ_e is the minority carrier lifetime.

Currents in semiconductors can be decomposed into two types, $\mathbf{J}_{\text{s,diff}} = -D_s \nabla s$, the diffusion current driven by concentration gradients, and $\mathbf{J}_{\text{s,drift}} = \mu_s e s \mathbf{E}$, the drift current driven by any electric fields. The diffusion coefficient and mobility are denoted as D_s and μ_s, respectively. The electric field can be neglected in the quasi- neutral regions. Again, from continuity equation for electrons, we get:

$$\nabla \cdot \mathbf{J_e} = -D_e \nabla^2 n = G_s - R_s = -\frac{n - n_0}{\tau_e} \tag{2.7}$$

For electrons, the concentration just outside the depletion region on the p-side is given by $n = n_0 \exp\left(\frac{eV}{kT}\right)$, and at the end of the p-type material is n_0. The excess concentration and current density is therefore (the vectorial current can be now be expressed as its component in the x direction only):

$$n - n_0 = n_0 \frac{\sinh\left(\frac{W_p - x}{L_e}\right)}{\sinh\left(\frac{W_p - x_p}{L_e}\right)} \left[\exp\left(\frac{eV}{kT}\right) - 1\right] \tag{2.8a}$$

$$J_e = -\frac{D_e}{L_e} \frac{n_i^2}{N_A} \frac{\cosh\left(\frac{W_p - x}{L_e}\right)}{\sinh\left(\frac{W_p - x_p}{L_e}\right)} \left[\exp\left(\frac{eV}{kT}\right) - 1\right] \tag{2.8b}$$

where we have assigned: $L_e = \sqrt{D_e \tau_e}$ as the electron diffusion length in the p-type material. Also, we can substitute the zero-bias electron concentration $n_0 = \frac{n_i^2}{N_A}$. The minority carrier current due to holes on the n-side can be derived in an analogous fashion. If the recombination and associated current change are ignored for now, the total electrical current, which should be constant throughout the device is:

$$\begin{aligned} j_{T0} =& eJ_h(-x_n) - eJ_e(x_p) \\ =& en_i^2 \left[\frac{D_h}{L_h N_D} \coth\left(\frac{W_n - x_n}{L_h}\right) + \frac{D_e}{L_e N_A} \coth\left(\frac{W_p - x_p}{L_e}\right) \right] \left[\exp\left(\frac{eV}{kT}\right) - 1 \right] \end{aligned} \tag{2.9}$$

This relation holds for both forward and reverse bias as long as the forward bias does not perturb the band levels too much beyond the level shown in **Figure 2-5b**. It is evident that the well-established component $\exp\left({}^{eV}/_{kT}\right) - 1$ arises primarily from the known minority carrier concentration at the boundary of the depletion region and the linear dependence of the recombination rate. If these conditions are not met, adjustments are needed. For example, we can consider Shockley-Read-Hall or trap-assisted recombination of the form:

$$R - G = \frac{np - n_i^2}{\tau_p(n + n') + \tau_n(p + p')} \tag{2.10}$$

In the case where the trap state energy level sits exactly in the middle of E_fe and E_fh, it can be shown [42] that $R - G = R_m \frac{\exp(eV/kT) - 1}{\exp(eV/2kT) - 1} = R_m \left[\exp\left(\frac{eV}{2kT}\right) - 1\right]$. The maximum recombination rate is reached at this point and is significantly larger than in other parts of the junction. As a consequence, an additional current component arises: $j_{\text{SRH}} = e \int R_m \left[\exp\left(\frac{eV}{2kT}\right) - 1\right] dx$. High carrier injection at larger biases causing significant increases in the majority carrier in the quasi-neutral regions also leads to a similar voltage dependence in the current. The total current is thus $j_T = \sum_n j_{Tn} \left[\exp\left(\frac{eV}{nkT}\right) - 1\right]$ and may exhibit a different dependence on V in different ranges.

2.3.3 Response of a pn Junction with Photogeneration

Solar cells and photodiode-type photodetectors rely on conversion of absorbed incident photons to electrical responses. In particular, a p-n junction is able to maintain a current flowing in the reverse direction (J_{SC}) when no external biases is applied or maintain a forward bias (V_{OC}) when no current flows in the circuit. The short-circuit current J_{SC} is formed when electrons and holes excited by photon absorption events are separated efficiently to their corresponding electrodes. Consider the same p-n junction as in **Figure 2-5** with light incident from the left and with no bias applied. Consider the simplest model, where light excitation only occurs in the quasi-neutral region of the p-side with a constant generation rate G_l, the continuity equation for minority hole is written as:

$$-D_h\frac{\partial^2 p}{\partial x^2} = G_l - \frac{p-p_0}{\tau_h} \tag{2.11}$$

where we assume that the excitation is not strong enough to affect the hole lifetime τ_h. It can also be reasonably assumed that the excess hole concentration $p-p_0$ vanishes at both the left end and the left boundary of the depletion region under zero bias in **Figure 2-5**. The solution is then:

$$p - p_0 = G_l\tau_h - G_l\tau_h\frac{\sinh\left(\frac{W_n+x}{L_h}\right) - \sinh\left(\frac{x+x_n}{L_h}\right)}{\sinh\left(\frac{W_n-x_n}{L_h}\right)} \tag{2.12a}$$

$$J_h(x) = G_lL_h\frac{\cosh\left(\frac{W_n+x}{L_h}\right) - \cosh\left(\frac{x+x_n}{L_h}\right)}{\sinh\left(\frac{W_n-x_n}{L_h}\right)} \tag{2.12b}$$

The hole diffusion current is hence anti-symmetric with respect to $x = (W_p + x_p)/2$, with half of the net-generated carrier flowing to the left electrodes. Since the electron current at $-x_n$ should be close to zero, the total electrical current is just $j_T = eJ_h(-x_n)$, i.e., the total current is determined by the minority hole current at this location. Furthermore,

$$j_L = j_T = eJ_h(-x_n) = eG_lL_h, \qquad \text{when } L_h \ll W_p \tag{2.13a}$$

$$j_L = j_T = eJ_h(-x_n) = eG_l\frac{W_p - x_p}{2}, \qquad \text{when } L_h \gg W_p \tag{2.13b}$$

This indicates that the charge extracted is at most one half of the total generated charge and is far less than ideal when the diffusion length becomes shorter than the quasi-neutral region width. The case is similar for electrons generated on the p-side of the junction if the light excitation extends across the whole structure. For generation occurring within the depletion region, because of the strong electric field, the generated carriers can be separated and driven in their favorable directions, and the extraction efficiency is considered to be close to unity.

This analysis demonstrates the importance of the location and the width of the depletion region in achieving high J_{SC}. In fact, most practical solar cell and photodiode designs implement a thin highly-doped top layer to make sure that light absorption takes place primarily within the thicker depletion region located in the lower-doped region. This can also be achieved by using a p-i-n structure where an intrinsic layer is placed between the p- and n-type layers, resulting in a spatial-charge region of at least the thickness of the intrinsic layer, in which most of the light absorption is meant to occur. The carrier diffusion length also plays an important role in ensuring the extraction of carriers in the quasi-neutral regions and when the width and the strength of the electric field in the depletion layer are reduced under forward bias.

The total current under simultaneous photogeneration and biases can be treated as the sum of the individual current component, as a reasonable approximation. This is because the minority carrier continuity equation in the quasi-neutral region is still described by 2.11, with appropriate boundary conditions accounting for the effects of the applied bias. Due to the linearity of the equation and assuming constant coefficients under weak injection, the solution is therefore the sum of 2.9 and 2.13 and consequently, the total current with everything included is :

$$j = j_L - \sum_n j_{n0}\left[\exp\left(\frac{eV}{nkT}\right) - 1\right] \tag{2.14}$$

A generic solar cell current-voltage (J-V) curve is shown in **Figure 2-6**. Some solar cell figures of merits are labeled in the figure and defined as follows: j_{SC}, the current density at which the voltage is zero; V_{OC}, the voltage sustained at zero-current; j_{mpp} and V_{mpp}, the current density and voltage, respectively, at which the power supplied to the external circuit (the area of the rectangle in the first quadrant) is maximized; and the fill factor $FF = \dfrac{j_{\mathrm{mpp}}V_{\mathrm{mpp}}}{j_{\mathrm{SC}}V_{\mathrm{OC}}}$. The PCE is then naturally defined as $j_{\mathrm{mpp}}V_{\mathrm{mpp}}/I_{\mathrm{in}}$ where I_{in} is the solar irradiance incident on the solar cell. The standard value of 1000.4 W/cm^2, corresponding to the total power density in the AM1.5 global horizontal irradiance spectrum, is often used as the incident irradiance.

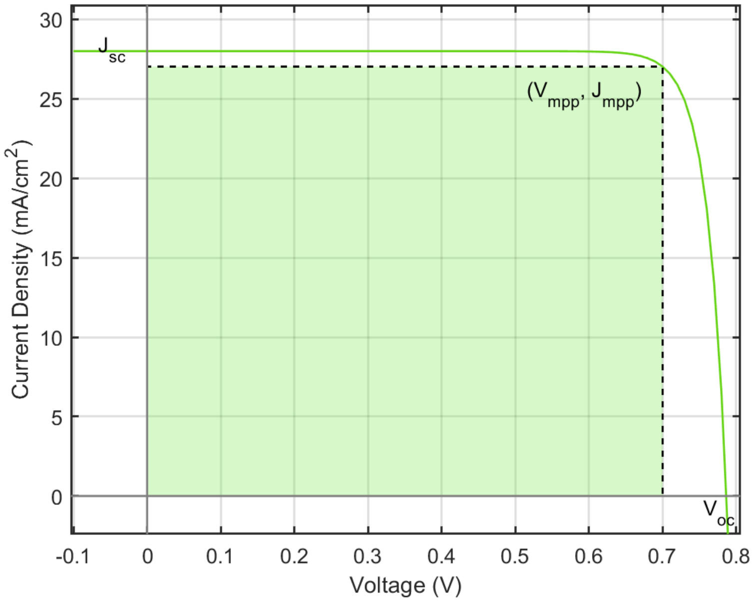

Figure 2-6. An example current density-voltage curve for a generic solar cell under solar illumination with figures of merit labeled.

When used as photodetectors, the design considerations for photodiodes change. Instead of the goal of achieving the highest possible output power, photodiode-type photodetectors are designed to maintain consistent, stable, and fast detection of received light signals. In most cases, photodetectors are operated in reverse-bias mode, in order to establish a wide depletion width for both efficient and fast charge collection. When an electron-hole pair is generated inside the depletion region after absorption of a photon, the charge carriers start to move to their electrodes at speeds determined by their mobilities and the local electric field, resulting in an instantaneous current flow in the external circuit caused by capacitive coupling, described by the Shockley-Ramo theorem [44, 45]. The current lasts until the charge carriers reach their corresponding electrodes. The collective current due to all electrons and holes generated everywhere in the device by an infinitely short light pulse can then be approximated by an exponential of the form: $< I >= I_h e^{-t/\tau_h} + I_e e^{-t/\tau_e}$, where τ_e and τ_h denote the transit times of carriers: $\tau = {}^{W}/_{\mu E}$, where W is the width of the depletion layer. This is also the impact response function h(t) of the photodiode. If carriers undergo considerable recombination events before being swept to the electrodes, the carrier lifetimes also contribute to the exponential decay, but since they are usually much longer than the transit times in practical devices, the overall time constant in the measured current is determined almost completely by the transit times. This principle also allows macroscopic electrical measurements to be used to probe properties such as carrier mobilities, etc. On the other hand, the temporal response of a photodiode is also affected by its depletion capacitance C_{dep} when operating under reverse bias. The transfer function is then:

$$f(s) = h(s)\frac{1}{1 + sC_{\text{dep}}R_{\text{ext}}} \propto \left(\frac{1}{1 + s\tau_e} + \frac{1}{1 + s\tau_h}\right)\left(\frac{1}{1 + sC_{\text{dep}}R_{\text{ext}}}\right) \tag{2.15}$$

where R_{ext} is the resistance contributed by the external circuit. This relation determines how fast the photodiode reacts to external light, or the detection bandwidth. It also contains the tradeoff between the bandwidth and the efficiency. A wider depletion region absorbs more light and hence a stronger signal is generated, while ultra-fast photodiodes usually require narrower device width for shorter transit times. This is also the essential reason that the structures of photovoltaic solar cells differ from those of photodiode-type photodetectors.

Quantum efficiencies are another set of metrics to quantify the operation of both solar cells and photodetectors [46, 47]. While internal quantum efficiency (IQE) quantifies the ratio by which absorbed photons are converted to carriers that flow in the circuit, external quantum efficiency (EQE) measures the ratio by which photons incident on the active surface are converted to carriers. These two quantities are related such that $EQE(\lambda) = IQE(\lambda)a(\lambda)$ where a denotes the absorptivity and all quantities are wavelength-dependent. For solar cells that employ MEG or photodetectors with gain mechanisms such as avalanche photodetectors and photoconductors, EQE and IQE can, in theory, exceed unity. For photodetectors, the responsivity R is another important factor that quantifies how efficiently incident photon power is converted to electrical current and is related to EQE by $R(\lambda) = EQE(\lambda)\,{}^{q\lambda}/_{hc}$.

For all photodetection mechanisms, there is a fundamental physical limit for the weakest detectable signal which is usually determined by the lowest noise-level of the system.The associated quantity is detectivity $D = \frac{\sqrt{A\Delta f}}{NEP}$ [48], where A is the detector area, Δf is the bandwidth of the system and NEP denotes the noise-equivalent power. The unit of detectivity is Jones: $\mathrm{cm}^{1/2}\mathrm{Hz}^{-1/2}\mathrm{W}^{-1}$. Generally, the NEP of the system is closely related to the bandwidth. For ideal photodiodes, the noise originates from the generation of carriers, which in the case of a continuous coherent incident wave, takes the form of shot noise with a spectral density proportional to the photocurrent by $S_I(\omega) = eI_{ph}$, and hence$NEP = \frac{1}{R}\sqrt{2S_I(\omega)\Delta f}$ and $D = \frac{R\sqrt{A}}{\sqrt{2eI_{\mathrm{ph}}}}$, where R is the responsivity. Another major contribution to the noise is Johnson-Nyquist noise[49] from the thermal fluctuation of charge carriers inside resistive components in the circuit, with $S_I(\omega) = {}^{4k_BT}/_{R}$ at room temperature and higher. The power spectral density of Johnson-Nyquist is also constant, and affects the detectivity similarly, resulting in $D = \frac{R\sqrt{A}}{\sqrt{2eI_{\mathrm{ph}} + \frac{8k_BT}{R}}}$.

2.3.4 Architectures of PbS CQD Solar Cells and Photodetectors

The earliest solar cells that incorporate CQD actually relied on them only as the solar absorbers, instead of as the material responsible for both carrier generation and transport. These were known as CQD-sensitized solar cells [50, 51]. Similar to dye-sensitized solar cells (DSSCs), the sensitizing CQDs are coated on a nanoporous electron acceptor, usually TiO_2. The electron acceptor/absorber matrix is immersed in a electrolytic medium, usually containing redox pairs such as I_3^-/I^-, which serve to transport holes, and is connected to the counter-electrode. Because of this structure, CQD-sensitized solar cells have two major drawbacks: a low short circuit current due to the very limited thickness of the CQD absorbing material, and a low fill factor caused by the unavoidable direct contact between the electron transport oxide and the hole transport electrolyte.

The discovery that photo-generated excitons within certain types of CQDs readily dissociate, causing the electron and hole to move in separate directions in the presence of an electric field [52, 53], enabled solar cell devices that employed p-type CQD thin films as semiconductor analogs, without the infiltration of materials such as conjugated polymers, to be built. The first thin-film CQD solar cells were Schottky-junction solar cells [54–56]. This architecture consists of a shallow work function metal, such as Mg or Al, in contact with a mildly p-doped CQD film to form a Schottky barrier that produces a diode rectification effect as well as a wide spatial field region to facilitate charge extractions, as shown in **Figure 2-7a**. The anode is a transparent conductive oxide (TCO, usually indium tin oxide - ITO). The simple Schottky solar cell structure necessitates only these 3 layers and is able to deliver up to 5.2% PCE [56]. Unfortunately, the performance of Schottky junction solar cells are inherently limited because i) the built-in potential only resides in the non-metal side of the junction and the open circuit voltage therefore cannot exceed half of the band gap energy of the CQD film; ii) the metal-CQD interface, which typically contains a high density of trap states, tends to pin the Fermi level at an undesired position

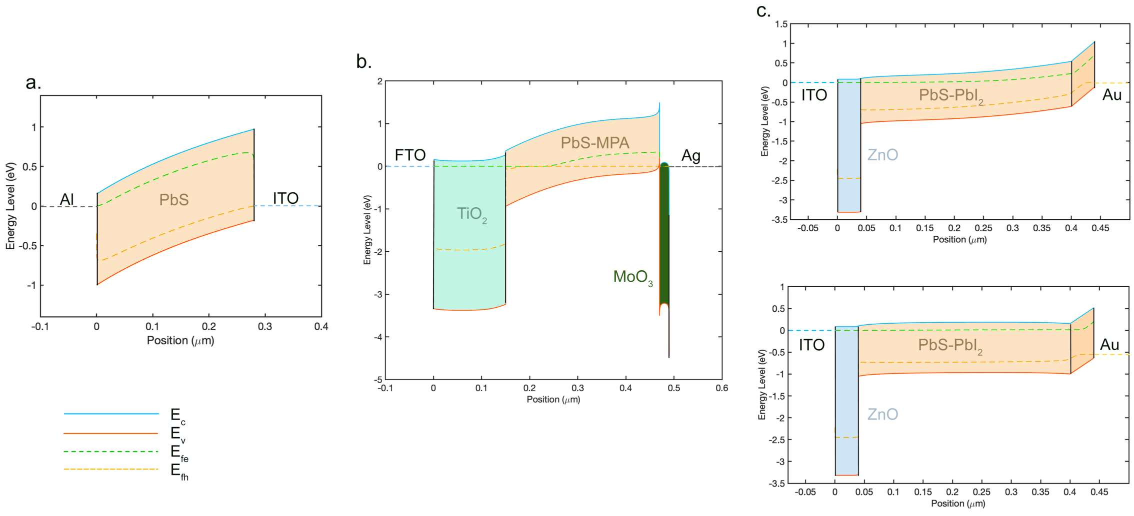

Figure 2-7. Energy band diagrams for common CQD solar cell architectures. The legend in the bottom left corner denotes the colors corresponding to specific energy bands in all plots (E_c: conduction band edge; E_v: valence band edge; E_fe: electron quasi-Fermi level; E_fh, hole quasi-Fermi level). **a.** Band diagram for a Schottky junction solar cell employing an aluminum cathode and ITO anode. **b.** Band diagram for a depleted heterojunction solar cell employing FTO (Fluorine-doped tin oxide), TiO_2, MPA-passivated PbS CQDs, MoO_3 and silver. **c.** Improved depleted heterojunction solar cell band structures using ZnO, iodide-passivated PbS CQDs, EDT-passivated CQDs and gold. Top: band diagram for short circuit conditions. Bottom: band diagram for the maximum power point.

and inhibit the voltage further.

Further improvements in CQD solar cells were made possible through careful choice of carrier transport layers, between which the CQD layers are sandwiched. This general structure is known as the depleted heterojunction architecture. TiO_2 that was used extensively in sensitized solar cells was also found to be a great candidate for an electron transport material in the depleted heterojunction architecture, due to its native n-doping, visible transparency and deep valence band edge that allows it to act as a hole barrier for the adjacent CQD layer. Further tuning of the doping density of TiO_2 as well as the conduction band edge of the CQD materials was carried out so that the CQD layer was made almost fully depleted through contact with the TiO_2 alone, allowing the formation of a wide spatial field under short circuit conditions. Moreover, an additional thin buffer layer – playing the role of a hole transport layer (HTL) - made of MoO_3 or LiF and deposited between the CQD film and the anode was found to considerably improve the solar cell performance and stability by providing a back-surface field as well as preventing the degradation of CQDs in contact with the anode metal [57, 58]. The majority of CQD assemblies used in the first generation of depleted heterojunction solar cells were surface-passivated with EDT or MPA, which are bi-linker molecules that reduce inter-dot spacing. However, the solid-state ligand exchange processes required to bind them to the CQDs introduced surface traps. A band diagram for a depleted heterojunction device of this type is shown in shown in **Figure 2-7b**. Terminologically, the architecture that places the ETL next to the TCO, thus making it the cathode, is regarded as the ”inverted” architecture, as opposed to the conventional structure adopted in organic photovoltaics that uses the TCO as the anode. For CQD solar cells, the inverted structure is the dominant type due to its improved stability at the interfaces, a wider compatibility among fabrication techniques, and, more importantly, it is the architecture in which almost all significant efficiency records have been demonstrated. [59–61].

The depleted heterojunction architecture proved to be a great platform for exploring the impacts of engineering a variety of factors including surface passivation and crosslinking of the CQDs, interface modification of the junctions, carrier extraction layers, etc. Most high-efficiency CQD solar cells with PCEs >10% are based on the depleted heterojunction with ZnO as the electron transport layer and an atomic halide passivated CQD active layer [30, 36, 37]. The combination of the high doping density of ZnO and the deeper energy band levels in halide-passivated CQD films, as well as a dramatically improved diffusion length in the CQD layers thanks to improved mobility and reductions in trap states, enables this architecture to support a spatial field for efficient carrier extraction up to the maximum power point for CQD layers thicker than about 400 nm. Usually, another thin layer of EDT-passivated CQDs is then deposited as the transition layer, or hole transport layer, to a deep work function metal (Au usually) electrode. Device band diagrams at short circuit conditions and at the maximum power point are shown in **Figure** 2-7**c**. This architecture yields devices with PCEs consistently above 10%, independent of specific fabrication conditions or ligand treatments across various reports, and also demonstrates good long-term air stability. Looking at the latest generation of depleted heterojunction devices, it is surprising that the state-of-the-art CQD solar cell architecture is not significantly more complicated, in terms of the species of materials or the number of layers required, than most of the early implementations with only a fraction of the PCE. Future work in this area will focus on further simplification of the fabrication processes, adaptation to large-quantity scalable production, and continuing increases in efficiency

In contrast, several different photodetector architectures based on PbS QDs have shown promise. **Figure** 2-8 depicts the three main QD photodetector architectures: photoconductors, phototransistors and photodiodes. Photoconductors are composed of a uniformly doped PbS QD layer sandwiched between two identical metal electrodes whose work function allows carrier transport across the interface without a voltage drop. The carrier concentration and conductivity of the PbS QD film is drastically increased with light absorption, and each absorbed photon can cause multiple majority carriers to circulate through the external circuit if the transit time through the device is much shorter than the carrier lifetime, thus creating gain.

Phototransistors, as shown in the figure, are similarly structured planar devices that also include a bottom oxide gate placed on top of a conducting material. They bear resemblance to metal-oxide-semiconductor field-effect transistors (MOSFETs) in that the photoconductivity is simultaneously modulated by the applied gate voltage, VG, which shapes the conducting channel between the source and drain electrodes by creating carrier accumulation or depletion. This structure also allows for more complicated configurations to enable higher gains or bandwidths, such as by incorporating 2D materials as

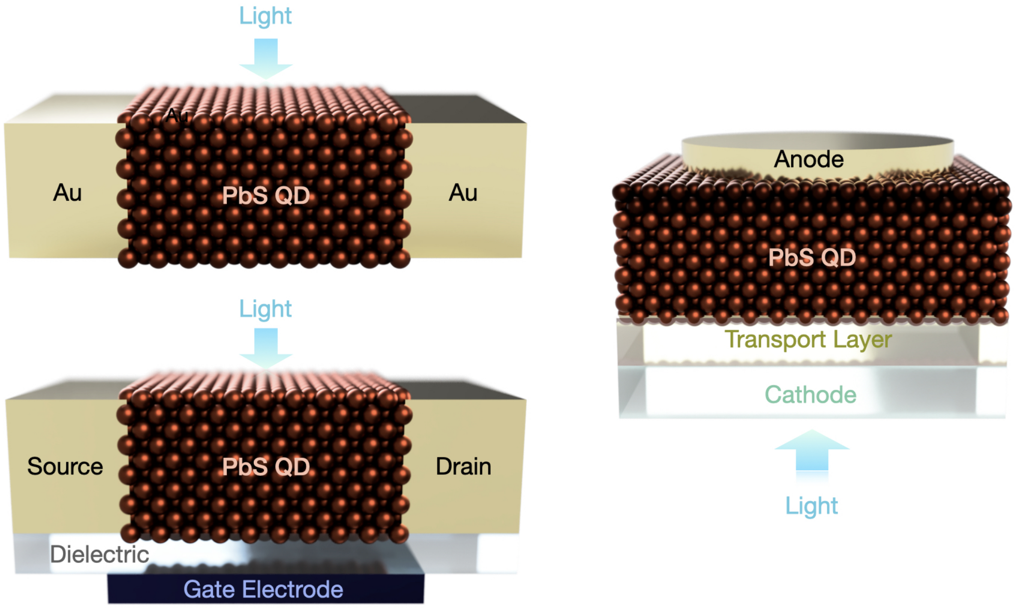

Figure 2-8. Basic Architectures of PbS QD based photoconductor (upper left), phototransistor (lower left) and photodiodes (right).

the actual conducting channel with carrier injection from PbS QDs [62, 63].

Photodiode-type detectors are similar to solar cells, in that they are constructed from a vertical stack of layers. In general, any photovoltaic solar cell can also operate as a photodetector. The difference is that rather than being designed to output the maximum possible power at a forward bias, photodiode-type photodetectors are designed to generate photocurrents that depend as linearly as possible on the incident illumination flux at reverse bias, as well as for fast responses and low dark current. This necessitates a careful balance of the active layer thickness, depletion capacitance, recombination strengths, etc.

References

[1] S. Adachi, "Lead Sulphide (PbS)," in *Optical Constants of Crystalline and Amorphous Semiconductors: Numerical Data and Graphical Information*, edited by S. Adachi (Springer US, Boston, MA, 1999), pp. 613–621.

[2] J. N. Zemel, J. D. Jensen, and R. B. Schoolar, "Electrical and Optical Properties of Epitaxial Films of PbS, PbSe, PbTe, and SnTe," Physical Review **140**, A330–A342 (1965).

[3] G. Martinez, M. Schlüter, and M. L. Cohen, "Electronic structure of PbSe and PbTe. I. Band structures, densities of states, and effective masses," Physical Review B **11**, 651–659 (1975).

[4] K. Hummer, A. Grüneis, and G. Kresse, "Structural and electronic properties of lead chalcogenides from first principles," Physical Review B **75**, 195211 (2007).

[5] J. M. Luttinger and W. Kohn, "Motion of Electrons and Holes in Perturbed Periodic Fields," Physical Review **97**, 869–883 (1955).

[6] L. Brus, "Electronic wave functions in semiconductor clusters: experiment and theory," The Journal of Physical Chemistry **90**, 2555–2560 (1986).

[7] Y. Wang, A. Suna, W. Mahler, and R. Kasowski, "PbS in polymers. From molecules to bulk solids," The Journal of Chemical Physics **87**, 7315–7322 (1987).

[8] R. S. Kane, R. E. Cohen, and R. Silbey, "Theoretical Study of the Electronic Structure of PbS Nanoclusters," The Journal of Physical Chemistry **100**, 7928–7932 (1996).

[9] D. L. Mitchell and R. F. Wallis, “Theoretical Energy-Band Parameters for the Lead Salts,” Physical Review **151**, 581–595 (1966).

[10] I. Kang and F. W. Wise, “Electronic structure and optical properties of PbS and PbSe quantum dots,” Journal of the Optical Society of America B **14**, 1632 (1997).

[11] T. Takagahara, “Electron-phonon interactions and excitonic dephasing in semiconductor nanocrystals,” Physical Review Letters **71**, 3577–3580 (1993).

[12] T. D. Krauss and F. W. Wise, “Coherent Acoustic Phonons in a Semiconductor Quantum Dot,” Physical Review Letters **79**, 5102–5105 (1997).

[13] S. Schmitt-Rink, D. A. B. Miller, and D. S. Chemla, “Theory of the linear and nonlinear optical properties of semiconductor microcrystallites,” Physical Review B **35**, 8113–8125 (1987).

[14] B. Cho, W. K. Peters, R. J. Hill, T. L. Courtney, and D. M. Jonas, “Bulklike Hot Carrier Dynamics in Lead Sulfide Quantum Dots,” Nano Letters **10**, 2498–2505 (2010).

[15] I. Moreels, K. Lambert, D. Smeets, D. De Muynck, T. Nollet, J. C. Martins, F. Vanhaecke, A. Vantomme, C. Delerue, G. Allan, and Z. Hens, “Size-Dependent Optical Properties of Colloidal PbS Quantum Dots,” ACS Nano **3**, 3023–3030 (2009).

[16] Peter Würfel, “Limitations on Energy Conversion in Solar Cells,” in *Physics of Solar Cells* (John Wiley & Sons, Ltd, 2007), pp. 137–153.

[17] n. Benisty, n. Sotomayor-Torrès, and n. Weisbuch, “Intrinsic mechanism for the poor luminescence properties of quantum-box systems,” Physical Review. B, Condensed Matter **44**, 10945–10948 (1991).

[18] V. I. Klimov and D. W. McBranch, “Femtosecond 1P-to-1S Electron Relaxation in Strongly Confined Semiconductor Nanocrystals,” Physical Review Letters **80**, 4028–4031 (1998).

[19] U. Woggon, H. Giessen, F. Gindele, O. Wind, B. Fluegel, and N. Peyghambarian, “Ultrafast energy relaxation in quantum dots,” Physical Review B **54**, 17681–17690 (1996).

[20]R. J. Ellingson, M. C. Beard, J. C. Johnson, P. Yu, O. I. Micic, A. J. Nozik, A. Shabaev, and A. L. Efros, “Highly Efficient Multiple Exciton Generation in Colloidal PbSe and PbS Quantum Dots,” Nano Letters **5**, 865–871 (2005).

[21]R. D. Schaller and V. I. Klimov, “High Efficiency Carrier Multiplication in PbSe Nanocrystals: Implications for Solar Energy Conversion,” Physical Review Letters **92**, 186601 (2004).

[22]V. Sukhovatkin, S. Hinds, L. Brzozowski, and E. H. Sargent, “Colloidal Quantum-Dot Photodetectors Exploiting Multiexciton Generation,” Science **324**, 1542–1544 (2009).

[23]C. Kittel, “Nanostrucutres,” in *Introduction to Solid State Physics*, 8th ed. (2004), pp. 517–518.

[24]C. B. Murray, C. R. Kagan, and M. G. Bawendi, “Synthesis and Characterization of Monodisperse Nanocrystals and Close-Packed Nanocrystal Assemblies,” Annual Review of Materials Science **30**, 545–610 (2000).

[25]H. Grätz, “Ostwald ripening: New relations between particle growth and particle size distribution,” Scripta Materialia **37**, 9–16 (1997).

[26]M. A. Hines and G. D. Scholes, “Colloidal PbS Nanocrystals with Size-Tunable Near-Infrared Emission: Observation of Post-Synthesis Self-Narrowing of the Particle Size Distribution,” Advanced Materials **15**, 1844–1849 (2003).

[27]L. Cademartiri, J. Bertolotti, R. Sapienza, D. S. Wiersma, G. von Freymann, and G. A. Ozin, “Multigram Scale, Solventless, and Diffusion-Controlled Route to Highly Monodisperse PbS Nanocrystals,” The Journal of Physical Chemistry B **110**, 671–673 (2006).

[28]I. Moreels, Y. Justo, B. De Geyter, K. Haustraete, J. C. Martins, and Z. Hens, “Size-Tunable, Bright, and Stable PbS Quantum Dots: A Surface Chemistry Study,” ACS Nano **5**, 2004–2012 (2011).

[29]J. Zhang, R. W. Crisp, J. Gao, D. M. Kroupa, M. C. Beard, and J. M. Luther, “Synthetic Conditions for High-Accuracy Size Control of PbS Quantum Dots,” The Journal of Physical Chemistry Letters **6**, 1830–1833 (2015).

[30]P. R. Brown, D. Kim, R. R. Lunt, N. Zhao, M. G. Bawendi, J. C. Grossman, and V. Bulović, "Energy Level Modification in Lead Sulfide Quantum Dot Thin Films through Ligand Exchange," ACS Nano **8**, 5863–5872 (2014).

[31]E. J. D. Klem, D. D. MacNeil, P. W. Cyr, L. Levina, and E. H. Sargent, "Efficient solution-processed infrared photovoltaic cells: Planarized all-inorganic bulk heterojunction devices via inter-quantum-dot bridging during growth from solution," Applied Physics Letters **90**, 183113 (2007).

[32]A. G. Pattantyus-Abraham, I. J. Kramer, A. R. Barkhouse, X. Wang, G. Konstantatos, R. Debnath, L. Levina, I. Raabe, M. K. Nazeeruddin, M. Grätzel, and E. H. Sargent, "Depleted-Heterojunction Colloidal Quantum Dot Solar Cells," ACS Nano **4**, 3374–3380 (2010).

[33]L. Sun, J. J. Choi, D. Stachnik, A. C. Bartnik, B.-R. Hyun, G. G. Malliaras, T. Hanrath, and F. W. Wise, "Bright infrared quantum-dot light-emitting diodes through inter-dot spacing control," Nature Nanotechnology **7**, 369–373 (2012).

[34]J. Tang, K. W. Kemp, S. Hoogland, K. S. Jeong, H. Liu, L. Levina, M. Furukawa, X. Wang, R. Debnath, D. Cha, K. W. Chou, A. Fischer, A. Amassian, J. B. Asbury, and E. H. Sargent, "Colloidal-quantum-dot photovoltaics using atomic-ligand passivation," Nature Materials **10**, 765–771 (2011).

[35]A. H. Ip, S. M. Thon, S. Hoogland, O. Voznyy, D. Zhitomirsky, R. Debnath, L. Levina, L. R. Rollny, G. H. Carey, A. Fischer, K. W. Kemp, I. J. Kramer, Z. Ning, A. J. Labelle, K. W. Chou, A. Amassian, and E. H. Sargent, "Hybrid passivated colloidal quantum dot solids," Nature Nanotechnology **7**, 577–582 (2012).

[36]R. W. Crisp, D. M. Kroupa, A. R. Marshall, E. M. Miller, J. Zhang, M. C. Beard, and J. M. Luther, "Metal Halide Solid-State Surface Treatment for High Efficiency PbS and PbSe QD Solar Cells," Scientific Reports **5**, 9945 (2015).

[37] M. Liu, O. Voznyy, R. Sabatini, F. P. García de Arquer, R. Munir, A. H. Balawi, X. Lan, F. Fan, G. Walters, A. R. Kirmani, S. Hoogland, F. Laquai, A. Amassian, and E. H. Sargent, "Hybrid organic–inorganic inks flatten the energy landscape in colloidal quantum dot solids," Nature Materials **16**, 258–263 (2017).

[38] W. van Roosbroeck and W. Shockley, "Photon-Radiative Recombination of Electrons and Holes in Germanium," Physical Review **94**, 1558–1560 (1954).

[39] W. Shockley and H. J. Queisser, "Detailed Balance Limit of Efficiency of *p-n* Junction Solar Cells," Journal of Applied Physics **32**, 510–519 (1961).

[40] A. D. Vos, "Detailed balance limit of the efficiency of tandem solar cells," Journal of Physics D: Applied Physics **13**, 839–846 (1980).

[41] Peter Würfel, "Conversion of Thermal Radiation into Chemical Energy," in *Physics of Solar Cells* (John Wiley & Sons, Ltd, 2007), pp. 85–92.

[42] Peter Würfel, "Basic Structure of Solar Cells," in *Physics of Solar Cells* (John Wiley & Sons, Ltd, 2007), pp. 109–136.

[43] D. Neamen, *Semiconductor Physics And Devices* (McGraw-Hill Education, 2003), 774 pp.

[44] W. Shockley, "Currents to Conductors Induced by a Moving Point Charge," Journal of Applied Physics **9**, 635–636 (1938).

[45] S. Ramo, "Currents Induced by Electron Motion," Proceedings of the IRE **27**, 584–585 (1939).

[46] C. R. Kagan, E. Lifshitz, E. H. Sargent, and D. V. Talapin, "Building devices from colloidal quantum dots," Science **353**, `10.1126/science.aac5523` (2016).

[47] R. Saran and R. J. Curry, "Lead sulphide nanocrystal photodetector technologies," Nature Photonics **10**, 81–92 (2016).

[48] R. C. Jones, "A Method of Describing the Detectivity of Photoconductive Cells," Review of Scientific Instruments **24**, 1035–1040 (1953).

[49] J. B. Johnson, "Thermal Agitation of Electricity in Conductors," Physical Review **32**, 97–109 (1928).

[50] K. S. Leschkies, R. Divakar, J. Basu, E. Enache-Pommer, J. E. Boercker, C. B. Carter, U. R. Kortshagen, D. J. Norris, and E. S. Aydil, "Photosensitization of ZnO Nanowires with CdSe Quantum Dots for Photovoltaic Devices," Nano Letters **7**, 1793–1798 (2007).

[51] S. H. Im, H.-j. Kim, S. W. Kim, S.-W. Kim, and S. I. Seok, "All solid state multiply layered PbS colloidal quantum-dot-sensitized photovoltaic cells," Energy & Environmental Science **4**, 4181–4186 (2011).

[52] S. A. McDonald, G. Konstantatos, S. Zhang, P. W. Cyr, E. J. D. Klem, L. Levina, and E. H. Sargent, "Solution-processed PbS quantum dot infrared photodetectors and photovoltaics," Nature Materials **4**, 138–142 (2005).

[53] A. Maria, P. W. Cyr, E. J. D. Klem, L. Levina, and E. H. Sargent, "Solution-processed infrared photovoltaic devices with $>$10% monochromatic internal quantum efficiency," Applied Physics Letters **87**, 213112 (2005).

[54] G. I. Koleilat, L. Levina, H. Shukla, S. H. Myrskog, S. Hinds, A. G. Pattantyus-Abraham, and E. H. Sargent, "Efficient, Stable Infrared Photovoltaics Based on Solution-Cast Colloidal Quantum Dots," ACS Nano **2**, 833–840 (2008).

[55] W. Ma, S. L. Swisher, T. Ewers, J. Engel, V. E. Ferry, H. A. Atwater, and A. P. Alivisatos, "Photovoltaic Performance of Ultrasmall PbSe Quantum Dots," ACS Nano **5**, 8140–8147 (2011).

[56] C. Piliego, L. Protesescu, S. Z. Bisri, M. V. Kovalenko, and M. A. Loi, "5.2% efficient PbS nanocrystal Schottky solar cells," Energy & Environmental Science **6**, 3054–3059 (2013).

[57] J. Gao, C. L. Perkins, J. M. Luther, M. C. Hanna, H.-Y. Chen, O. E. Semonin, A. J. Nozik, R. J. Ellingson, and M. C. Beard, "N-Type Transition Metal Oxide as a Hole Extraction Layer in PbS Quantum Dot Solar Cells," Nano Letters **11**, 3263–3266 (2011).

[58] P. R. Brown, R. R. Lunt, N. Zhao, T. P. Osedach, D. D. Wanger, L.-Y. Chang, M. G. Bawendi, and V. Bulović, "Improved Current Extraction from ZnO/PbS Quantum Dot Heterojunction Photovoltaics Using a MoO3 Interfacial Layer," Nano Letters **11**, 2955–2961 (2011).

[59] J. M. Luther, J. Gao, M. T. Lloyd, O. E. Semonin, M. C. Beard, and A. J. Nozik, "Stability Assessment on a 3% Bilayer PbS/ZnO Quantum Dot Heterojunction Solar Cell," Advanced Materials **22**, 3704–3707 (2010).

[60] Y. Sun, J. H. Seo, C. J. Takacs, J. Seifter, and A. J. Heeger, "Inverted Polymer Solar Cells Integrated with a Low-Temperature-Annealed Sol-Gel-Derived ZnO Film as an Electron Transport Layer," Advanced Materials **23**, 1679–1683 (2011).

[61] B.-R. Hyun, J. J. Choi, K. L. Seyler, T. Hanrath, and F. W. Wise, "Heterojunction PbS Nanocrystal Solar Cells with Oxide Charge-Transport Layers," ACS Nano **7**, 10938–10947 (2013).

[62] G. Konstantatos, M. Badioli, L. Gaudreau, J. Osmond, M. Bernechea, F. P. G. de Arquer, F. Gatti, and F. H. L. Koppens, "Hybrid graphene–quantum dot phototransistors with ultrahigh gain," Nature Nanotechnology **7**, 363–368 (2012).

[63] D. Kufer, I. Nikitskiy, T. Lasanta, G. Navickaite, F. H. L. Koppens, and G. Konstantatos, "Hybrid 2D–0D MoS2–PbS Quantum Dot Photodetectors," Advanced Materials **27**, 176–180 (2015).

Chapter 3

Extending the Capabilities of PbS QD Devices via Photonic Engineering

3.1 Multi-Color and Semi-Transparent PbS QD Solar Cells from optimized thin film interference

This section is partially adapted from Ref[1]. Reprinted with permission from Optics Express 24, no. 4, A101-A112, "Color-tuned and transparent colloidal quantum dot solar cells via optimized multilayer interference", by Arinze, Ebuka S., Botong Qiu, Nathan Palmquist, Yan Cheng, Yida Lin, Gabrielle Nyirjesy, Gary Qian, and Susanna M. Thon, copyright © 2017.

3.1.1 Introduction

Solar cells generate electrical power that scales with the areas of the panels. As the most visible and exposed components of the system that occupy large areas, it is appealing if the panels match or add to the appearance of surroundings, at the same time supplying electrical power efficiently and stably. Multi-colored solar cells can be achieved with controlled, tunable spectral reflection and absorption profiles, and thus are of significant interest due to their potential to be placed or coated on exterior surfaces of urban infrastructures, such as building facades, rooftops and other residential or industrial facilities, to serve both aesthetic and functional purposes [2, 3]. In tandem cell applications, there is also a need to systematically control absorption and, in turn, achieve the required current-matching in cells that possess different spectral absorption profiles. Additionally, semitransparent solar cells are attractive for integration into portable electronics and for window coatings to help with building and vehicular heat management [4, 5]. Solar cells based on solution- processed materials are especially promising for these large-area applications because of their thin-film and lightweight nature, ease and flexibility of fabrication, associated low costs, and high efficiency potential. Past examples of colored solution-processed solar cell technologies include using combinations of dyes[6], photonic filters [7], physically- or chemically-modified absorbing/transport layers [8–11], integrated liquid/photonic crystals[12, 13], embedded optical microcavities and dielectric mirrors [14, 15], and modified top/bottom electrodes [16, 17]in dye-sensitized, organic, and perovskite solar cells.

The light management strategies reported previously, to produce cell colors or achieve transparency often come with an unavoidable loss of photocurrent and device efficiency. On the other hand, Colloidal quantum dots (CQDs), semiconducting nanocrystals stabilized in solution, are a promising candidate material for achieving multicolored and semitransparent solar cells due to their band gap tunability enabled by the quantum size effect discussed in Section 2.1. Specifically, lead sulfide and lead selenide (PbS, bulk band gap energy of 0.41 eV, and PbSe, bulk band gap energy of 0.27 eV) [18, 19]. CQDs have band gaps that can be tuned from the near- infrared to the visible portion of the spectrum. As a result, visible absorption losses induced by the design of multicolored or semitransparent cells can potentially be compensated for by enhanced absorption in the infrared region.

Standard CQD film-based devices[20] **Figure 3-1a** employ different electronic layers that have thicknesses on the order of the optical wavelengths of interest. The layer thicknesses and design are typically optimized for their electrical properties, but optical thin-film interference plays a large role in these devices as well, as demonstrated by efforts to utilize interference effects to achieve semitransparency and absorption enhancement via electrode modification [21] and microcavity structures [22]. Traditionally, transparency in CQD-based devices is induced by employing thin absorbing layers [23, 24]. In this study, we optimize multicolored and transparent CQD solar cells based on thin-film interference engineering concepts to customize both optical and electrical device properties. Using physical modeling and optimization based on Transfer Matrix Method (TMM)[25–27] and multiobjective optimization algorithms[28, 29], we have developed an optimization method for the custom-design of multicolored and transparent CQD solar cells that could be generalized to other materials systems. The optimization sequence is depicted in **Figure 3-1c**. The method maximizes reflection within specific wavelength range or overall transmission, creating a desired cell color, while simultaneously requiring high photogeneration rates in a solar cell device.

3.1.2 Optimization and Tradeoff of Colors and Photocurrents

Our device model makes the following initial assumptions: (1) layers included in the multi- layer device are considered homogeneous and isotropic; (2) interfaces are parallel and optically flat; (3) light is incident normal to the device and is modeled as a plane wave; (4) all photogenerated charge carriers contribute to photocurrent in the device (100% internal quantum efficiency). Some of the restrictions can be lifted as-needed by incorporating into the calculations a more complicated model based on experimental data.

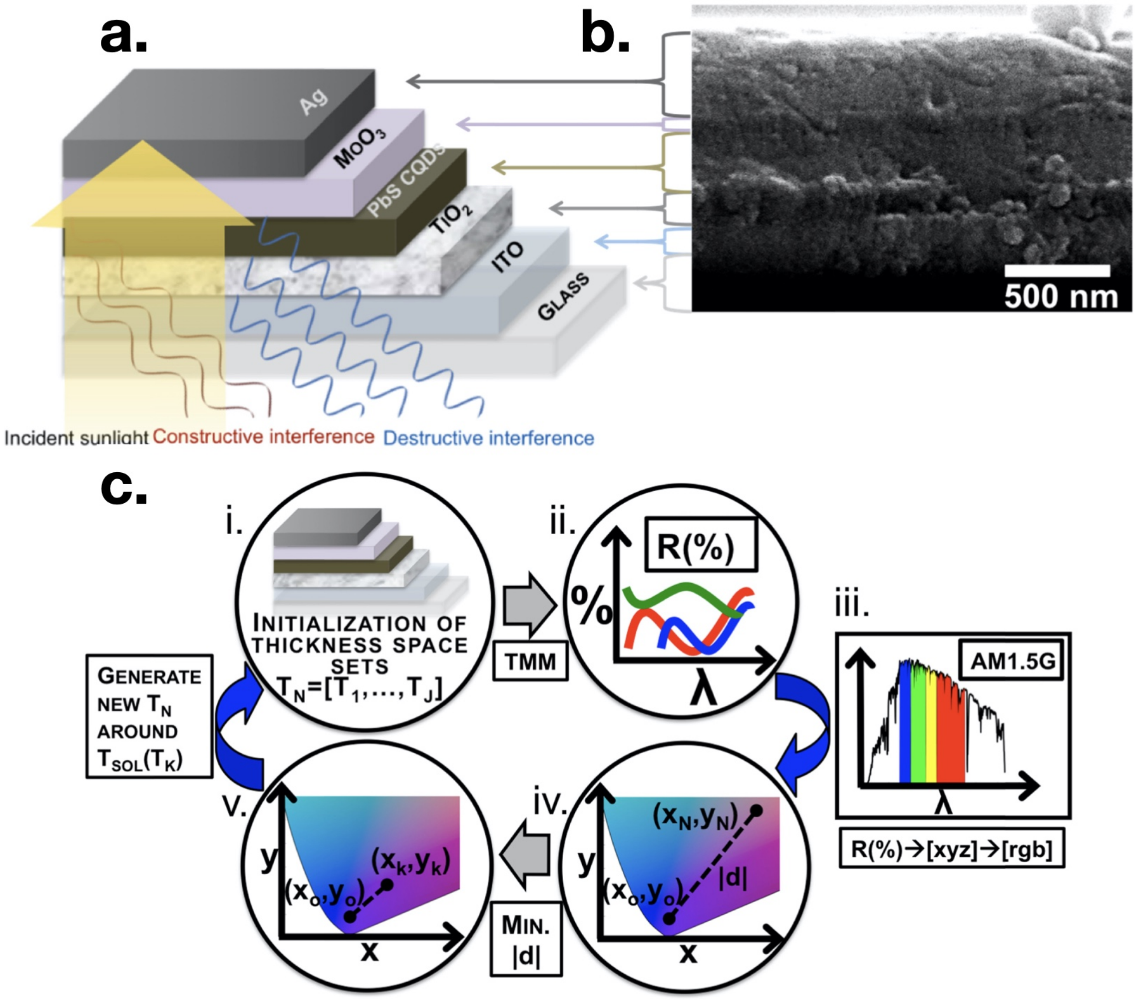

Figure 3-1. a. Schematic of a CQD-based solar cell illustrating the spectrally-dependent optical interference patterns from tuning the thicknesses of the layers, resulting in wavelength-dependent reflectivity and transmission, giving the cell its apparent color or semitransparency. **b.** Cross-sectional scanning electron microscope (SEM) image of the structure shown in (a.). **c.** Graphic representation of the optimization technique to produce cells with defined color characteristics. Space set of thickness combinations is **i** initialized and each combination physically yields **ii** a reflection spectrum via TMM. These spectra in combination with incident **iii** AM1.5G and CIE color matching functions are translated to color coordinates on **iv** Yxy chromaticity plots where the distance to the intended color **iv** is minimized. This optimization cycle repeats until a global optimum is realized.

Firstly,TMM takes the thicknesses and complex refractive indices of all layers as inputs, and calculates electrical field profiles normalized to incident field amplitudes, within the multi-layer structure. In our calculations, the complex refractive index data are from the literature and experimental ellipsometry measurements, and we consider a wavelength range of 300–1800 nm. In the case of opaque reflective colored solar cells, Ag is used as the back contact, while ITO is used as the back contact for the semitransparent cells. We calculate the reflection spectrum of the device, and predict the apparent reflective color using the widely accepted CIE 1931 color matching functions [30] and solar source spectrum (AM1.5 Global Horizontal Irradiance). The predicted color is represented on the Yxy chromaticity plot, Cell "transparency" is calculated by averaging transmittance data over the visible wavelength range (420 nm – 680 nm) output by the TMM calculations.

In order to optimize the thickness profile for a target color, we use particle swarm optimization (PSO) method, a global population -based algorithm [29], as illustrated in **Figure 3-1c**.. A "swarm size" of solution thickness sets is initialized and fed into the TMM to generate associated reflection spectra and the associated apparent color, as the objective function value. These xy co-ordinates are then optimized by minimizing the distance to the target color on the chromaticity plot, yielding a global optimum via multiple iterations. The presence of a population with tendencies of movement towards both the known global best location and individual's best location in PSO allows for both greater degrees of exploration and faster convergence when compared to other optimization methods, such as genetic algorithms. Due to high-dimensionality search space resulted from the multi-layer interference problem, it is highly likely that a semi-periodic landscape of objective values with multiple local minima emerges. Therefore, employing a PSO with a relatively large "swarm size" provides an efficient route to identifying the global optimum for the intended color.

The trade-off between absorption-induced photocurrent generation and transmission through the absorbing material can be partially mitigated by taking the advantage of multi-layer interference effects to reduce the visible-range field overlap with the CQD

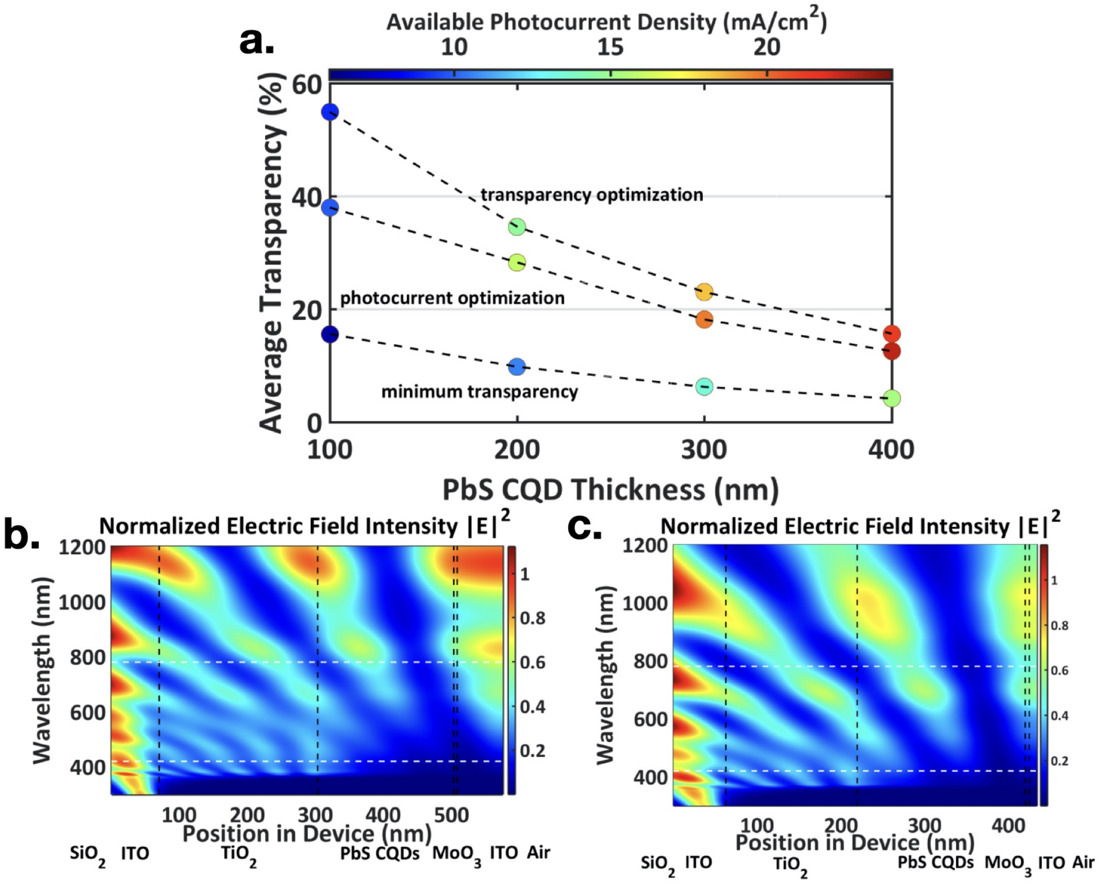

Figure 3-2. **a.** Calculated average transparency and corresponding available photocurrent density (color of the point) versus PbS CQD film thickness. Top curve: optimized for maximum average visible range transparency. Middle curve: optimized for maximum available photocurrent. Bottom curve: optimized for minimum average transparency. **b.** Calculated normalized field intensity as a function of wavelength and position across the device (ITO back contact) with a PbS CQD layer thickness of 200 nm for transparency-optimized case; **c.** for photocurrent-optimized case.

layer while maintaining absorption in the infrared. In order to achieve high photocurrent with minimum loss of visible transparency, optimization is performed on the layer thicknesses, with PbS CQD layer thickness kept constant. The three objectives chosen to explore the entire parameter space involved with the trade-off were high transparency, high photocurrent, and low transparency. The available photocurrent and average transparency of each solution to the three optimization problems are shown in **Figure 3-2a**

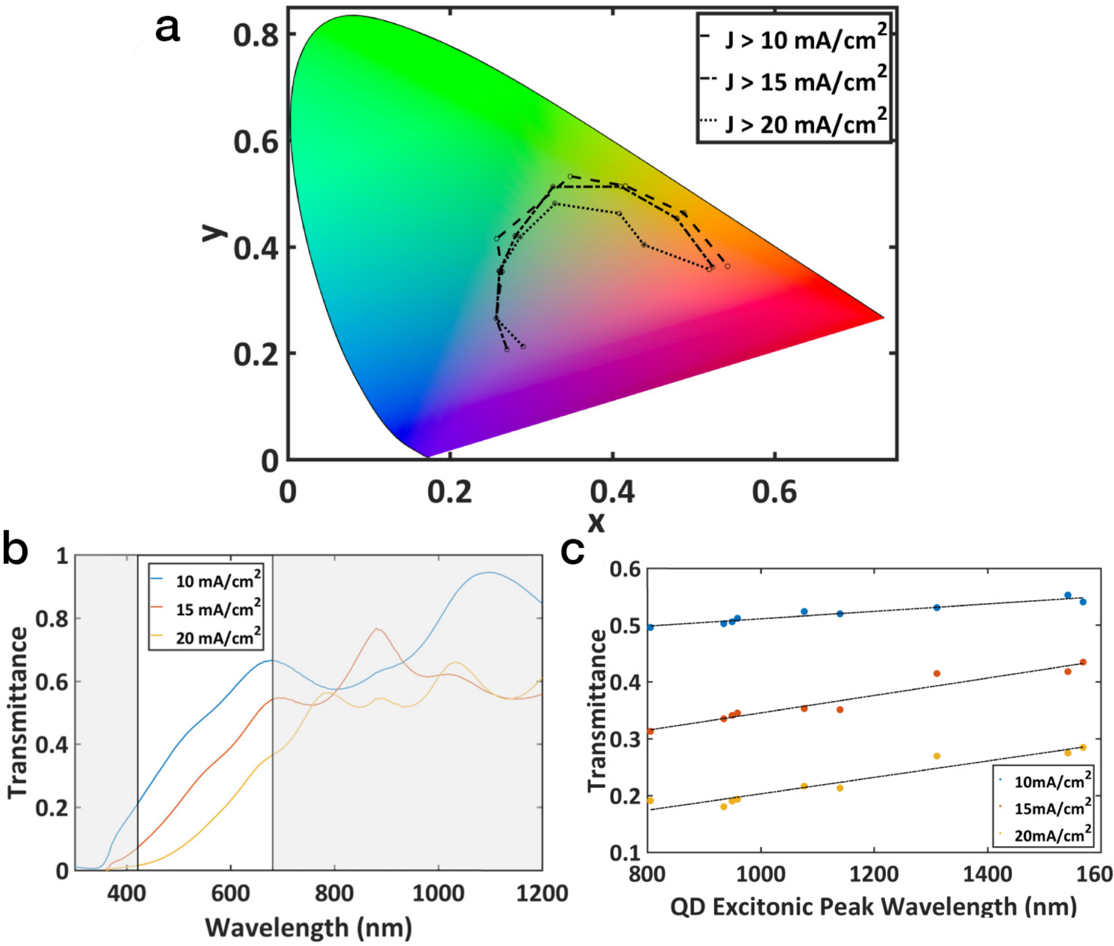

Figure 3-3. a. Chromaticity plot showing achievable colors given minimum photocurrent requirements. Calculated Transmittance plots showing: **b.** trade-off between transparency and photocurrent (for CQDs with 950 nm exciton peak wavelength), and **c.** achievable transparency given minimum photocurrent requirements for different CQD excitonic peak wavelengths.

Here, the average transparency is plotted as a function of CQD layer thickness, and the available photocurrent is represented by the color of the point. The top curve is the set of solutions at each given PbS CQD film thickness optimized for the transparency. The middle curve is optimized for the highest photocurrent at each film thickness. Higher photocurrent comes with the expected trade-off of lower transparency. The bottom curve is calculated for the lowest transparency, and it happens to have the lowest available photocurrent of the three sets of solutions. The difference between the lowest transparency curve and the highest photocurrent curve represents the achievable gain for both transparency and photocurrent from a well-formulated thickness optimization. Generally, the high photocurrent of the middle curve is achieved by maximizing the electric field strength within the active absorbing layer, while the high transparency of the top curve is achieved by minimizing the electric field strength in visible range within all the absorbing layers. These two targets are not completely opposite. The difference is visualized in **Figure 3-2b** and **Figure 3-2c**. In the optimized photocurrent case **Figure 3-2c**, there is an intensity peak at a wavelength near 700 nm within the CQD film, allowing more absorption and photogeneration. In the optimized transparency case **Figure 3-2b**, the peak electric field is shifted just out of the visible range to around 800nm, allowing visible light to be transmitted and maintaining photogeneration through NIR photon absorption.

The tradeoffs between attainable color or transparency and minimum device photocurrent are illustrated in **Figure 3-3a**. From this plot, it is apparent that photocurrent requirements more strongly affect “redder” colors, whereas the range of “bluer” colors that can be achieved shows little correlation with achievable photocurrent. **Figure 3-3b** shows transmittance plots for devices optimized for their transparency based on photocurrent restrictions. As expected, a lower required device photocurrent result in higher potential visual transparency. **Figure 3-3c** shows the dependence of the photocurrent/-transparency tradeoff on the CQD excitonic peak wavelength.

3.1.3 Effects of non-ideal layers on color saturation

In evaluating the prospects for real devices, it is important to take into account non-ideal effects, such as interface roughness, non-uniformity of the layer physical properties, and the presence of scattering centers formed by impurities and contaminants. We can incorporate these effects into our model by using another parameter, the effective “optical roughness” of each layer. We create a sufficiently large number of samples with random thicknesses by adding the standard deviation of a Gaussian distribution based on the measured or assumed roughness to the mean thickness for each layer. We then calculate the reflectance curve of each sample in the distribution and statistically average the reflectance from all samples to derive the effective reflectance curves.

Due to the nanostructured nature of the material itself as well as the deposition technique, the CQD layer typically has a geometrical roughness of 3-10 nm [31]. The geometrical roughness of the underlying electrodes and oxide layers deposited by evaporation, which can be determined from surface profilometry, is usually smaller than that of the CQD films. However, the effective optical roughness can be significantly greater than the geometrical roughness. One possible origin of optical inhomogeneity in the ITO and TiO^2 layers is the compositional and structural non-uniformity introduced during the deposition and processing steps, which can be seen as a spatial variation in the refractive index profile of the electrode films.

Figure 3-4 shows the effects of non-ideal interference on the reflectance curves as well as the effective colors of the devices. As can be seen in **Figure** 3-4**a**, the reflectance from devices with rough CQD layers is smoothened in the red spectral region, while the shorter-wavelength region is mostly unaffected by the roughness. For rough TiO_2 and ITO layers, the deviations from the ideal case are greater in the blue region. The changes in the reflectance curves reduce the wavelength selectivity, and make the apparent color less saturated. The chromaticity plot in **Figure** 3-4**b** demonstrates this effect for a device that is designed to be blue in color. As the effective optical roughness of the ITO/TiO_2 layer increases, the chromaticity point moves towards the white point, decreasing the saturation, and shifting the color towards brown-grey. In **Figure** 3-4**c**, after accounting for the optical roughness, all 3 points corresponding to the maximum achievable saturation of red, blue and green, are closer to the white point. This approach to considering the effects of non-ideal interference is particularly useful for understanding color in real devices.

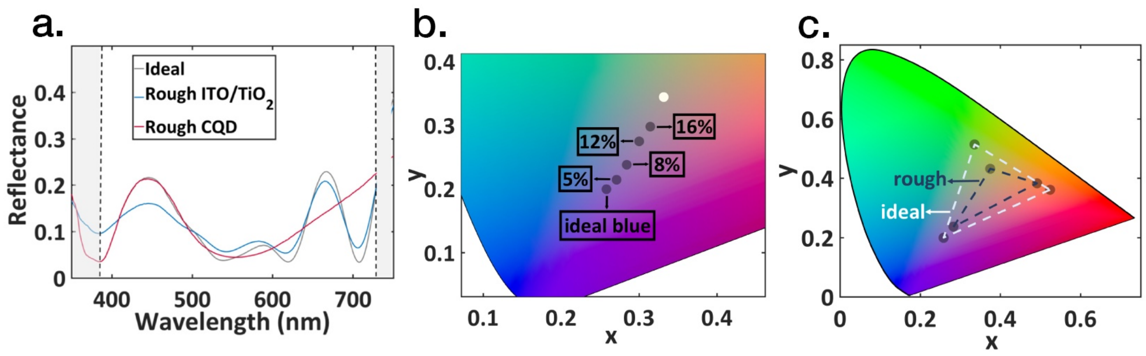

Figure 3-4. a. Simulated reflectance curves for a specific color objective with and without an effective optical roughness of 10% for the ITO/TiO_2 layers and 10% for the CQD layer. **b.** Effects of different levels of roughness on the chromaticity of a "blue" device. Percentages refer to the ratio of the standard deviation to the ideal thickness of the ITO/TiO_2 layer. The white point of the standard illuminant is referenced. **c.** The extent by which 10% roughness moves the largest achievable triangle of color profiles closer to the white point.

3.1.4 Results and Discussion

We fabricated several proof-of-principle CQD solar cell devices based on optimizations for different colors using PbS CQDs with exciton peak wavelengths near 950 nm. To minimize the fabrication uncertainty in the layer thicknesses, we used commercial ITO-coated glass substrates with ITO thicknesses of 28 nm for our "red" and "green" cell designs. For the "blue" cell, the ITO of desired thickness is deposited on a glass substrate with e-beam evaporation and properly annealed . The TiO_2 layer was also deposited using e-beam evaporation for precise thickness control, and a TiCl4 solution treatment was applied afterwards [32]. The PbS CQD layer was built up using a layer-by-layer solid state ligand exchange process [32]. PbS CQD solution at a concentration of 50 mg/mL were spin-cast on the substrate through a 0.22 μm filter,followed by soaking in 0.5% mercaptopropionic acid (MPA) methanol solution for 3 seconds to replace the oleic acid, and then the film was spin-cast dry. Lastly, the films were washed with methanol twice to remove the unbound ligands, completing the deposition of one CQD film layer. The total CQD film thickness

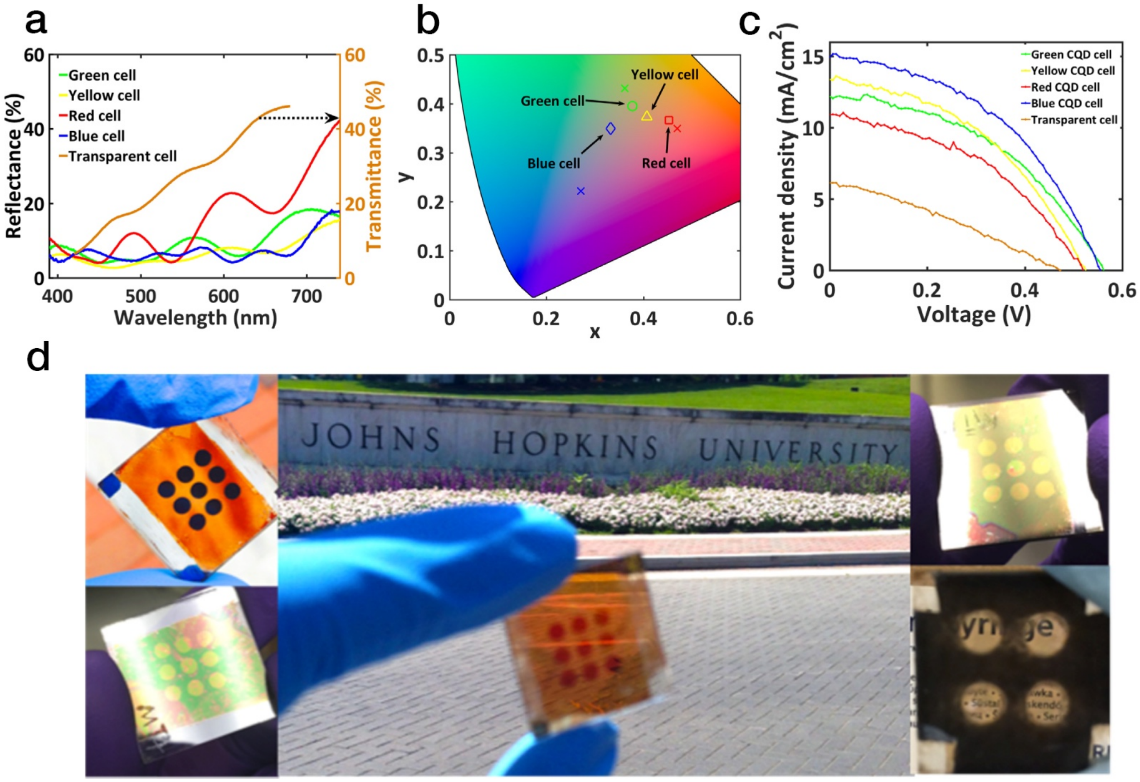

Figure 3-5. a. Experimental reflectance and transmittance spectra for colored and semi-transparent solar cells, respectively. **b.** Chromaticity plot showing the calculated coordinates for different colored devices. Crosses indicate design points while corresponding colored shapes indicate experimental points. **c.** J-V characteristics taken under simulated solar illumination for colored and semi-transparent devices. **d.** Photographs of blue (upper left), green (lower left), red (center), yellow (upper right), and semi-transparent (lower right) CQD solar cells.

under certain deposition condition is verified using profilometry measurements. We were able to control the thickness of the CQD layers to within +/-15 nm. The top contact was composed of a thin MoO3 buffer layer and Ag, which were deposited with controlled thicknesses using evaporation.

Photographs of the colored and transparent cells are shown in **Figure 3-5d**. We measured the reflectance of each solar cell under a integrating sphere-equipped spectrophotometer, calculated the corresponding Yxy color values under AM1.5 spectrum, and plotted them in a chromaticity diagram. The reflectance spectra are plotted in **Figure 3-5a**,

Type	V_{OC} (V)	J_{SC} (mA/cm^2)	FF	PCE	Thicknesses (ITO/TiO$_2$/PbS/ MoO$_3$/Ag)
Blue	0.55(11)	14.6(6)	0.44(1)	3.6(1)	240/113/400/100/475
Green	0.55(2)	12.1(7)	0.42(2)	2.8(1)	28/150/297/12/60
Yellow	0.53(1)	12.6(5)	0.41(1)	2.7(2)	28/150/297/12/60
Red	0.50(3)	10.3(8)	0.41(3)	2.1(3)	28/166/222/22/274
Transparent	0.46(5)	5.2(7)	0.31(1)	0.8(1)	28/349/170/17/85(ITO)

Table 3.1. Average performance characteristics of colored and transparent solar cell devices. Figures in the parentheses indicate the uncertainty at the least significant digit. All measurements are for at least 6 devices.

and the calculated color of the fabricated devices is shown in **Figure 3-5b**. For the semi-transparent device designed from the optimization, the top contact adopts a composite electrode consisting of spin-coated Ag nanowires and ITO nanoparticles. Our test devices had measured visible transparencies ranging from 27.3% to 32.2%. The measured JV curves of the highest efficiency device is plotted in **Figure 3-5c**.

All current density-voltage measurements were carried out in a nitrogen-purged environment with source-meter and solar spectrum simulator. The measured short circuit current (J_{SC}), open circuit voltage (V_{OC}), fill factor (FF), and power conversion efficiency (PCE) for the different cells are summarized in **Table 3.1**. Blue is a relatively difficult color to produce using this method, since the spectral range is absorbed the strongest in all layers, which renders the interference modulation less effective, and more subject to impact from random factors such as scatterings. The lower FF of the semi-transparent device is related to the difficulty in making a highly conductive top transparent contact without impact from heat-processing on the temperature -sensitive underlying CQD film. Generally, the experimental photocurrents were smaller than those predicted by the simulations by approximately 50-60%, due to deviations from the model assumptions. The simulations make the assumption of perfect carrier collection (IQE = 100%), whereas CQD solar cell IQE is typically on the order of 50-90% above the band gap [32, 33]. Additionally, experimental variations in the device layer thicknesses can contribute to lower average photocurrents. On average, the ITO, TiO_2, and PbS CQD layer thicknesses in our devices were within 15 nm, 10 nm, and 15 nm, respectively, of the design thicknesses.

3.1.5 Conclusion

We developed a method for producing customized spectral profiles in layered solar cell structures using thin film interference modulation techniques combined with optimization algorithms. At selected wavelengths, our model maximizes reflection a nd/or transmission to create a target color and transparency level while simultaneously maintaining sufficient photocarrier generation rates. Our study revealed that designs with minimum transparency do not necessarily correspond to the high photocurrent, providing a pathway for high efficiency colored devices. Although effective optical roughness in the films decreases the color saturation, CQD solar cell devices with well-defined color profiles can still be produced.

In addition, our optimization method can also serve as a better approach to solving the current match problem in tandem solar cells, as compared to the conventional calculation based on Beer-Lambert exponential law. Because of a more accurate calculated current generation profile, a higher attainable matched current density can almost always be achieved given the exact solution of layer thickness distribution. This is especially important for thin-film based CQD and other solution-processed tandem solar cells [34, 35], as the absorbing layer thicknesses, usually electronically optimized to be only a fraction of the absorption depths, create significantly stronger interference that causes the field to deviate from simple exponential profile.

Experimentally, we fabricated proof-of-principle blue, green, yellow, red and semi-transparent devices. The measured reflectance and transmittance spectra agreed well with the perceived color and transparency levels. Future work will focus on broadening the application of our model to hybrid materials systems (single junction and tandem design structures based on non-CQD-based films) and explicitly including additional loss mechanisms. Additionally, the overall device performance could be improved by employing the current best CQD device architecture strategies involving halide passivation strategies. [36, 37], with the corresponding device optical modeling readily covered with our method. Finally, this work, coupled with the development of more efficient room-temperature-processed transparent electrode materials, should extend the range of functionalities of flexible optoelectronic devices.

3.2 Spectral Selectivity in Absorbing Optoelectronic films via Photonic Crystal Band Engineering

This section is partially adapted from Ref[38]. Reprinted with permission from Optics Express 26, no. 21, pp. 26933-26945, ”Photonic band engineering in absorbing media for spectrally selective optoelectronic films,” by B. Qiu, Y. Lin, E. S. Arinze, A. Chiu, L. Li and S. M. Thon, copyright © 2018.

3.2.1 Introduction

Spectrally selectivity is one of the most critical foundations for countless modern optoelectronic applications. Its coverage ranges from lighting, display and optical imaging[39] that are closet to daily lives, to popular scientific research areas such as target recognition[40], gas detection [41, 42] and solar energy harvesting [43, 44]. Semiconductors, as the most closely related materials for such applications, however, is difficult to achieve adequate spectral selectivity since they typically absorb at all energies above their band gaps. Specific examples of technologies requiring fine-tuned spectral responsivity include finite bandwidth photodetectors and materials with controlled transparency windows for multijunction photovoltaics [35, 43, 45]. Spectral-selectivity can be employed for heat management in solar cells or other optoelectronic devices by reflecting unwanted wavelengths that would otherwise be parasitically absorbed in the contacts or other device layers. Common solutions to this problem include using external filters for photodetectors, which come with the cost of adding complexity to the system, and empirically controlling the thicknesses of each absorbing material in tandem solar cells to realize current matching, which often sacrifices photocurrent output [35, 46]. Here, we propose a solution that achieves controlled spectral selectivity within the absorbing material itself, i.e., the photogenerative material that is responsible for energy conversion or transfer of the absorbed photon energy: using photonic crystals to engineer the band structure in absorbing media to directly control the wavelength-dependent absorption, reflectivity and transmissivity.

Photonic crystals (PCs) are materials with periodic variations in their dielectric functions, potentially creating a photonic band gap, a range of frequencies in which photons are forbidden to propagate [47, 48]. This compelling mechanism enables PCs to be used to manipulate light flow in many optoelectronics applications [49–51]. In addition to artificial structures, many examples of PCs can be found in the natural world, enabling effects such as the structural colors of butterfly wings and beetles[52, 53].

Most of these examples use PCs with photonic band gaps lying in the naturally non-absorbing range of the materials, i.e., below the electronic band gap where the material behaves like a simple dielectric, although photonic band structures can be straightforwardly tuned in frequency by adjusting the length scale of the dielectric function periodicity (lattice constant) [47]. Positioning the photonic band gap of a PC in the absorbing region of a material presents complications due to absorption being viewed as a loss mechanism for many applications. However, optoelectronic applications such as photovoltaics or photodetectors rely on semiconductor absorption and photogeneration as vital operating mechanisms, and the possibility of using photonic crystal band engineering within the absorbing region represents a potential new spectral tuning mechanism. Previous work on engineering photonic band gaps in lossy materials includes forming PCs from metals that have shown diminished reflection peaks with increasing absorption [54]. Initial work on forming PCs within the photoactive layers for solar cells has been proposed, focusing on utilizing the PC structures for spectrally-selective light trapping[55] and absorption enhancement [55, 56] based on density of states modulation. For wavelength-selective absorption, band-pass absorbers made from dye-glass [57] have been widely implemented for decades, and in recent years, metamaterials based on periodic plasmonic structures have been demonstrated with very high absorbance within the visible range for solar-thermal applications[58]. These implementations typically focus on engineering responses in different spectral ranges based on the respective structures. However, rather than focusing on absorption alone, a comprehensive method for inducing spectral-selectivity that aims to enable wavelength- dependent absorption, reflectivity and transmissivity simultaneously, including not just absorption enhancement but also suppression through the use of controlled transparency windows, has yet to be demonstrated. Here, we describe PCs embedded in photogenerative materials could offer a handle for controlling spectral features across multiple wavelength bands and dynamic ranges in complicated optoelectronic systems.

Spectral-selectivity is particularly applicable for the design of color-tuned materials with controlled transparency windows for multijunction and transparent photovoltaics. Infrared (IR) sensitive materials, such as small-bandgap semiconductors, absorb strongly at all energies above their band gaps. Molecular materials, such as organic semiconductors, typically have finite-bandwidth absorption in the visible and UV, but IR-only responsive materials are rare. To incorporate IR-sensitive materials into multijunction solar cells, they must be positioned at the back side of a standard solar cell device to permit the absorption of visible radiation by the front cell, and the thicknesses of both cells

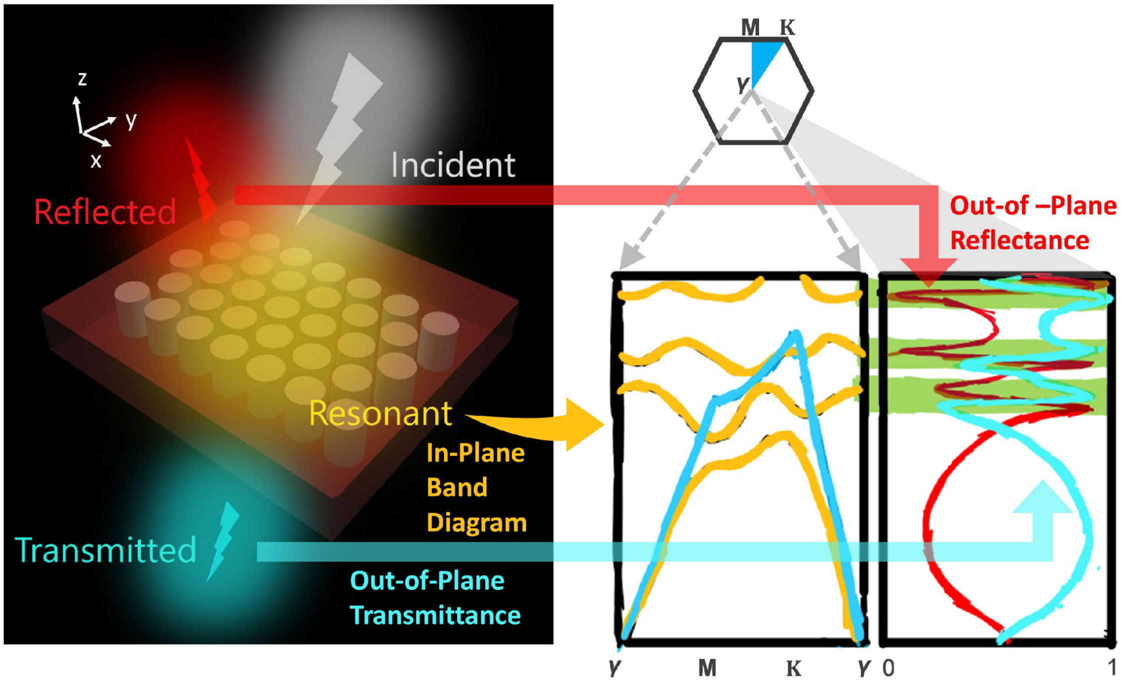

Figure 3-6. Schematic of a generic 2D slab photonic crystal illustrating the spectral tuning concept (left). The photonic slab can be used to generate selective reflectivity, transmissivity and absorption for target optoelectronic applications. Broadband light (white in color) is incident on the slab, with specific frequency components strongly coupled to the resonance modes of the slab (yellow), resulting in spectrally-selective transmission (blue) and reflection (red). A hypothetical photonic band diagram for the generic slab structure (photonic bands are shown in yellow; the light line is shown in blue in the center panel) and transmittance (blue) and reflectance (red) spectra at normal incidence are sketched on the right side. The green stripes show direct correlations (coupling) between the sharp resonance features in the transmittance and reflectance spectra and the photonic band states at the γ-point. A corresponding Brillouin Zone diagram for the structure is shown atop the band diagram sketch.

must be fine-tuned to achieve current-matching. An ideal material for incorporating multijunction functionality into current single junction photovoltaic technology would have an absorption profile that was both spectrally tunable and finite in bandwidth, thus offering flexibility for both current-matching and device design. The concept of using the band structure in a slab-type PC to control the reflection and transmission of external propagating fields is illustrated in **Figure** 3-6. Here, we present a system consisting of a 2D PC "slab" structure in which a periodic lattice of air holes is drilled in a semiconductor. The incident, reflected, and transmitted fields are highlighted and interact with the interior resonant field with spatial and temporal properties determined by the PC structure. Here, we use "in-plane" to describe physical structures or fields and states that are bound by or mostly concentrated in the slab itself, and "out-of-plane" to describe fields and waves that propagate indefinitely outside of the slab structure. The "in-plane" fields and states compose the band structure of the slab, and they can couple to the "out-of-plane" incident waves at the γ point of the Brillouin Zone, shown on the right side of **Figure** 3-6. We sketch hypothetical reflection and transmission spectra at normal incidence alongside a hypothetical (generic) in-plane band diagram for a structure such as that shown in **Figure** 3-6 to illustrate the coupling between the in-plane photonic bands and the out-of-plane reflection and transmission profiles. The transmission and reflection spectra should consist of a smoothly varying background that resembles a Fabry-Perot interference spectrum [59] with sharp and asymmetric resonance features on top. As will be discussing in the next section, the coupling between incident waves and the photonic bands sharing a lateral wave-vector results in resonance features in the transmission and reflection spectra of the slab. This coupling gives rise to the potential for tuning the "out-of-plane" spectral selectivity by tailoring the band structure of the PC slab, to achieve desired absorption, reflection and transmission profiles.

In this work, we use finite-difference time-domain (FDTD) simulations and Fourier modal methods (FMM) [60–62] to quantify the effect of material absorption on a slab PC with relevant photonic bands that fall above the electronic band gap of the semiconductor slab material. The study shows that by careful choice of a photogenerative material, and tuning the physics of resonance between the field and periodic material structure, simultaneous modulation and hence spectral selectivity of all spectrum can be achieved inside thin-film layered structures that are particularly useful for optoelectronic applications.

3.2.2 Simulation Setup and Results

To study the effect of material absorption on PC band structure, we first based our simulations on the well-studied 2D GaAs slab PC structure[48], which consists of a triangular lattice of air pillars in a semiconductor slab of finite thickness. In FDTD simulations, the strength of the absorption is adjusted through control of the imaginary part of the dielectric constant ϵ_I, with the real part ϵ_R kept constant, which is also equivalent to varying the real and imaginary parts of the refractive index (n, k). Dispersion is not explicitly considered in the test-case model since it results in difficulty in satisfying the Kramers-Kronig relations [63–65]. The completely non-absorbing control case uses a material that has ϵ_R set to 13, meant to approximate the average value of n for GaAs across the relevant frequency range, and ϵ_I set to zero. We then gradually increase the value of ϵ_I in the simulations, keeping ϵ_R constant, in order to systematically quantify the effect of dissipation on the photonic band structure.

We use FDTD simulations to reconstruct the PC band structures of our artificial material. Specifically,a broadband source is used to excite all possible modes in the structure. Randomly distributed time monitors collect the temporal field data, collecting modes that resonate with the structure and last beyond the initial transients. The frequencies of these modes are extracted via apodized Fourier transformation (FT) of the temporal signal.

Details of the FDTD simulation method for band structure simulations are as follows: The simulation volume consists of an integer number of unit cells of the 2D slab periodic structure, and the volume is extended in the z-direction symmetrically above and below the slab by approximately 10 lattice constants to eliminate boundary effects. Bloch boundary conditions are used for the x and y (in-plane) directions and perfectly matched layers (PMLs) with symmetric or anti-symmetric boundary conditions are used in the simulations corresponding to the even (TE-like) or odd (TM-like) mode with respect to z-axis. Identical broadband dipole sources with random polarizations are used to excite the modes and randomly distributed throughout the simulation volume. Conformal meshing is used near material interfaces, and the integral form of Maxwell equations are used to account for structural variations within a single mesh cell. The monitored temporal fields are apodized with a Gaussian-shaped windowing function, to only consider the portion of the time signal following the source pulse injection and before the simulation is cut off. The resulting FT of the apodized signal is a spectrum with peaks at the resonant mode frequencies, corresponding to allowed photonic bands. The energy spectra of Fourier-transformed signals for each field component of every time monitor are summed to ensure all of the resonant are identified, even if some of the randomly placed time monitors are located close to the node of certain modes. The simulations are repeated for each Bloch vector value, $\mathbf{k}$, and frequency peaks for each $\mathbf{k}$ that meet the intensity threshold are retained.

In our simulations, we chose a semiconductor slab thickness of 125 nm and adjusted the lattice constant (a = 250 nm) and radius (r = 60 nm) of the air holes to produce a number of relevant PC bands within the visible regime, or above the electronic band gap of GaAs. The model structure is shown in the inset of **Figure 3-7a**. The simulated band structure for the non-absorbing control case with both even and odd modes is shown in the top left panel of **Figure 3-7a**, followed by a series of photonic band structures with increasing k. The photonic band structure for a GaAs PC slab including full dispersion [66] in the refractive index model is shown in **Figure 3-7b**.

As can be seen from **Figure 3-7a**, the frequencies of the photonic bands are almost unchanged as dissipation is added to the optical model, if ϵ_I remains small compared to ϵ_R, although the relative band strengths are reduced with increasing material absorption. As material loss increases, the widths of the bands are broadened, and the clarity of the higher order bands decreases faster than that of the lower order bands, which is expected from the shorter absorption lengths at higher frequencies present in the model. The rough

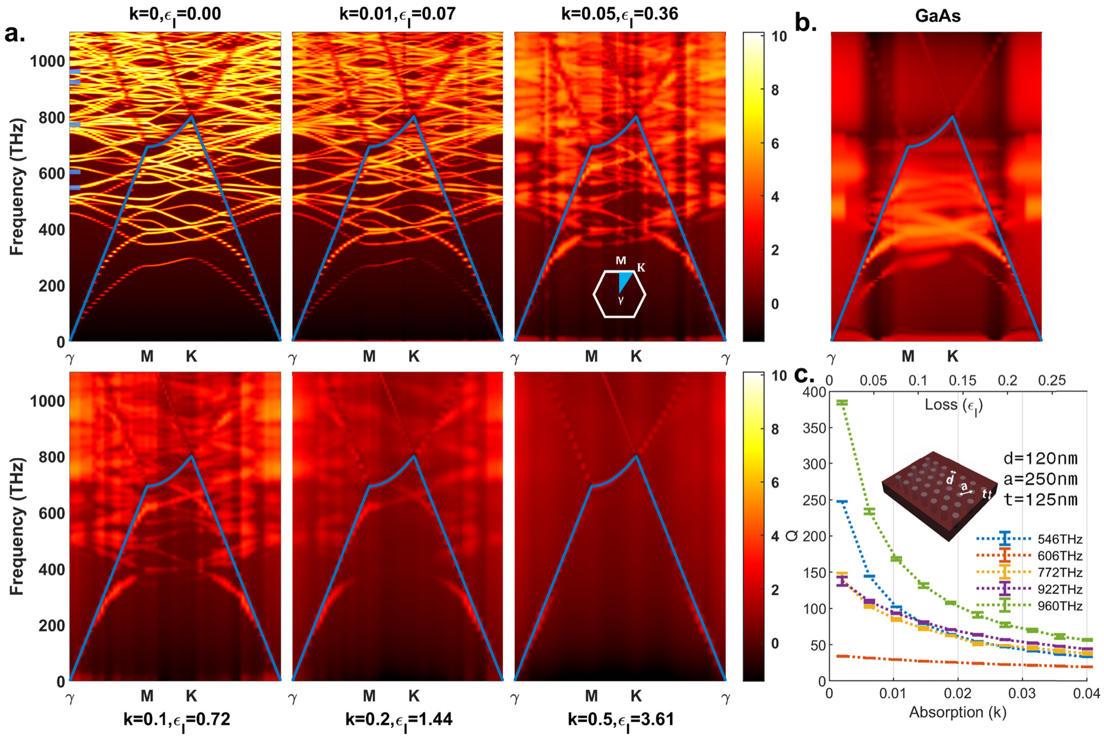

Figure 3-7. a. FDTD- calculated PC slab bandstructure for the structure shown in **c.** with media loss (absorption) varying from $\epsilon_I = 0$ to $\epsilon_I = 3.61$ and constant $\epsilon_R = 13$, The light lines are plotted in blue. The color scale is in arbitrary logarithmic units corresponding to the field intensity. **b.** FDTD-calculated photonic band diagram for the same structure for a GaAs slab. **c.** Quality factor of 5 selected modes, indicated by the blue markings at the γ point in the top left panel of **a.**, as a function of loss in the material. Inset: model of the simulated structure, a triangular lattice of air holes in a semiconductor slab with 120 nm diameter, 250 nm lattice constant, and 125 nm slab thickness.

maintenance of the photonic band frequencies in the presence of weak material loss can be understood using perturbation theory applied to the PC master equation[48]. Adding a small imaginary part to the dielectric function ϵ, results in the addition of an imaginary part to the resonance frequency, $\omega_0 = \omega_0 - i\gamma$, which consequently adds to the linewidth of the Lorentzian resonance profile and reduces the resonance peak height.

To quantitatively study the properties of photonic bands in dissipative structures, we calculated quality factors, Q, for the individual bands in the structure shown in **Figure 3-7**: $Q_i = \frac{\omega_0}{\Gamma_i}$, where Γ_i is the energy decay rate, or the band resonance linewidth, of the

i^{th} photonic band at the γ point of the periodic structure. Modes at the γ point are above the light line, and because of the finite thickness of the PC slab, they are radiating modes at that point that can couple to external propagating fields. Here, we chose five modes capable of coupling to plane waves at normal incidence angles, i.e., they can be excited by incident plane waves and radiate energy to reflected and transmitted plane waves. For this reason, these bands dissipate energy from the slab and have finite Q even without the presence of material absorption. **Figure 3-7c** shows the quality factors for the five bands as a function of increasing ϵ_I or k in the material. All quality factors exhibit similar decays as a function of ϵ_I and can be well fitted by the function $Q_i = \frac{Q_0 \Gamma_0}{\Gamma_0 + \alpha_i \epsilon_I}$, where Q_0 is the quality factor of the lossless structure, and α_i is a constant that depends on the spatial distribution of the ith mode[48]. As loss in the material (ϵ_I) increases, the differences in Q between different modes decrease, corresponding to a "smearing" and overlapping of the photonic bands until they eventually become indistinct at the limit of very high material absorption.

Understanding the interactions of external propagating fields with the in-plane photonic band structure of a slab-like PC, specifically the spectral reflection and transmission of a PC thin film, is a critical step in using them for absorbing optoelectronic applications. These interactions involve power transfer from external fields to radiating modes within the slab and vice versa. Such systems can be modeled as resonators interacting with external ports using coupled-resonator theories [67]. In PC thin films of interest for optoelectronic applications, the periodicities are always smaller than the wavelengths of interest; therefore, for plane wave sources, no diffraction orders exist. Consequently, all fields and modes that interact with an incident wave are contained in the reflected and transmitted waves with the same in-plane wave vector as the incident wave, and the in-resonance slab radiating modes. Waves impingent at normal incidence on a slab-PC therefore compose a system that can be fully and concisely modeled.

Figure 3-8 shows transmission and reflection spectra for absorbing and non-absorbing

PC structures calculated via Fourier modal methods[60–62] at a fixed in-plane wave vector with polarization along one of the reciprocal lattice vectors. The smoothly-varying background curve resembles the spectrum from a simple Fabry-Perot cavity consisting of a uniform continuous media sandwiched between two mirrors, with additional sharp resonance features added on top. The resonances occur at the same frequencies as the in-plane PC radiating modes and are asymmetric with negative and positive features due to the nature of Fano resonance behavior[67]; these features include dramatic increases in transmission on one side of the resonance, even in the case with material absorption. The transmitted and reflected fields directly couple to the incident field while simultaneously indirectly coupling to the radiating mode of the photonic crystal excited by the incident field. Such resonance phenomena are well explained by temporal- coupled wave theory[67–69]. We note that not all modes in the photonic band structure can be excited with incident plane waves, due to restrictions in symmetry and polarization[67].

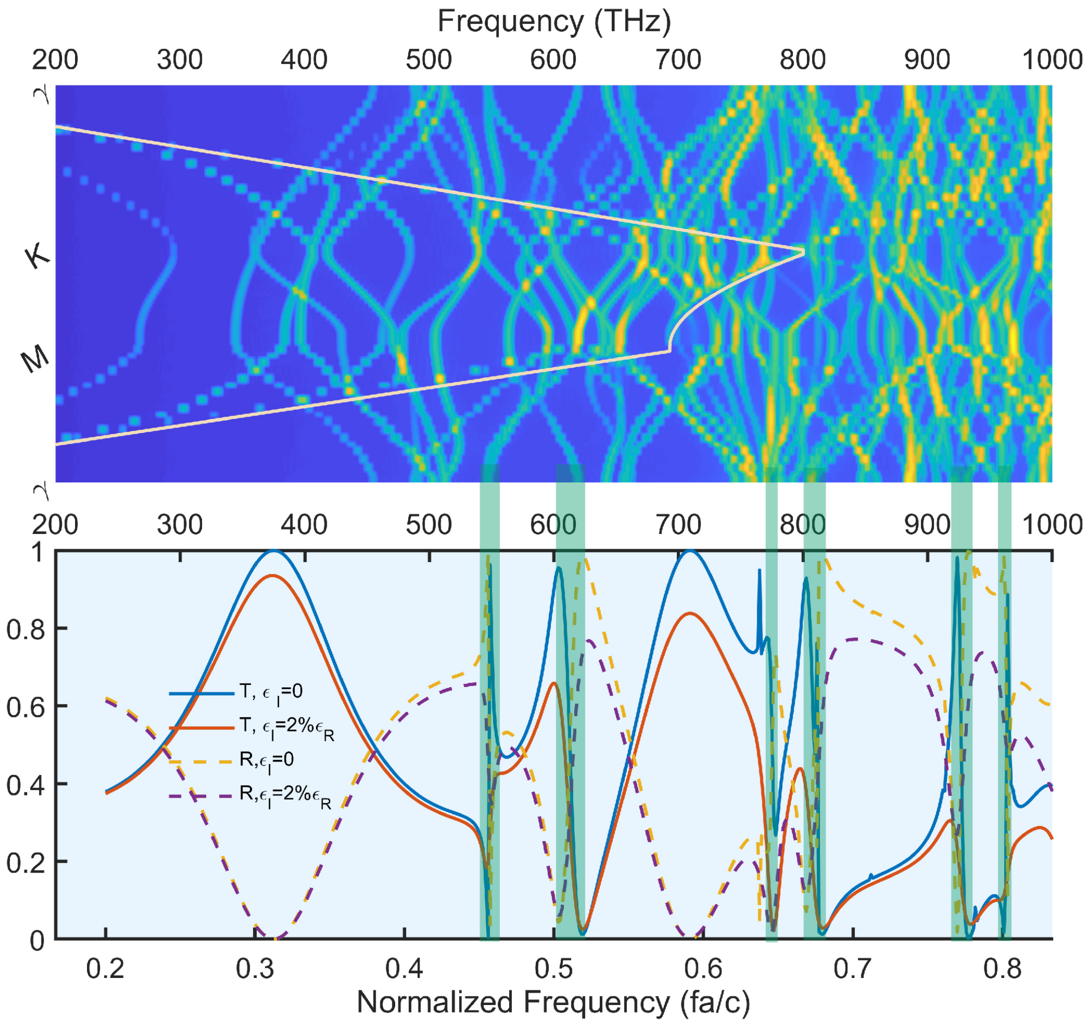

Figure 3-8. FMM-calculated transmission (solid lines) and reflection (dashed lines) spectra (bottom) for a triangular lattice slab PC with $r = 0.24a$, $t = 0.5a$ and $\epsilon = 13$ (blue and yellow spectra) and $\epsilon = 13 + 0.3i$ (red and purple spectra). The incident field is perpendicular to the slab structure. The corresponding FDTD-calculated band structure for the $\epsilon = 13$ case is shown in the top panel (light line plotted in white). The resonance regions are highlighted and associated with the modes at the Γ point in the band structure.

In the absence of absorption, the Fano resonance features are narrow and sharp, due to the intrinsic long lifetimes of the lossless radiating modes. When absorption is added to the model, the lifetimes of the radiating modes are reduced, resulting in broader and weaker resonance features, which originate from the same effects as the reduction in Q factor seen for the modes in the band structures. The resonance frequencies for the same structure with a non-zero ϵ_I, set to 2% of ϵ_R, are almost unchanged, in accordance with the FDTD photonic band structure simulations. The FDTD-calculated photonic band structure for the $\epsilon_R = 0$ case is plotted next to the reflection and transmission spectra in **Figure** 3-8 illustrate direct spectral correspondence between the out-of-plane Fano resonance features and the in-plane photonic crystal bands. The overall reflection and transmission are both slightly reduced in the case with absorption compared to the case without absorption, as would be expected for a uniform lossy slab.

Although the resonance features are less apparent in the transmission and reflection spectra of the absorptive structure, the interactions of the PC medium with the radiating resonance modes are not necessarily weakened. Applications such as photovoltaics and photocatalysis that depend on absorption of the photoactive material could benefit from this phenomenon of increased absorption of the resonance modes. The amplitude of the ith steady-state resonance mode in the presence of material absorption can be approximated from temporal-coupled wave theory as shown below[68, 70]:

$$a_i = \frac{gs}{i(\omega - \omega_0) + \Gamma_{\text{rad,i}} + \Gamma_{\text{abs,i}}} \tag{3.1}$$

where g and s are the coupling strength and the amplitude of the incident field, respectively; ω_0 is the resonance frequency; and Γ_{rad} and Γ_{abs} are the decay rates, i.e., the reciprocals of the radiation and absorption lifetimes. The power absorbed in the i^{th} mode is therefore approximated as:

$$P_{\text{abs}} \propto \Gamma_{\text{abs}}|a_i|^2 = \frac{\Gamma_{\text{abs}}|g|^2|s|^2}{(\omega - \omega_0)^2 + (\Gamma_{\text{rad,i}} + \Gamma_{\text{abs,i}})^2} \tag{3.2}$$

which can be maximized at the resonance frequency ω_0, if the absorption strength is comparable to the radiative strength. In the presence of material absorption, the widths of the resonances are also broadened so that a larger range of frequencies is capable of inducing stronger absorption in the media. Additionally, the integrated absorbed power associated with a specific resonance (photonic band) always increases with increasing material absorption strength.

Based on this analysis, using 2D PC slabs in absorptive materials should enable spectral modulation, including absorption and transmission tuning, with careful control of the PC parameters. Broadband transmission and reflection selectivity is controlled primarily by the average optical properties of the slab, i.e., the effective refractive index. The smoothly varying background in the reflection spectra can be very accurately fitted assuming an optically uniform slab with slight dispersion in the dielectric constant that varies around the average dielectric constant of the PC slab. Broadband transmission and reflection tuning is therefore effectively only dependent on the volume ratio of the periodic voids (low-index inclusions), the slab thickness, and the properties of the high-index material. The spectral locations of the sharp resonant features corresponding to the photonic bands within the material, on the other hand, are highly dependent on the PC structural properties, such as the periods and shapes of the voids, not on the slab thickness and high-to-low index material volume ratio. Additionally, due to the optical scalability of PC structures in the absence of strong dispersion, specific spectral features can be easily shifted to preferred frequency ranges simply by scaling the structure accordingly. The addition of material absorption allows abrupt spectral features to be smoothed and broadened without significant shifts in frequency or decreases in the absorbed incident power, an additional tool that can be used to tailor transmission and reflection profiles.

3.2.3 Experimental Demonstration

To further explore the transmission and reflection tunability indicated from the theoretical analyses, we sought to experimentally demonstrate this mechanism by fabricating a proof-of-principle PC structure in a strongly absorbing material with response in the infrared portion of the spectrum. PbS CQD thin films are used because of its facile solution processability and its broad involvementWe in various optoelectronics including LED, photodetectors and solar cells. Nanosphere self-assembly [71, 72] is used to construct a monolayer triangular lattice out of polystyrene beads, which served as the low-index material, and is infiltrated with PbS CQDs as the high-index absorbing material to form a PC structure. FDTD is used for optimization of the transmittance in the visible regime for this PC-CQD film. To mimic the realistic system, we incorporate slight non-uniformity in the large-scale film thicknesses. We calculated the transmission by averaging the simulation results for 11 different film thicknesses for PC-CQD (250(50) nm) and 3 different film thicknesses for the CQD control (200(10) nm), of which the uncertainties are based on our experimental thickness measurements. As shown in **Figure 3-9a-b**, the PC-CQD film consisting of 250 nm beads infiltrated with PbS CQDs displays a slight enhancement in visible transparency and a decrease in near-infrared (NIR) transparency compared with the CQD control in both the simulation and the experiment. The electrical field profiles at the transmittance peak and valley of the 250 nm PC-CQD film are shown in **Figure 3-9c-d**, respectively. At the transmittance peak, the field is mainly confined within the low-index dielectric material, whereas at the valley, the field overlaps more with the absorbing media and hence higher absorption.

To fabricate the PC-CQD film, we started by hydrophilic treatment with oxygen plasma of the glass substrates. The compact triangular beads arrays were self-assembled following spin-cast deposition with the aqueous suspension of polystyrene beads. We then applied an oxygen plasma etching procedure to adjust the ratio of the radius-to-lattice constant. A scanning electron microscope (SEM) image of the bead array after etching is shown **Figure 3-9e**, and the inset contains a photograph of the sample. The iridescence from the structure indicates the existence of large-scale PC structure. We synthesized oleic-acid capped PbS CQDs following methods discussed in previous sections [73] and deposited the control CQD films from octane solutions, which is then treated via a layer-by-layer 3-mercaptopropionic acid (MPA) ligand exchange process[74] to build

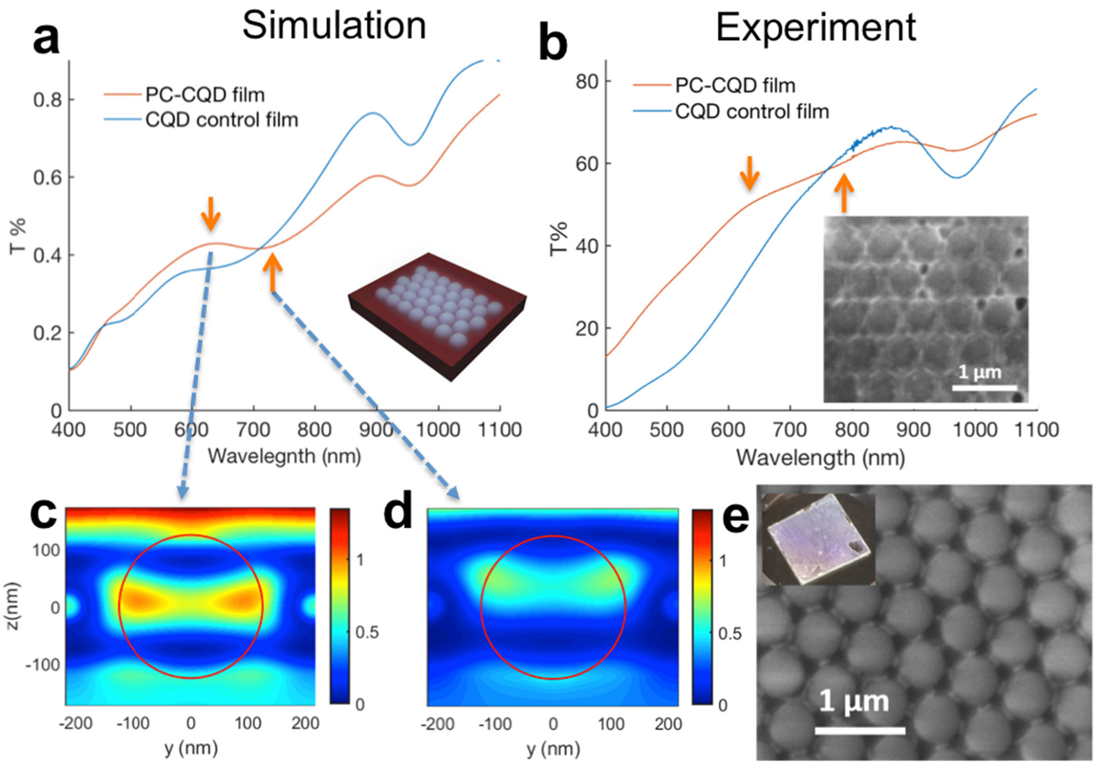

Figure 3-9. a. Simulated transmittance for a control CQD film and a PC-CQD film. The inset is the PC-CQD structure. The CQD control is 200 nm thick on average, and the PC-CQD film consists of 250 nm diameter beads with a lattice constant of 250 nm. The spectra are averaged over several thicknesses to simulate the effect from roughness. **b.** Transmittance spectra of the PC-CQD film and the CQD control; Inset: SEM image of the PC-CQD structure. **c.** FDTD-calculated cross-section profile of the electric field at the transmittance peak **d.** valley. **e.** SEM image of the bead array before CQD infiltration. The inset is a photo of the bead array on a 25 mm × 25 mm glass substrate before CQD infiltration.

up a film of the desired thickness. We used a lower concentration CQD solution while keeping the concentration of the MPA solution to promote infiltration of the CQDs into the bead array. An SEM image of the PC-CQD film is shown in the inset of **Figure 3-9b**. Optical transmittance spectra of the PC-CQD and control films are shown in **Figure 3-9b**, measured using integrating sphere in a UV-Vis-NIR spectrophotometer. The experimental data is in rough qualitative agreement with the FDTD simulation results. The peaks and valleys of the experimental spectra are broadened and reduced compared to the simulation, most likely due to non-uniformity across the films and significant surface roughness that results in reduction of spectral tuning effect.

3.2.4 Summary and Outlook

We developed and analyzed a strategy for tuning the spectral selectivity of optoelectronic thin films: using PC band engineering in absorbing materials in which the in-plane photonic energy bands interaction with out-of-plane reflection and transmission fields are used to control the spectral properties of all related fields. We analyzed a model system composed of a semiconductor-based 2D slab PC in which the photonic energy bands of interest reside in the absorbing region of the material. With the help of FDTD and FMM simulations to compare the effects from varying absorption strength, we were able to quantify the impact of absorption on the photonic band structure. Specifically, adding absorption had little impact on the frequency of the PC states, although the widths of the bands were broadened and the quality factors of the in-plane modes decreased as a natural result of the additional increased energy dissipation rate. Our FMM analysis showed that coupling between the PC band states at the reciprocal lattice point and an incident wave with corresponding lateral wave-vector induces sharp Fano resonance features and the associated variations over the smoothly varying background in the reflection and transmission spectra, which is preserved even in the presence of material absorption. These results indicate that PC structures in strongly absorbing media can be used to produce spectrally selective optoelectronic thin films for targeted applications by careful adjustment of the lattice parameters.

Experimentally, we demonstrated the use of photonic structuring as a transmittance tunning mechanism in a strongly absorbing material by fabricating a proof-of-principle structure consisting of a self-assembled polystyrene bead monolayer array infiltrated with PbS CQDs. The PC-CQD structure showed both NIR absorption enhancement and visible transparency enhancement over the CQD control of the same thickness, qualitatively matching predictions.

Future work will focus on extending these results by utilizing the full PC band structures for solution-processed systems and including other realistic factors such as dispersion in the optical models. We will use the insights gained from this study to design spectral-selective photoactive optoelectronic films for targeted applications such as narrow-band infrared photodetectors and infrared solar cell materials for multijunction photovoltaics. The platform described here should form the basis for a new strategy about using PC band structure engineering to control the spectral selectivity of systems with strongly absorbing materials.

References

[1] E. S. Arinze, B. Qiu, N. Palmquist, Y. Cheng, Y. Lin, G. Nyirjesy, G. Qian, and S. M. Thon, "Color-tuned and transparent colloidal quantum dot solar cells via optimized multilayer interference," Optics Express **25**, A101–A112 (2017).

[2] A. Henemann, "BIPV: Built-in solar energy," Renewable Energy Focus **9**, 14–19 (2008).

[3] A. G. Hestnes, "Building Integration Of Solar Energy Systems," Solar Energy **67**, 181–187 (1999).

[4] H. Davidsson, B. Perers, and B. Karlsson, "Performance of a multifunctional PV/T hybrid solar window," Solar Energy **84**, 365–372 (2010).

[5] T. Miyazaki, A. Akisawa, and T. Kashiwagi, "Energy savings of office buildings by the use of semi-transparent solar cells for windows," Renewable Energy **30**, 281–304 (2005).

[6] H. Otaka, M. Kira, K. Yano, S. Ito, H. Mitekura, T. Kawata, and F. Matsui, "Multi-colored dye-sensitized solar cells," Journal of Photochemistry and Photobiology A: Chemistry, Proceedings of the Dye Solar Cell Osaka ICP-21 Pre-Symposium. Dedicated to Professor Shozo Yanagida on the Occasion of His Retirement **164**, 67–73 (2004).

[7] H. J. Park, T. Xu, J. Y. Lee, A. Ledbetter, and L. J. Guo, "Photonic Color Filters Integrated with Organic Solar Cells for Energy Harvesting," ACS Nano **5**, 7055–7060 (2011).

[8] G. E. Eperon, V. M. Burlakov, A. Goriely, and H. J. Snaith, "Neutral Color Semitransparent Microstructured Perovskite Solar Cells," ACS Nano **8**, 591–598 (2014).

[9] Y. Guo, K. Shoyama, W. Sato, and E. Nakamura, "Polymer Stabilization of Lead(II) Perovskite Cubic Nanocrystals for Semitransparent Solar Cells," Advanced Energy Materials **6**, 1502317 (2016).

[10] Y.-H. Kim, H. Cho, J. H. Heo, T.-S. Kim, N. Myoung, C.-L. Lee, S. H. Im, and T.-W. Lee, "Multicolored Organic/Inorganic Hybrid Perovskite Light-Emitting Diodes," Advanced Materials **27**, 1248–1254 (2015).

[11] C. Li, J. Sleppy, N. Dhasmana, M. Soliman, L. Tetard, and J. Thomas, "A PCBM-assisted perovskite growth process to fabricate high efficiency semitransparent solar cells," Journal of Materials Chemistry A **4**, 11648–11655 (2016).

[12] Y. Galagan, M. G. Debije, and P. W. M. Blom, "Semitransparent organic solar cells with organic wavelength dependent reflectors," Applied Physics Letters **98**, 043302 (2011).

[13] W. Zhang, M. Anaya, G. Lozano, M. E. Calvo, M. B. Johnston, H. Míguez, and H. J. Snaith, "Highly Efficient Perovskite Solar Cells with Tunable Structural Color," Nano Letters **15**, 1698–1702 (2015).

[14] C. O. Ramírez Quiroz, C. Bronnbauer, I. Levchuk, Y. Hou, C. J. Brabec, and K. Forberich, "Coloring Semitransparent Perovskite Solar Cells via Dielectric Mirrors," ACS Nano **10**, 5104–5112 (2016).

[15] K.-T. Lee, M. Fukuda, S. Joglekar, and L. J. Guo, "Colored, see-through perovskite solar cells employing an optical cavity," Journal of Materials Chemistry C **3**, 5377–5382 (2015).

[16] J. Krantz, T. Stubhan, M. Richter, S. Spallek, I. Litzov, G. J. Matt, E. Spiecker, and C. J. Brabec, "Spray-Coated Silver Nanowires as Top Electrode Layer in Semitransparent P3HT:PCBM-Based Organic Solar Cell Devices," Advanced Functional Materials **23**, 1711–1717 (2013).

[17] Y.-Y. Lee, K.-H. Tu, C.-C. Yu, S.-S. Li, J.-Y. Hwang, C.-C. Lin, K.-H. Chen, L.-C. Chen, H.-L. Chen, and C.-W. Chen, "Top Laminated Graphene Electrode in a Semitransparent

Polymer Solar Cell by Simultaneous Thermal Annealing/Releasing Method," ACS Nano **5**, 6564–6570 (2011).

[18]S. Adachi, "Lead Sulphide (PbS)," in *Optical Constants of Crystalline and Amorphous Semiconductors: Numerical Data and Graphical Information*, edited by S. Adachi (Springer US, Boston, MA, 1999), pp. 613–621.

[19]J. N. Zemel, J. D. Jensen, and R. B. Schoolar, "Electrical and Optical Properties of Epitaxial Films of PbS, PbSe, PbTe, and SnTe," Physical Review **140**, A330–A342 (1965).

[20]E. H. Sargent, "Colloidal quantum dot solar cells," Nature Photonics **6**, 133–135 (2012).

[21]X. Zhang, C. Hägglund, M. B. Johansson, K. Sveinbjörnsson, and E. M. J. Johansson, "Fine Tuned Nanolayered Metal/Metal Oxide Electrode for Semitransparent Colloidal Quantum Dot Solar Cells," Advanced Functional Materials **26**, 1921–1929 (2016).

[22]O. Ouellette, N. Hossain, B. R. Sutherland, A. Kiani, F. P. García de Arquer, H. Tan, M. Chaker, S. Hoogland, and E. H. Sargent, "Optical Resonance Engineering for Infrared Colloidal Quantum Dot Photovoltaics," ACS Energy Letters **1**, 852–857 (2016).

[23]S. Akhavan, B. Guzelturk, V. K. Sharma, and H. V. Demir, "Large-area semi-transparent light-sensitive nanocrystal skins," Optics Express **20**, 25255–25266 (2012).

[24]X. Zhang, G. E. Eperon, J. Liu, and E. M. J. Johansson, "Semitransparent quantum dot solar cell," Nano Energy **22**, 70–78 (2016).

[25]G. F. Burkhard, E. T. Hoke, and M. D. McGehee, "Accounting for Interference, Scattering, and Electrode Absorption to Make Accurate Internal Quantum Efficiency Measurements in Organic and Other Thin Solar Cells," Advanced Materials **22**, 3293–3297 (2010).

[26]L. A. A. Pettersson, L. S. Roman, and O. Inganäs, "Modeling photocurrent action spectra of photovoltaic devices based on organic thin films," Journal of Applied Physics **86**, 487–496 (1999).

[27] P. Peumans, A. Yakimov, and S. R. Forrest, "Small molecular weight organic thin-film photodetectors and solar cells," Journal of Applied Physics **93**, 3693–3723 (2003).

[28] K. Deb, "Multi-objective Optimisation Using Evolutionary Algorithms: An Introduction," in *Multi-objective Evolutionary Optimisation for Product Design and Manufacturing*, edited by L. Wang, A. H. C. Ng, and K. Deb (Springer, London, 2011), pp. 3–34.

[29] J. Kennedy, "Particle Swarm Optimization," in *Encyclopedia of Machine Learning*, edited by C. Sammut and G. I. Webb (Springer US, Boston, MA, 2010), pp. 760–766.

[30] T. Smith and J. Guild, "The C.I.E. colorimetric standards and their use," Transactions of the Optical Society **33**, 73–134 (1931).

[31] G.-H. Kim, B. Walker, H.-B. Kim, J. Y. Kim, E. H. Sargent, J. Park, and J. Y. Kim, "Inverted Colloidal Quantum Dot Solar Cells," Advanced Materials **26**, 3321–3327 (2014).

[32] D. Paz-Soldan, A. Lee, S. M. Thon, M. M. Adachi, H. Dong, P. Maraghechi, M. Yuan, A. J. Labelle, S. Hoogland, K. Liu, E. Kumacheva, and E. H. Sargent, "Jointly Tuned Plasmonic–Excitonic Photovoltaics Using Nanoshells," Nano Letters **13**, 1502–1508 (2013).

[33] A. J. Labelle, S. M. Thon, J. Y. Kim, X. Lan, D. Zhitomirsky, K. W. Kemp, and E. H. Sargent, "Conformal Fabrication of Colloidal Quantum Dot Solids for Optically Enhanced Photovoltaics," ACS Nano **9**, 5447–5453 (2015).

[34] J. J. Choi, W. N. Wenger, R. S. Hoffman, Y.-F. Lim, J. Luria, J. Jasieniak, J. A. Marohn, and T. Hanrath, "Solution-Processed Nanocrystal Quantum Dot Tandem Solar Cells," Advanced Materials **23**, 3144–3148 (2011).

[35] X. Wang, G. I. Koleilat, J. Tang, H. Liu, I. J. Kramer, R. Debnath, L. Brzozowski, D. A. R. Barkhouse, L. Levina, S. Hoogland, and E. H. Sargent, "Tandem colloidal quantum dot solar cells employing a graded recombination layer," Nature Photonics **5**, 480–484 (2011).

[36] R. W. Crisp, D. M. Kroupa, A. R. Marshall, E. M. Miller, J. Zhang, M. C. Beard, and J. M. Luther, "Metal Halide Solid-State Surface Treatment for High Efficiency PbS and PbSe QD Solar Cells," Scientific Reports **5**, 9945 (2015).

[37] M. Liu, O. Voznyy, R. Sabatini, F. P. García de Arquer, R. Munir, A. H. Balawi, X. Lan, F. Fan, G. Walters, A. R. Kirmani, S. Hoogland, F. Laquai, A. Amassian, and E. H. Sargent, "Hybrid organic–inorganic inks flatten the energy landscape in colloidal quantum dot solids," Nature Materials **16**, 258–263 (2017).

[38] B. Qiu, Y. Lin, E. S. Arinze, A. Chiu, L. Li, and S. M. Thon, "Photonic band engineering in absorbing media for spectrally selective optoelectronic films," Optics Express **26**, 26933–26945 (2018).

[39] S.-J. Lim, D.-S. Leem, K.-B. Park, K.-S. Kim, S. Sul, K. Na, G. H. Lee, C.-J. Heo, K.-H. Lee, X. Bulliard, R.-I. Satoh, T. Yagi, T. Ro, D. Im, J. Jung, M. Lee, T.-Y. Lee, M. G. Han, Y. W. Jin, and S. Lee, "Organic-on-silicon complementary metal–oxide–semiconductor colour image sensors," Scientific Reports **5**, 7708 (2015).

[40] J. J. Talghader, A. S. Gawarikar, and R. P. Shea, "Spectral selectivity in infrared thermal detection," Light: Science & Applications **1**, e24 (2012).

[41] H. Hara, N. Kishi, M. Noro, H. Iwaoka, and K. Suzuki, "Fabry-Perot filter, wavelength-selective infrared detector and infrared gas analyzer using the filter and detector," U.S. pat. 6590710B2 (Yokogawa Electric Corp, July 8, 2003).

[42] C. S. Goldenstein, R. M. Spearrin, J. B. Jeffries, and R. K. Hanson, "Infrared laser-absorption sensing for combustion gases," Progress in Energy and Combustion Science **60**, 132–176 (2017).

[43] A. D. Vos, "Detailed balance limit of the efficiency of tandem solar cells," Journal of Physics D: Applied Physics **13**, 839–846 (1980).

[44] F. Cao, K. McEnaney, G. Chen, and Z. Ren, "A review of cermet-based spectrally selective solar absorbers," Energy & Environmental Science **7**, 1615–1627 (2014).

[45] Peter Würfel, "Conversion of Thermal Radiation into Chemical Energy," in *Physics of Solar Cells* (John Wiley & Sons, Ltd, 2007), pp. 85–92.

[46] K. A. Bush, A. F. Palmstrom, Z. J. Yu, M. Boccard, R. Cheacharoen, J. P. Mailoa, D. P. McMeekin, R. L. Z. Hoye, C. D. Bailie, T. Leijtens, I. M. Peters, M. C. Minichetti, N. Rolston, R. Prasanna, S. Sofia, D. Harwood, W. Ma, F. Moghadam, H. J. Snaith, T. Buonassisi, Z. C. Holman, S. F. Bent, and M. D. McGehee, "23.6%-efficient monolithic perovskite/silicon tandem solar cells with improved stability," Nature Energy **2**, 17009 (2017).

[47] J. D. Joannopoulos, P. R. Villeneuve, and S. Fan, "Photonic crystals: putting a new twist on light," Nature **386**, 143–149 (1997).

[48] J. D. Joannopoulos, S. G. Johnson, J. N. Winn, and R. D. Meade, *Photonic Crystals: Molding the Flow of Light - Second Edition* (Princeton University Press, Oct. 30, 2011), 305 pp.

[49] S. Strauf, K. Hennessy, M. T. Rakher, Y.-S. Choi, A. Badolato, L. C. Andreani, E. L. Hu, P. M. Petroff, and D. Bouwmeester, "Self-Tuned Quantum Dot Gain in Photonic Crystal Lasers," Physical Review Letters **96**, 127404 (2006).

[50] H.-G. Park, S.-H. Kim, S.-H. Kwon, Y.-G. Ju, J.-K. Yang, J.-H. Baek, S.-B. Kim, and Y.-H. Lee, "Electrically Driven Single-Cell Photonic Crystal Laser," Science **305**, 1444–1447 (2004).

[51] P. Bermel, C. Luo, L. Zeng, L. C. Kimerling, and J. D. Joannopoulos, "Improving thin-film crystalline silicon solar cell efficiencies with photonic crystals," Optics Express **15**, 16986–17000 (2007).

[52] A. R. Parker and H. E. Townley, "Biomimetics of photonic nanostructures," Nature Nanotechnology **2**, 347–353 (2007).

[53] J. W. Galusha, L. R. Richey, J. S. Gardner, J. N. Cha, and M. H. Bartl, "Discovery of a diamond-based photonic crystal structure in beetle scales," Physical Review E **77**, 050904 (2008).

[54] Z. Wang, C. T. Chan, W. Zhang, N. Ming, and P. Sheng, "Three-dimensional self-assembly of metal nanoparticles: Possible photonic crystal with a complete gap below the plasma frequency," Physical Review B **64**, 113108 (2001).

[55] K. Xingze Wang, Z. Yu, V. Liu, A. Raman, Y. Cui, and S. Fan, “Light trapping in photonic crystals,” Energy & Environmental Science **7**, 2725–2738 (2014).

[56] A. Chutinan, N. P. Kherani, and S. Zukotynski, “High-efficiency photonic crystal solar cell architecture,” Optics Express **17**, 8871–8878 (2009).

[57] R. B. Withrow and L. Price, “Filters for the Isolation of Narrow Regions in the Visible and Near-Visible Spectrum 1,” Plant Physiology **28**, 105–114 (1953).

[58] H. Wang and L. Wang, “Perfect selective metamaterial solar absorbers,” Optics Express **21**, A1078–A1093 (2013).

[59] K. F. Renk and L. Genzel, “Interference Filters and Fabry-Perot Interferometers for the Far Infrared,” Applied Optics **1**, 643–648 (1962).

[60] L. Li, “Formulation and comparison of two recursive matrix algorithms for modeling layered diffraction gratings,” Journal of the Optical Society of America A **13**, 1024 (1996).

[61] L. Li, “Use of Fourier series in the analysis of discontinuous periodic structures,” Journal of the Optical Society of America A **13**, 1870 (1996).

[62] L. Li, “New formulation of the Fourier modal method for crossed surface-relief gratings,” Journal of the Optical Society of America A **14**, 2758 (1997).

[63] R. d. L. Kronig, “On the Theory of Dispersion of X-Rays,” JOSA **12**, 547–557 (1926).

[64] R. d. L. Kronig and H. Kramers, “La diffusion de la lumiere par les atomes,” Atti Congr. Intern. Fisici **2**, 545–557 (1927).

[65] J. S. Toll, “Causality and the Dispersion Relation: Logical Foundations,” Physical Review **104**, 1760–1770 (1956).

[66] E. D. Palik, “- Gallium Arsenide (GaAs),” in *Handbook of Optical Constants of Solids*, edited by E. D. Palik (Academic Press, Burlington, Jan. 1, 1997), pp. 429–443.

[67] Haus H. A., *Waves And Fields In Optoelectronics* (Prentice Hall, Englewood Cliffs, N.J., 1984).

[68] S. Fan, W. Suh, and J. D. Joannopoulos, "Temporal coupled-mode theory for the Fano resonance in optical resonators," Journal of the Optical Society of America A **20**, 569 (2003).

[69] Wonjoo Suh, Zheng Wang, and Shanhui Fan, "Temporal coupled-mode theory and the presence of non-orthogonal modes in lossless multimode cavities," IEEE Journal of Quantum Electronics **40**, 1511–1518 (2004).

[70] S. Fan and J. D. Joannopoulos, "Analysis of guided resonances in photonic crystal slabs," Physical Review B **65**, `10.1103/PhysRevB.65.235112` (2002).

[71] C. L. Cheung, R. J. Nikolić, C. E. Reinhardt, and T. F. Wang, "Fabrication of nanopillars by nanosphere lithography," Nanotechnology **17**, 1339 (2006).

[72] M. M. Adachi, A. J. Labelle, S. M. Thon, X. Lan, S. Hoogland, and E. H. Sargent, "Broadband solar absorption enhancement via periodic nanostructuring of electrodes," Scientific Reports **3**, 2928 (2013).

[73] M. A. Hines and G. D. Scholes, "Colloidal PbS Nanocrystals with Size-Tunable Near-Infrared Emission: Observation of Post-Synthesis Self-Narrowing of the Particle Size Distribution," Advanced Materials **15**, 1844–1849 (2003).

[74] A. G. Pattantyus-Abraham, I. J. Kramer, A. R. Barkhouse, X. Wang, G. Konstantatos, R. Debnath, L. Levina, I. Raabe, M. K. Nazeeruddin, M. Grätzel, and E. H. Sargent, "Depleted-Heterojunction Colloidal Quantum Dot Solar Cells," ACS Nano **4**, 3374–3380 (2010).

Chapter 4

Probing Local Properties and Defects in Thin Film Optoelectronics via Spatially Resolved Multi-Modal Optoelectronic Spectroscopy

This chapter is partially adapted from Ref[1]. Reprinted with permission from Advanced Materials 32, no. 11 (2020): 1906602, ”Local Defects in Colloidal Quantum Dot Thin Films Measured via Spatially Resolved Multi-Modal Optoelectronic Spectroscopy”, by Yida Lin, Tina Gao, Xiaoyun Pan, Maria Kamenetska and Susanna M. Thon, copyright © 2020.

4.1 Motivation and Introduction to the Methodology

The morphology, chemical composition, and electronic uniformity of thin-film solution-processed optoelectronics are believed to greatly affect device performance. The concern has been accompanying the rapid development and prosperity of the area. In recent years,considerable attention has been devoted to solution-processed thin-film solar cells based on perovskites [2–4] , colloidal quantum dots (CQDs)[5–7], and organic materials[8–10], due to their low fabrication and materials costs, lightweight and flexible nature, and potential for new applications. As a result, these technologies have experienced improvements in device performance, parameter control, cost-effective production methods, and stability, either via physical and chemical engineering down to the molecular and atomic scales, or via development of new growth and fabrication methods.

Usually, the efficacy of a new growth or fabrication method is tested and verified through a series of measurement performed on devices that are assumed to be uniform in all relevant physical parameters (chemical composition, electronic properties, layer thicknesses, etc.), and can be categorized by a defined set of parameters under investigation such as transport layer thickness, deposition solution concentration, annealing temperature, and so on. The optoelectronic properties measured are therefore regarded as a statistical average of similar portions of the active device area. This procedure is sufficient if the device under investigation has a narrow distribution for most of the critical physical properties which can, in theory, be guaranteed by careful control during the full processes of preparation, synthesis and fabrication and optional encapsulation. However, this is hard to achieve due to the nature of solution-processing techniques and the materials. In reality, micrometer-scale defects with dimensions greater than the entire thickness of the structure, or lateral defects appearing as “streaks” or “ripples” can often be observed by eye, with areas that may comprise only a small portion of, but extend across the entire, device active area **Figure 4-1c**. Compositional variation can also be induced by uneven dispersion of the material solutions during deposition, which may only manifest as color variations in the final film though, indicate more profound underlying structural and electronic non-uniformities.

These various sources of inhomogeneity are associated with important but unanswered questions, including: what is the magnitude of the direct negative effects, if any, of inhomogeneity on device performance metrics, and are the defective areas ony respon-

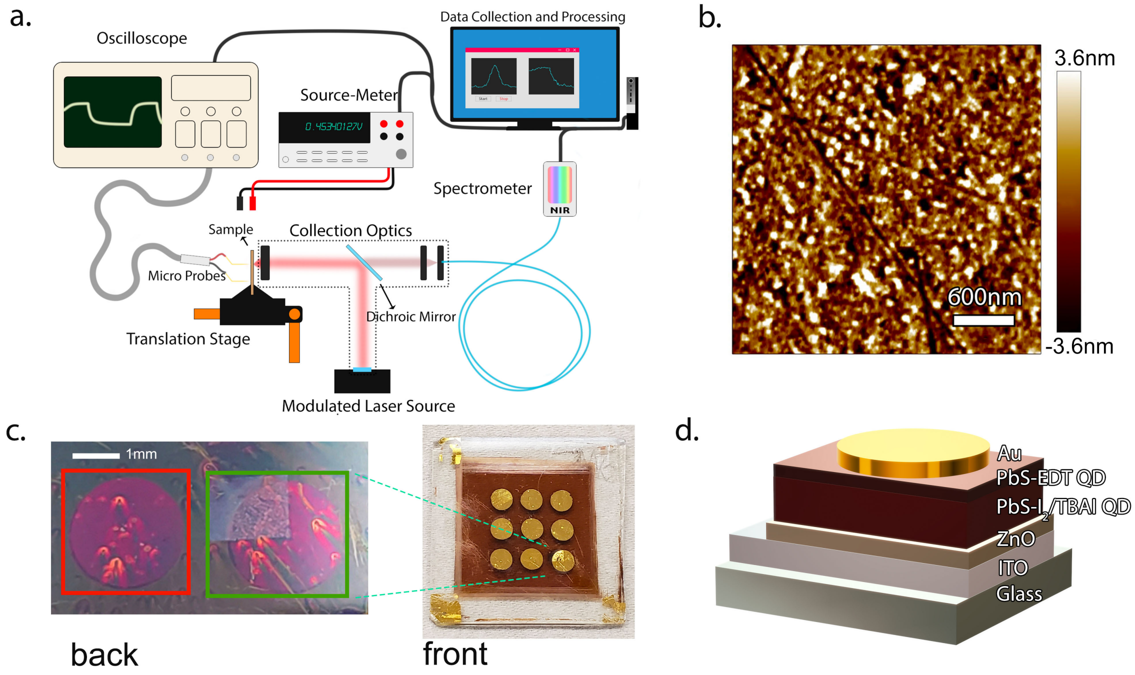

Figure 4-1. a. Diagram of the multi-modal measurement and data collection system. **b.** AFM image of a 3 µm × 3 µm area of the surface of one of the CQD photovoltaic devices measured, showing a root-mean-square average local roughness of 2.6 nm. **c.** Left: Photograph of two of the device active areas reported here, defined by circular top contacts of 2.4 mm in diameter, taken through the glass substrate ("back"). The device indicated by the orange rectangle is the subject of **Figure** 4-2, **Figure** 4-4 and **Figure** 4-8 (Device 1), and the device indicated by the green rectangle is the subject of **Figure** 4-10 (Device 2). Right: Photograph of the full substrate containing nine devices taken from the gold side ("front"). **d.** Diagram of the full device architecture: ITO is the indium tin oxide transparent contact, ZnO is the zinc oxide electron transport layer, PbS-I_2/TBAI QD is the PbI_2 or TBAI-ligated absorbing PbS quantum dot layer, PbS-EDT QD is the ethanedithiol-ligated PbS quantum dot hole transport layer, and Au is the gold top contact.

sible for the performance loss in their own regions or there exist interactions between them and the "normal" or defect-free film regions, causing further decreases in performance? Relatedly, although it is logical to expect a better performance from a sample that is visually uniform than from one with visible defects and inhomogeneity, experimental results suggest that this may not always be the case. The question of if intrinsic nano and micro-scale physical and/or electronic variation in the device, which are present even under ideal fabrication environments, such as the much-studied effects of charge carrier traps [11–14] are more important than the negative effects from larger scale faulty areas caused by accidental damage and defects introduced during the fabrication or even testing and storage processes remains unaddressed.

These questions have been partly examined by scanning probe microscopy (SPM) measurements, [15–22] which can be used to visualize nearly molecular-scale morphological inhomogeneities in the active film and compared with conductivity, photocurrent, and work function mappings of the film with the same high resolution. For example, conductive-atomic force microscopy(AFM) has been very successful in revealing the strong photocurrent variation associated with polycrystalline domains and grain boundaries[16–18] and AFM-IR has been used to measure spatial absorption inhomogeneity caused by compositional variations that can be eliminated by annealing[23, 24]. Nonetheless, most SPM methods involve fundamental trade-offs between total field of view (FOV) and spatial resolution, and consequently, the mapping is usually restricted to less than $10\,\mu\text{m} \times 10\,\mu\text{m}$ in area. Even if multiple measurements are stitched together, profiling a small device area of cm2 in extent is extremely impractical. Moreover, the visible defects accidentally introduced during fabrication such as dust, agglomerates precipitated during solution-processing, and scratches from transfer and testing, usually have dimensions of up to 0.1 mm. These areas are too large to sample using SPM measurements, and, consequently, their properties and effects cannot be probed. In addition, we found that the optoelectronic behaviors of devices can have considerable spatial variations on scales larger than 0.1 mm, even if their topological profiles, as measured by SPM, are “smooth” across multiple-micrometer-scale regions, meaning these variations cannot be studied using submicrometer-scale SPM.

There are a few later reports of large-area ($\approx$ cm^2) characterization methods using infrared camera imaging that extract thin-film optoelectronic device parameters such as quasi-Fermi level splitting, carrier mobilities, and carrier lifetimes, based on spectrally resolved photoluminescence (PL)[20] or frequency- dependent photoresponse obtained from homodyne and heterodyne lock-in carrierographies [25, 26]. However, the practical spatial resolution of such methods is limited by the camera capabilities, and, compared with scanning optical microscopy, diffraction-limit resolution is hard to achieve due to the nature of large-FOV optics. Moreover, such methods are highly reliant on the specific carrier physics model to describe the system and mathematical or numerical treatment to extract a specific set of large numbers of parameters, which can result in large uncertainties in the results should the assumptions be changed, and a lack of straightforward physical interpretations of most intermediate data before the final results, which can be otherwise very useful to intuitively predict and assess the qualitative behaviors of the devices along with the progression of the measurements.

A high-resolution 2D method for mapping optoelectronic properties that can bridge the gap between submicrometer-scale SPM and millimeter-to-centimeter-scale practical device areas is therefore a critical need for answering questions about the effects of macro-scale defects on device performance. This method should provide straightforward and self-contained measurements that can both be interpreted both separately and combined to derive more complicated parameters and, ideally, require minimal costly advanced instrumentation. As a solution, we developed a system in which the spatial resolution is configurable, with the fundamental limit set by the focusing of the excitation optics and the step size of a scanning stage down to <1 μm, rather than the fixed radius of an SPM tip or the resolution of a camera. Our system can therefore generate mappings of either partial or full devices over large areas by scanning the excitation over the active area and simultaneously measuring multiple optoelectronic properties of interest. Here, we use this system to measure data collected from lead sulfide (PbS) CQD solar cells and use it to analyze the effects of localized macro-scale defects on device properties.

Our system consists almost entirely of off-the-shelf components already present in most optoelectronics labs, as opposed to costly or custom instrumentation. We use a focused pulsed laser as the excitation source to probe an optoelectronic device mounted on x–y–z translation stages driven by DC motors with sub-micrometer resolution and centimeter travel ranges. A diagram of the experiment setup is shown in **Figure 4-1a**. A laser beam is collimated and focused onto the sample plane by an infinite-conjugate aspheric lens with an effective focal length of 8.0 mm. The PL signal is then collected by the same objective lens, collimated, directed back through a dichroic mirror only allowing the passage of infrared wavelengths, and coupled into a multi-mode optical fiber to be analyzed by a fiber-coupled near infrared spectrometer (Ocean Optics NIRQuest512).

For collection of photocurrent and photovoltage responses, the sample is electrically connected by microprobes to an oscilloscope for transient measurements. A source-meter (Keithley 2400) provides biases, steady-state current–voltage measurements, and shunt resistance, if needed. The laser signal is modulated using a function generator with a square wave output of 100–10 000 Hz, and duty cycles 0.05–0.2. The modulation frequency is chosen so that the photovoltage and photocurrent transients responses have time to recover in between excitations, while allowing the fastest possible sampling rate. The translation stage is programmed to move along a 2D grid with preset step sizes and dwells at each step, so that PL and electrical measurements can be integrated and collected. The resolution and range of the system can be varied by configuring the step sizes and travels of translation stages, or adapting stages of even higher capabilities, making our system adaptable to a wide range of length scales.

The system is capable of synchronous and aligned measurement of PL spectra, transient photocurrent and photovoltage responses, full current–voltage curves, and other optical and electronic characteristics that can be probed through optical and/or electronic excitation. The focused nature of the laser beam sets the excitation area in the sample to smaller than a few micrometers. Photogenerated carriers in PbS CQD solar cells migrate primarily in the vertical direction, due to the sub-micrometer diffusion lengths[14, 27] electrical response is also collected from within the resolution range set by the excitation area. The confocal nature of the collection mechanism further improves the resolution of the PL mapping.

Once the 2D mappings of the device area are obtained, other critical parameters can be extracted from fits to the data such as PL peak intensity and width, photocurrent and photovoltage magnitudes and decay times, and carrier mobilities. Combined with thickness profiles, we obtained clear images of morphological defect regions and their relationships with optoelectronic properties, as well as the variation of optoelectronic properties within non-defect regions. By simultaneously measuring multiple properties, we were able to explore and elucidate the correlations and interactions between such properties, and thus provide insights into the fundamental carrier dynamics that occur in operating devices. Additionally, to understand the extent to which a certain defective region affects the surroundings and the overall device performance, we artificially introduced a continuous large-scale faulty area of a given size and shape by subjecting the CQD film to high intensity laser illumination, resulting in probable CQD ligand loss and fusion that ensure the region dysfunctional . We then quantified the effects on device metrics from both artificial and “natural” defects and compared their properties.

The step size in our CQD solar cell experiments was set to 10–50 µm based on the required resolution and scanning time or desired area coverage, and the number of grid points was set to 10^3–10^4, corresponding to complete image sizes as large as 5×5 mm, covering a substantial fraction of a single solar cell device (typical area of $\approx$3–5 mm^2). Higher resolution and image sizes are also achievable as long as sufficient collection time is allowed. The single-point exposure and collection times for different types of measurements are summarized in Table S1 (Supporting Information). For the PL measurements, we collected a spectrum covering 1100 to 1700 nm in wavelength for each point, which was then fit to a dual-Gaussian distribution to account for emission from both the core and secondary states[28, 29].

Measurement type	PL only	PL+PC/PV (amplitude only)	PL+TPC (transients, each bias)	PL+TPV (transients, each bias)	Additional Stage Movement
Typical Exposure Time	50-120ms	50-200ms	200-600ms	300-1000ms	50-200ms

Table 4.1. Exposure/Sampling time required for different types of measurements (PL: photoluminescence, PC: photocurrent, PV: photovoltage, TPC: transient photocurrent, TPV: transient photovoltage). The total dwell time at each point in the scan is the sum of the exposure time for the measurement type (yellow boxes) plus the stage movement time (blue box).The total time for a complete measurement is approximately the number of points in the scan times the dwell time.

As a result, the data containing PL peak intensity, peak width, and integrated peak intensity are generated for the core emission and secondary emission states at each film location. The photocurrent transient signals are captured by applying a zero or reverse bias to the device, creating currents which generate voltage signals across the shunt resistor that are then processed by the oscilloscope. The data consist of time curves, from which the magnitudes and the time constants of the exponential decays can be extracted from fits. To collect photovoltage signals, we set the open-circuit voltage (V_{OC}) of the device by applying a constant laser excitation background and a modulated pulsed component that creates an $\approx$100 mV additional signal. The photovoltage data are collected by connecting the device to the oscilloscope in an open-circuit configuration. The data are then processed to produce 2D maps of both background photovoltage (V) and pulsed photovoltage (ΔV) magnitudes, as well as the pulsed photovoltage decay time constant.

We illustrate our spatial-resolved multi-modal measurement method on CQD solar cells employing the current standard device architectures in the field[5, 6]. Briefly, the structure consists of a transparent indium tin oxide (ITO) electrode coated on a glass substrate, a spin-cast ZnO electron transport layer, a solution-phase exchanged PbI_2 or solid-state exchanged tetrabutylammonium iodide (TBAI) treated PbS CQD active layer, an ethanedithiol (EDT) treated PbS CQD hole transport layer, and an evaporated Au electrode. A device photograph taken through the transparent glass is shown in **Figure 4-1c**, and a diagram of the device structure is shown in **Figure 4-1d**. Measurements of the two devices indicated by colored rectangles in the photograph are described in the following sections. All measurements were conducted in air, due to the excellent air stability demonstrated by the devices of interest, although a nitrogen-flow environment could be incorporated into the system, if necessary.

4.2 Experimental Results and Discussion

Figure 4-2shows the results of PL mapping of the device in the orange square of **Figure 4-1c** (Device 1, TBAI-PbS). This particular device was employed because it has a surface profile with more topological variations than a typical device of the same type and comparable performance, in order to demonstrate the effects on device behaviors of a variety of defect types. The color scale of the PL map in **Figure 4-2a** denotes the peak intensity of the core emission state, determined from the Gaussian fitting of the spectrum of each spatial point, as described in the previous section. Two example PL spectra collected at two specific locations in the sampled region are shown in **Figure 4-2b**. The location with lower PL intensity has a dramatically redshifted and slightly broadened PL spectrum compared with other majority typical locations in the map, which is posited to result from CQD fusion due to excessive heating or ablation from the focused laser beam. Defects of this type can be identified by examining in the map of the secondary PL intensity and are associated with higher-intensity longer wavelength contribution in the dual-Gaussian fitting, as shown in **Figure 4-2b**.

In order to account for differences in PL intensity due purely to differences in film thickness, we measured the height of the same device area using 3D scanning confocal microscopy. The original height map contains several spikes of much greater height than

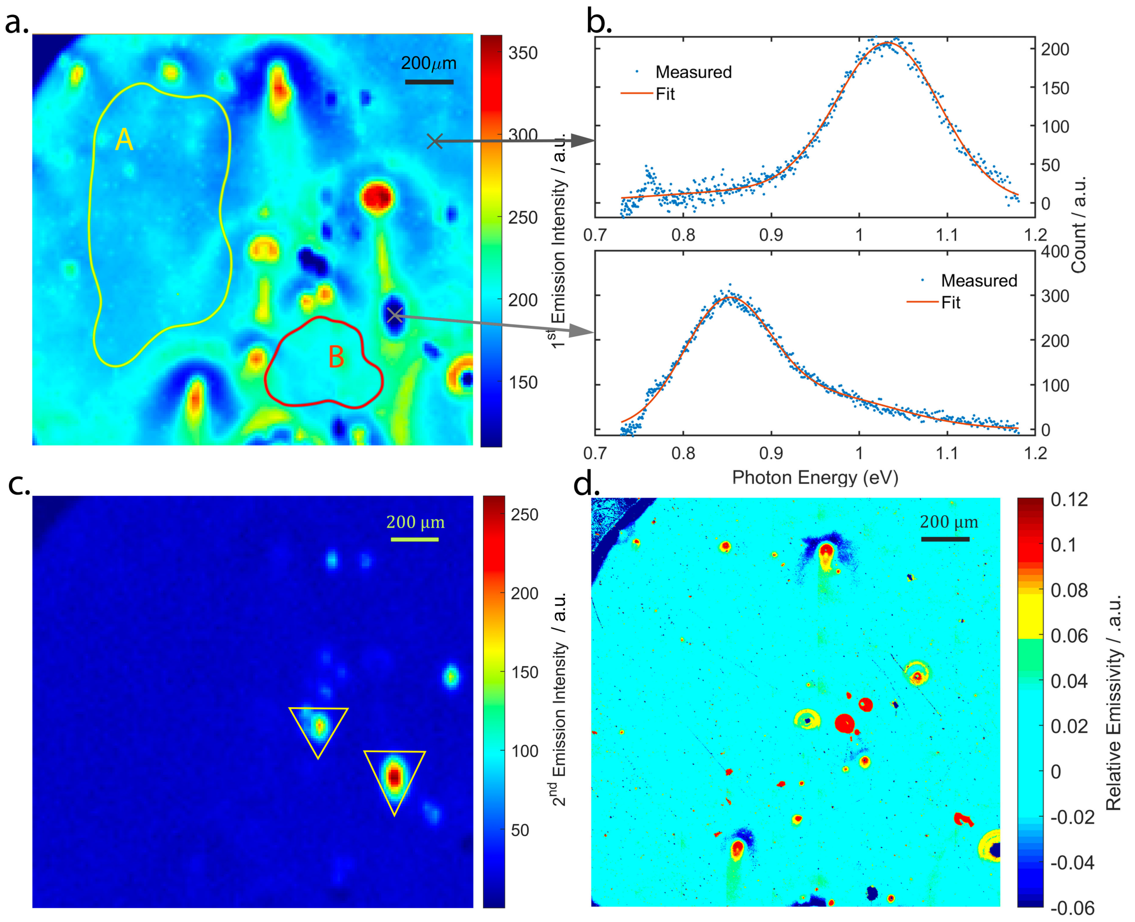

Figure 4-2. **a.** Peak intensity map of the PL core state emission. The properties of regions A and B are described in the text. **b.** PL spectra from two example locations marked with crosses in **a.**. **c.** Peak intensity map of the secondary PL peak emission. Defects caused by intentional laser heating appear as spots with warmer colors and are indicated by triangles. **d.** Relative emissivity map of the same area as in **a.**.

the majority of the sampled area, potentially associated with CQD aggregates deposited during the film fabrication process, which limited the visual dynamic range of the height map. We therefore chose to compare the PL intensity map with the relative emissivity derived from height map. PL intensity is a function of the emissivity and the PL quantum yield (PLQY) of the thin film. If we first treat the PLQY and absorption coefficient as effective averages over the entire sampled area, we can obtain the relative emissivity mapping of the CQD film from the height map, which is given by $-C\exp(-\alpha h)$, where α is the average absorption coefficient of the PbS CQD film at the excitation wavelength,

h is the sample height, and C is a constant that accounts for the offset of the thickness from zero and other factors. The differences in the relative emissivity map are therefore a measure of the contributions to the PL that originate only from thickness variation. The result is shown in **Figure 4-2d**, and it suggests a strong correlation between emissivity and PL core peak intensity, implying that most of the strong variation in the PL is caused by the variations in the thickness of the CQD film. On the other hand, subtle deviations from this correlation can reveal different properties of the underlying areas. For example, the highest amplitude regions in the emissivity mapping (saturated in color) have the strongest PL intensities, but their contrast with the surrounding areas is not as large in the PL map as in the emissivity map. This suggests that these anomalous thick spots have lower PLQY, possibly due to agglomeration and increased CQD size variation.

Another region with lower PL intensity than expected from its emissivity is circled and labeled Region “A” in **Figure 4-2a**. This region is smooth on a local scale, with roughness on the order of 2.6 nm rms, as measured via AFM for a small typical device area (**Figure 4-1b**). The lower PLQY here is potentially associated with efficient exciton dissociation and higher carrier mobilities, as opposed to defects resulting from CQD fusion, for which additional evidence can be found in the photocurrent and photovoltage maps shown in **Figure 4-2**. The region labeled “B” located at the bottom right corner of **Figure 4-2a** has higher PL intensity than expected from its emissivity, which could potentially result from a higher absorption rate and anomalous nonradiative recombination properties, as will be discussed later.

Another important factor that could result in PL intensities that deviate from the emissivity estimates is the effect of multi- layer thin-film interference (Fabry–Peṙot) effects. Our device structure consists of a stack of thin films (**Figure 4-1d**) with thicknesses on the order of the optical wavelengths of interest and long-scale thickness variations of ≈10–20 nm, as commonly measured by cross-sectional scanning electron microscopy. We calculated the effect that thickness variations of this scale should have on the active layer

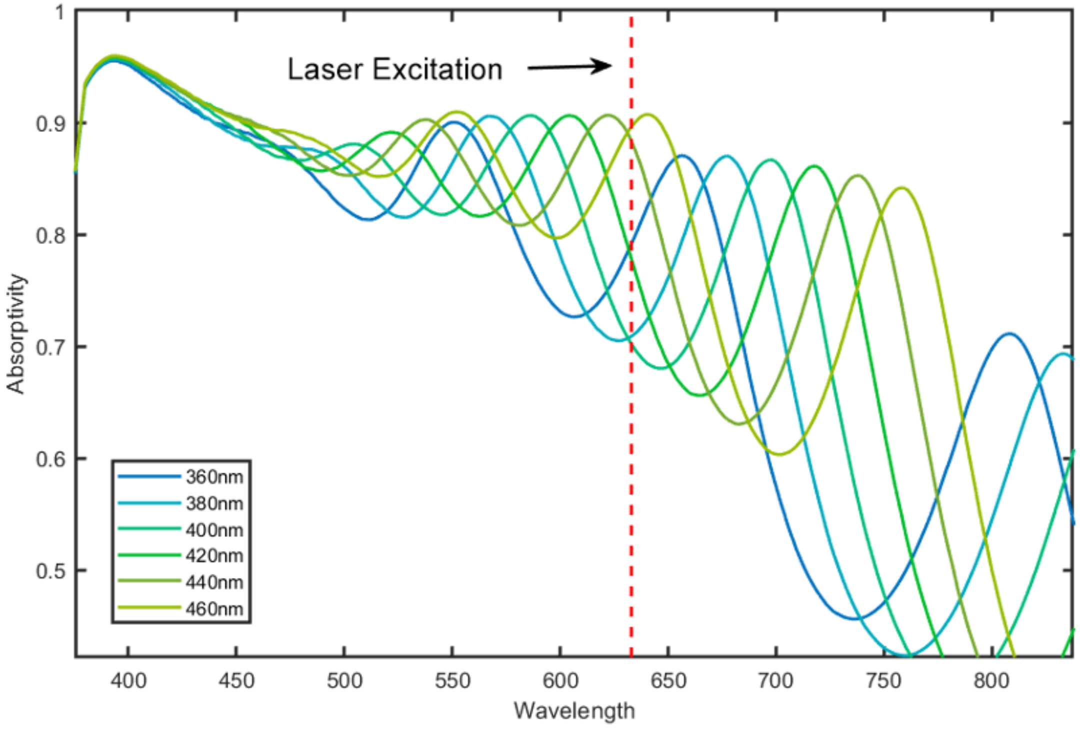

Figure 4-3. Absorptivity of the active layer calculated via the Transfer Matrix Method (TMM) for six different layer thicknesses (PbI_2 +PbS-EDT). The dashed line indicates the laser wavelength used in our experiments. Optical materials constants used in the calculations are taken from References [30, 31].

absorption using the transfer matrix method[30, 31] and show the results in **Figure** 4-3. We found that the wavelength-dependent absorptivity of the active layer can vary by up to 20% at the laser excitation wavelengths (450–650 nm) used in our experiments. Interference effects can therefore be responsible for similar-scale variations in photoinduced responses such as photocurrents and photovoltages.

Photocurrent and photovoltage measurement results from the same device are summarized in **Figure** 4-4. The results proved to be stable under repetitive measurements over hours-long intervals, and the exposure or integration time has little effects but on the signal-to-noise ratio (**Figure** 4-5). Spatial alignment between the maps is guaranteed by the simultaneous collection of all measurements at each point. Photocurrent and photovoltage are excited using square wave laser modulation of 2–10 kHz and 0.5–5 kHz, respectively. **Figure** 4-4**a** shows a map of the amplitude of the transient photocurrent at short-circuit conditions, and **Figure** 4-4**b** shows a map of the time constant extracted from the same measurement. The spatial variation in the photocurrent amplitude can be larger than 30% of its mean value, even within the regions that are relatively flat and smooth as measured by their PL intensity and emissivity mapping. This suggests that factors other than the presence of macroscopic film defects, such as energy band alignment, recombination center density, and thin-film interference effects, can vary widely across the device and affect current extraction capabilities, even in a film that appears morphologically uniform. **Figure** 4-4**d** shows a histogram of the photocurrent amplitudes from the entire scanned area, indicating that device current could theoretically be improved by at least 10% if the entire device had the average intrinsic film quality of the highest photocurrent regions (Regions A and B in **Figure** 4-4**a**). This improvement could be even greater if the local variance in the photocurrent was reduced.

An example photocurrent trace for a specific point is shown in **Figure** 4-4**c**. The time signal can be well fit to a single exponential function to yield a time constant, which is closely related to the transit time,τ, of the photogenerated carriers across the entire device. We verified that the RC time constant (product of the resistance and capacitance of the circuit) [32] associated with the parasitic capacitance of the devices as well as the external resistance, being less than 0.1 µs, is much smaller than the time scale being investigated 2–200 µs, so it should not interfere with the transient measurements. We also tested the effect of a constant background (DC) white light bias on the device transient photocurrent behaviors shown in **Figure** 4-6. The spatial distributions of the current component from excitation by only the laser, and by both the laser and DC white light bias are similar. However, the current component from the laser excitation in the presence of the DC white light bias is weaker overall than in the case without the bias. This indicates the presence of a potential photocurrent saturation effect under higher illumination intensities. Comparison of the two maps can also enable the identification of

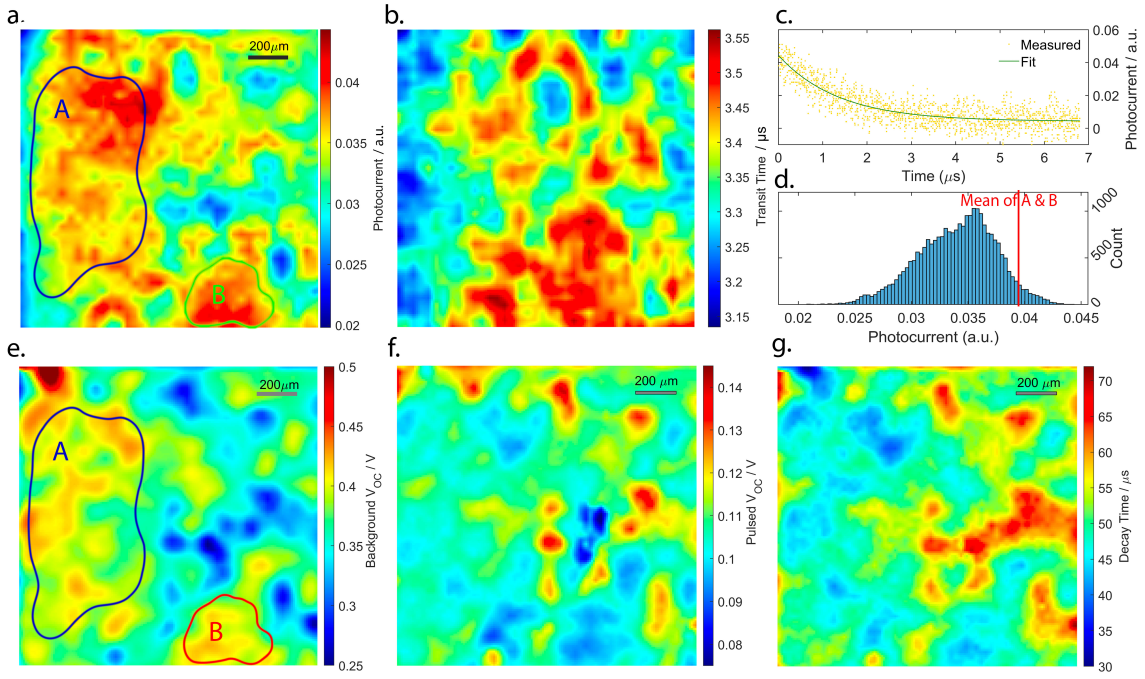

Figure 4-4. Simultaneous photocurrent and photovoltage maps of a CQD solar cell device (Device 1). Regions A and B indicate the same locations as in **Figure** 4-2. **a.** Photocurrent amplitude map. **b.** Electronic transit time map derived from the time decay of the photocurrent. **c.** Representative photocurrent time trace from a single measurement point fit to a single exponential function. **d.** Histogram of photocurrent amplitudes of the entire area shown in **a.**. The mean photocurrent of Areas A and B is also indicated. **e.** Background photovoltage map. **f.** Pulsed photovoltage map (ΔV). **g.** Pulsed photovoltage decay time, extracted from an exponential fit.

regions that outperform (e.g., area B) or underperform (e.g., area A) in terms of current generation intensities compared to the surrounding areas.

By extracting transit times at different reverse biases, we can calculate the carrier mobility, μ, based on the relation: $\frac{d^2}{\tau} = \mu(V - V_{\mathrm{bi}})$, where d is the device thickness, V is the applied bias, and V_{bi} is the built-in potential. The transit time map in **Figure** 4-4**b** is much noisier than the photocurrent amplitude map, due to the uncertainty in the fits of the time traces. Nonetheless, differences across the sample can still be discerned; for example, a vertical strip on the left side of the image has faster transit times than the sample average. This area also displays high average photocurrent, labeled in **Figure** 4-4**a**, im-

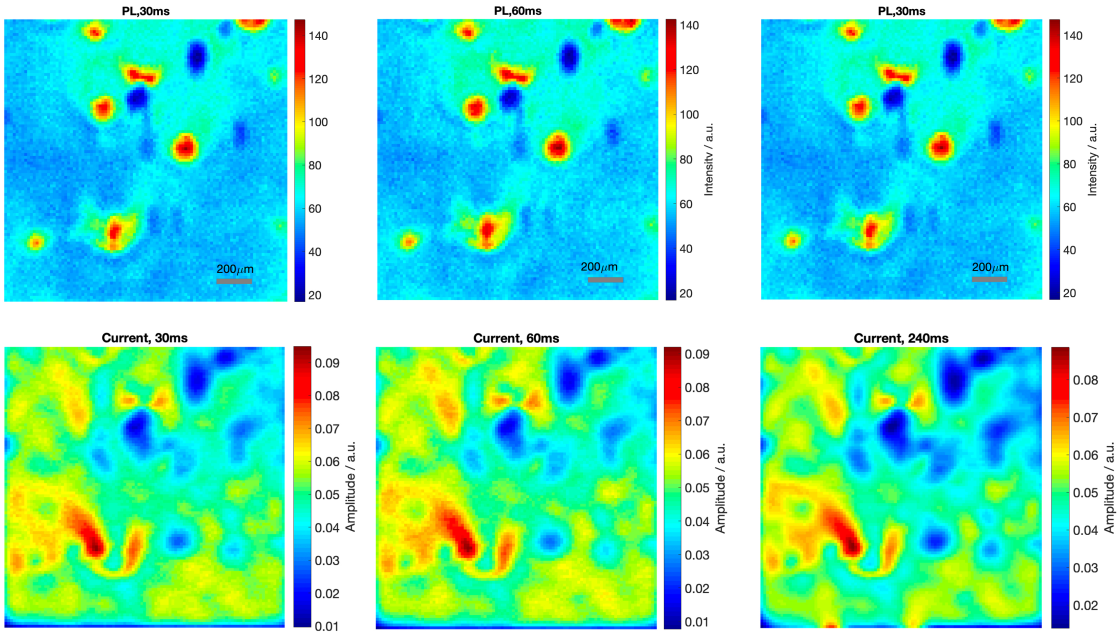

Figure 4-5. Device stability tests. Top: Photoluminescence maps. Bottom: Photocurrent amplitude maps. The same device was measured three times with varying exposure (integration) times from 30 ms (left) to 60 ms (middle) to 240 ms (right). The measurements were conducted over a period of approximately 10 hours and show only minimal signal-to-noise ratio variations over this extended period.

plying that slightly faster (≈ 10%) carrier extraction may increase photocarrier collection at a even higher rate (≈20 % to 30 %). We also probed spatial variations in photocurrent collection capabilities by using the assumption of complete carrier extraction at sufficient reverse bias to produce internal quantum efficiency (IQE) maps at short circuit(**Figure 4-9e**).

Meanwhile, the measured photovoltage amplitudes are divided into two different components, a "background" voltage generated by a constant DC laser bias and a "pulsed" component due to the addition of a modulated laser pulse on top of the background bias. Maps of the two components are shown in **Figure 4-4e,f**, respectively. **Figure 4-4f** shows the decay time constant of the pulsed photovoltage, extracted in the same manner as the transit time in the photocurrent measurements. Regions with higher photovoltage in the maps coincide with regions of higher photocurrent as would be expected from the simple

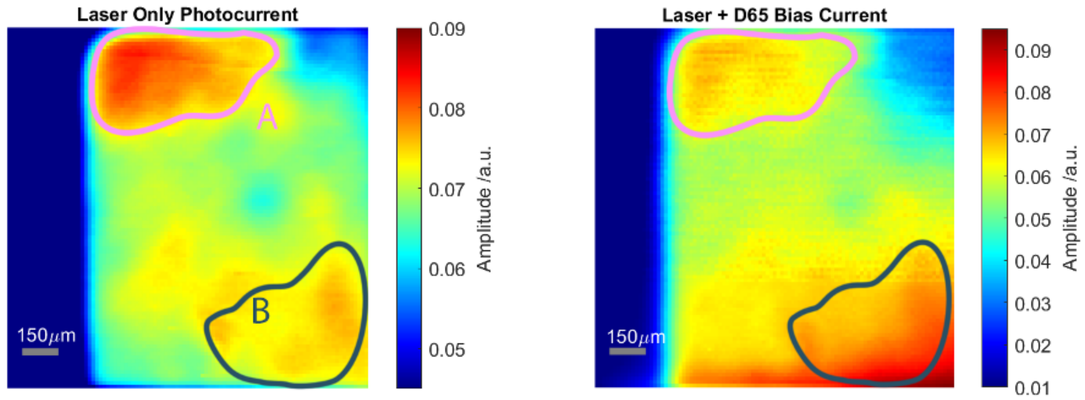

Figure 4-6. Photocurrent maps excited with only modulated laser (left) and with the addition of a constant 6500 K white light bias from an LED source (right). The white light illuminance was approximately 0.8 suns. The photocurrent from only the white LED source without any laser modulation, as a background, is subtracted from the data of the right plot. The spatial distribution of current is similar in the two cases.

relationship: $V_{\mathrm{OC}} = kT \ln \frac{J_{\mathrm{Gen}}}{JRec(0V)}$, where J_{Gen} is the photogenerated current density and $J_{\mathrm{Rec}}(0V)$ is the recombination current density at zero bias. This observation does not contradict the well-accepted trade- off between short-circuit current density J_{SC} and V_{OC} for CQD solar cells when the thickness of the active layer is increased beyond the optimum, in which case J_{SC} is improved due to increased total absorption, which, however, also induces higher recombination current that can outpace increases in the current. In the case highlighted in **Figure 4-4a**, the high J_{SC} of the two example regions is likely due to better carrier extraction associated with lower average J_{Rec} or higher average J_{Gen} caused by higher absorption rate instead of thicker material, all of which can benefit both J_{SC} and V_{OC}. Similarly, the fact that the effect is not due to large average film thickness, can be confirmed by the PL and height maps.

Moreover, comparisons between the background and pulsed photovoltage maps reveal an interesting effect: the regions with high background photovoltage are almost always associated with lower pulsed photovoltage. This trend is not affected by the magnitude of the constant background laser excitation (or equivalently the overall V_{OC} magnitude) for a given device. Here we propose some possible origins of this V_{OC} saturation effect at higher excitation levels. Consider the simple case, where the recombination current J_{Rec} and pen-circuit voltage V_{OC} are determined by:

$$J_{\text{Rec}} = J_{\text{Rec}}(0\text{V}) \exp{(\frac{qV}{nkT})} \tag{4.1}$$

$$V_{\text{OC}} = \frac{nkT}{q} \frac{J_{\text{Gen}}}{J_{\text{Rec}}(0\text{V})} \tag{4.2}$$

where the carrier generation current J_{Gen} is only dependent on the absorption of the material and the thickness of the active layer and is strictly proportional to the incident photon flux. Suppose that during the pulsed excitation, the total incident photon flux is $1 + c$ times that during the background, then we have:

$$\Delta V_{\text{OC}} = \frac{nkT}{q} \left(\ln \frac{(1+c)J_{\text{Gen}}}{J_{\text{Rec}}(0V)} - \ln \frac{J_{\text{Gen}}}{J_{\text{Rec}}(0V)} \right) \tag{4.3}$$

and ΔV_{OC} should be independent of J_{Gen}, J_{Rec}, or V_{OC} themselves. The fact that our observations diverge from this behavior implies that the carrier recombination must be increasing faster in the regions with higher V_{OC}, or faster across the device overall, than predicted by a single exponential relationship at higher applied biases relative to the case at lower biases. Several hypotheses for the origins of this behavior include (1) regions with differing values of V_{OC} have different dominant recombination types, which can be quantified as different ideality factors (n) in the expression:

$$J_{\text{Rec}} = J_{\text{Rec}}(0V) \exp \frac{qV}{nkT} \tag{4.4}$$

so that although lower values of $J_{\text{Rec}}(0V)$ in certain regions lead to higher V_{OC} in those regions, the increment, ΔV_{OC}, with additional J_{Gen} is actually smaller when radiative recombination processes are dominant ($n = 1$) than when Shockley–Read–Hall recombination processes are dominant ($n = 2$). This is a common characteristic of higher quality optoelectronic films. Another possibility is that (2) given the larger quasi-Fermi-level splitting in all areas with higher J_{Gen} , the occurrence of multi-exciton recombination events with rates that depend on higher powers of the product of carrier concentrations—such as Auger recombination and bi-exciton radiative recombination—is greatly increased, resulting in smaller ΔV_{OC} needed to compensate the additional J_{Gen}. Moreover, there could be (3) an energy-dependent trap state density distribution that leads to a varying number of activated trap states available for recombination under different quasi-Fermi-level splittings. This effect could cause a faster or slower growth in $J_{\text{Rec}}(0V)$, which could either aggravate the V_{OC} saturation effect in addition to (1) and (2), or alleviate it, depending on the exact trap state distribution and V_{OC} regime.

We note that the ΔV_{OC} generated in region B is lower than that in region A. Given that both areas have comparable photocurrents and background photovoltages, one possible explanation is that region B has higher J_{Gen} due to a higher absorption rate, and therefore higher $J_{\text{Rec}}(0V)$ that limits J_{SC} as $J_{\text{SC}} = J_{\text{SC}} - J_{\text{Rec}}(0V)$. In this case, region B has higher carrier concentration and a higher recombination rate than region A at a certain V_{OC}, which causes it to approach V_{OC} saturation faster and results in lower ΔV_{OC}. Moreover, the $J_{\text{Rec}}(0V)$ can be considered as a measure of the magnitude of the recombination rate associated with carrier accumulation caused by strong illumination and can be estimated by taking the derivative of the photocurrent with respect to voltage near zero bias, which is the shunt conductance S_{shunt}. This is because, according to 4.4:

$$S_{\text{shunt}} = \frac{dJ}{dV} = \frac{dJ_{\text{Rec}}}{dV} = \frac{q}{nkT} J_{\text{Rec}}(0V) \tag{4.5}$$

A spatial map of the ΔV_{OC} time decay is shown in **Figure 4-4g**. The time constant associated with this process is usually taken as an indicator of recombination lifetime[33–35]. Compared with the background V_{OC} map in **Figure 4-4e**, the regions with faster recombination coincide closely with those of higher background V_{OC}. This observation is in accordance with the voltage saturation explained above, as an increased quasi-Fermi level splitting can accelerate recombination by either increasing the incidence of processes that depend on carrier concentration or by activating the large shallow trap state densities closer to the band edges. We note that region B has a similar recombination lifetime as region A, which implies that the higher recombination rate associated with B is not necessarily due to higher trap state densities but is more likely caused by the overall higher carrier concentration in this region. In general, $R \propto \frac{1}{\tau_{\text{Rec}}} \times n$, where R is the recombination rate, τ_{Rec} is the recombination lifetime, n is the carrier concentration, and τ_{Rec} could be concentration-dependent on the dominant type of recombination. We also note that our method is capable of determining parameters such as the spatial variations in the open-circuit voltage deficit by relating the PL spectra and V_{OC} map. This is realized based on the Generalized Planck law of radiation [36], similar to the method described in [20], relating the spontaneous photo-emission power spectral density to the material property and Fermi level splitting inside a semiconductor:

$$I_{\text{PL}}\left(\hbar\omega\right) = \frac{\hbar\omega^3 a\left(\hbar\omega\right)}{4\pi^2 c^2} \frac{1}{\exp\left(\frac{\hbar\omega - \Delta E_F}{k_B T}\right) - 1} \tag{4.6}$$

when the PL energy is much higher than the bandgap as well as the Fermi level splitting, the absorptivity $a(\hbar\omega)$ is close to unity and the denominator in the Bose-Einstein distribution factor can be approximated, which leads to:

$$\Delta E_F = k_B T \ln \int_{\omega_0}^{\infty} \frac{I_{\text{PL}}\left(\hbar\omega\right) c^2}{\hbar\omega^3} d(\hbar\omega) + C \tag{4.7}$$

where the integral is carried out from a fixed lower ω to nearly infinity and C is a constant independent of the measured quantities. Note here by assuming a constant ΔE_F throughout the device, we are actually extracting the effective ΔE_F averaged across the device. By subtracting the collected spatial V_{OC} map, this allows us to evaluate V_{OC} deficit, as is defined by the difference between the average Fermi level splitting across the de-

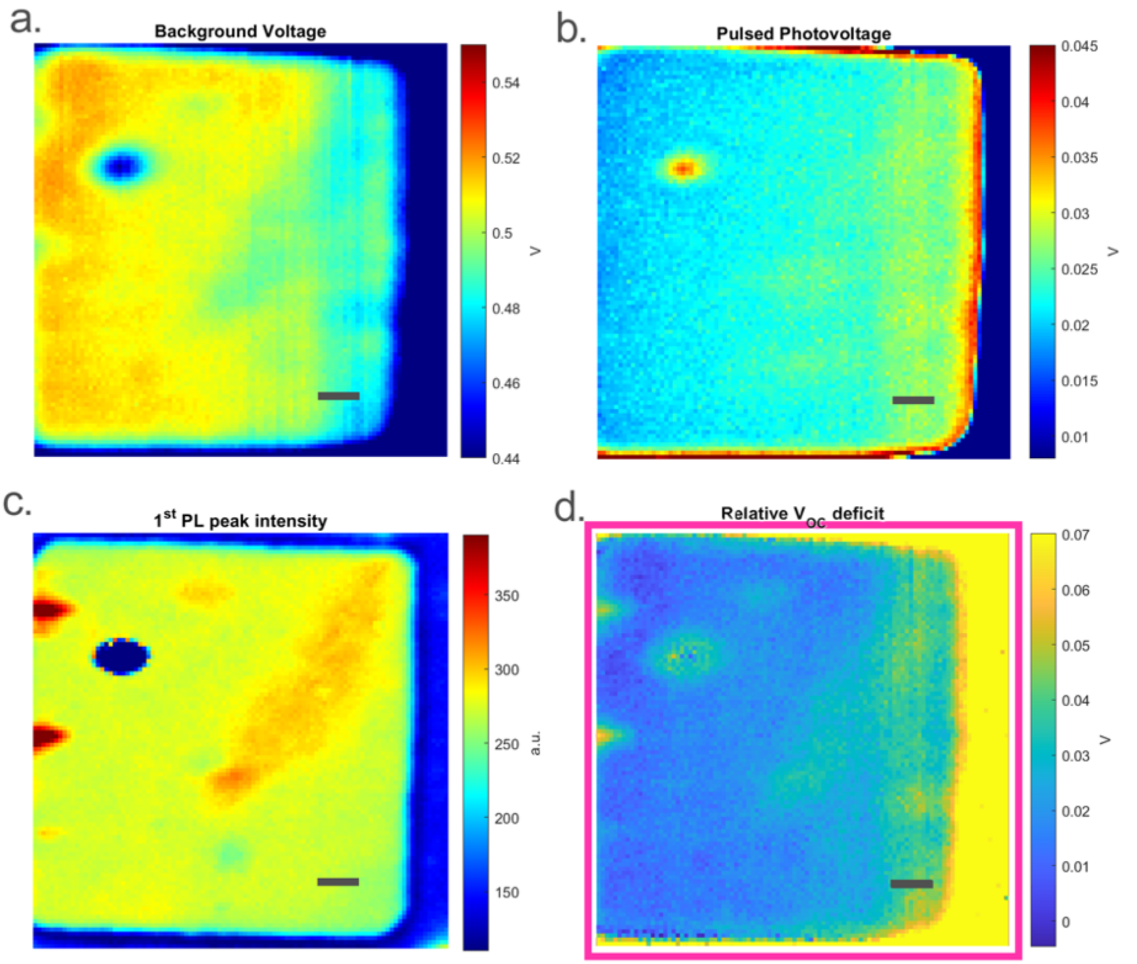

Figure 4-7. Photovoltage and PL measurements for a solution-phase-exchanged PbI_2 passivated device. The grey scale bars are 0.2 mm. **a.** and **b.** Background and pulsed photovoltage amplitudes maps, respectively, of the device. **c.** Core state PL peak intensity. **d.** V_{OC} deficit maps generated from the method described in the text.

vice and the photovoltage at the electrodes, by utilizing the high-frequency tail of the PL signal. The resulted relative V_{OC} deficit and associated maps of a different sample device is shown in **Figure** 4-7. Note that these results are only qualitative at this point since the calculation is very sensitive to the exact absorptivity as well as the accuracy of PL spectral calibration and signal-to-noise level.

As is illustrated in **Figure** 4-4, the full device area contains several regions that differ significantly in their optoelectronic properties. These regions are of 0.1–1 mm in extent, and the entire device area can be simply partitioned into a set of these regions. In the previous discussion, we manually identified two unique regions (A and B) and associated their PL, transient photovoltage, and transient photocurrent behaviors with their underlying physical properties. In order for our method to be implemented as part of a large-scale characterization protocol, it will ultimately be necessary to automate the process of defect identification and classification. Therefore, as a next step, we sought a more automated method to identify and classify spatial regions based on analysis of multiple 2D maps. We used k-means clustering, a standard statistical partitioning method commonly employed by machine learning algorithms, for this purpose[37, 38] method treats the observations as n points in a p-dimensional space and partitions all points into k clusters such that that each point lies in the cluster with the nearest mean, or equivalently, the smallest variance in distances. In our implementation, we have a set of observations with n equal to the total number of measurement points in the 2D maps, each containing p measured quantities such as PL, transient photovoltage and transient photocurrent amplitudes, and time constants. We use the k-means method to group all n points into k clusters, within which the points can be considered to have the most similar optoelectronic properties. Depending on the choice of k, we can thus automatically classify large or small regions by their properties.

Here we use transient photocurrent amplitude, background photovoltage amplitude, and pulsed photovoltage amplitude to construct a 3D space ($p = 3$). A normalization factor is applied in our model to compensate for the dissimilar units and orders of magnitude among the three quantities. Our clustered map results are shown in **Figure 4-8**. We first applied the k-means method individually to the background photovoltage (**Figure 4-8a**) and pulsed photovoltage (**Figure 4-8b**) observations such that both were treated as 1D spaces. We set the total number of clusters (k) to 6. The clustered maps show a clear resemblance to the maps of the full parameters. **Figure 4-8c** the results of clustering both background and pulsed photovoltage amplitude as a 2D data set (p = 2). Here, most areas display a similar pattern as in the $k = 1$ maps, with the notable exception of a distinct central region (in dark blue). This region displays both low background voltage and low pulsed photovoltage amplitude, and was intentionally created by excessive laser heating and ablation. The defective region at the same location is also identified in **Figure 4-2c**. **Figure 4-8d** shows the results of clustering both photovoltages and photocurrent amplitudes as a 3D data set ($p = 3$). As parameters are added to the clustered space, the maps become richer in features, and associations between the different variables are revealed. Specifically, the most inferior regions in terms of overall photocurrent and photovoltage generation are identified with bluer colors, while regions of higher quality are yellow and orange in color. This analysis is the first step in building an automatic defect identification protocol, in which device regions with specific properties as classified by their cluster type could potentially be flagged for either electronic isolation or repair. Additionally, this analysis can form the basis for a training data set for machine learning algorithms to potentially uncover additional correlations and discover new nanoscale physics.

In order to test the significance of our findings and interrogate device-to-device variations, we applied the characterization method to another device (Device 2, TBAI-PbS) with the same solar cell materials architecture and found that, despite having similar macroscopic figures of merit (J_{SC}, V_{OC}, power conversion efficiency (PCE)), the spatial variation of properties can be notably different across similar-performing devices. In **Figure 4-10a–d**, we show 2D maps of core state PL intensity, photovoltages, and photocurrent magnitudes. The maps reveal that Device 2 has slightly less spatial variation in its optoelectronic properties than to Device 1. The scanned area of Device 2 has a standard deviation in its photocurrent amplitude (**Figure 4-10b**) of $\sigma_2 = 0.051\mu_2$, where μ_2 is the Device 2 sample mean. This is a much smaller photocurrent variation than that measured for Device 1 ($\sigma_1 = 0.105\mu_1$) and indicates that the effective photocurrent loss from sub-optimal regions in Device 2 is reduced by roughly a factor of two ($^{0.105}/_{0.051} = 2.06$)

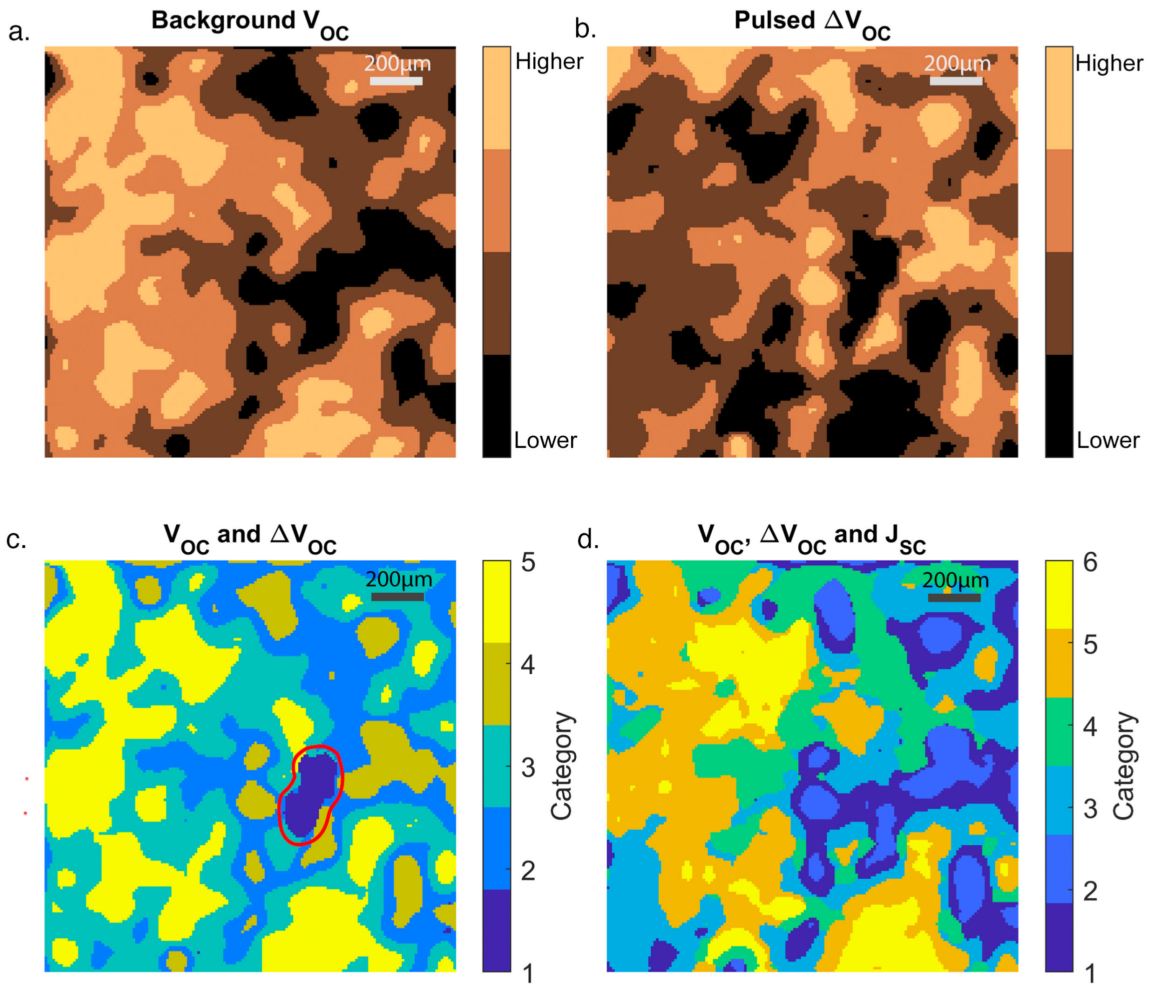

Figure 4-8. Voltage and current maps with the k-means clustering results for Device 1. **a.** Clustered map of background photovoltage amplitude ($k = 4, p = 1$). **b.** Clustered map of pulsed photovoltage amplitude ($k = 4, p = 1$). In **a.** and **b.**, different clusters are ordered and color-labeled based on the magnitudes of V_{OC} and ΔV_{OC} within each cluster. **c.** Clustered map of both background and pulsed photovoltage amplitudes ($k = 5, p = 2$). The defect region is indicated with a red contour. **d.** Clustered map of photocurrent, background photovoltage, and pulsed photovoltage amplitudes ($k = 5, p = 3$). In **c.** and **d.**, the clusters are colored in a manner that approximately associates higher performing areas with lighter (more yellow) colors. Due to the multi-dimensionality of the data and the semi-arbitrary number of clusters imposed, there is no exact quantitative association between the cluster number and film performance.

compared to Device 1, given the similar distributions of the photocurrent histograms.

Additional tests of uniformity were conducted on a solar cell device (Device S1) employing an absorbing layer with solution-phase- exchanged PbI_2-based passivation that was deposited in a single step, rather than a layer-by-layer process. **Figure 4-9a,b** contains a short-circuit current amplitude map and histogram for Device S1. It can be seen from the histogram that the photocurrent amplitude distribution is even narrower than that of Device 2 with $\sigma_{S1} = 0.037\mu_{S1}$. Additionally, the difference between the mean of the "optimal" regions, marked by rectangles in **Figure 4-9a,** and indicated by a red line in **Figure 4-9b**, and the entire sample mean is $0.03\mu_{S1}$, much smaller than the equivalent difference in Device 1 (**Figure 4-4d**). This evidence is further justification for the general trend of employing solution-phase ligand exchange methods in CQD solar cells. It provides an explanation for the improved device performance that the solution-phase ligand exchange process facilitates: this method leads to an "electronically smoother" film with less spatial variation in its photocurrent generation potential and therefore less impact from low-current regions.

Other differences can be observed in the behavior of Devices 1 and 2, as well. The apparent anti-correlation between the background V_{OC} and transient pulsed V_{OC} that was observed for Device 1 is mostly absent in Device 2, as can be seen in **Figure 4-10c,d**. Instead, most sub-regions in Device 2 have either no significant correlation or a slight positive correlation between the background and pulsed V_{OC}. Based on the previous discussion, the absence of a photovoltage saturation effect across most of Device 2 indicates that the electronic trap state densities are likely distributed to favor non-accelerating recombination rates when V_{OC} is increased due to higher illumination levels.

To further investigate this behavior, we investigated the photovoltage maps of other PbI_2-passivated devices. Such as the device of **Figure 4-7**, which displays evidence of an anti-correlation between the background and pulsed V_{OC} associated with V_{OC} saturation, similar to Device 1. In fact, the majority of the devices that we have tested exhibit this anti-correlation between the two V_{OC} components, regardless of the passivation or fabrication method employed for the absorbing layer. This appears to be a common feature of

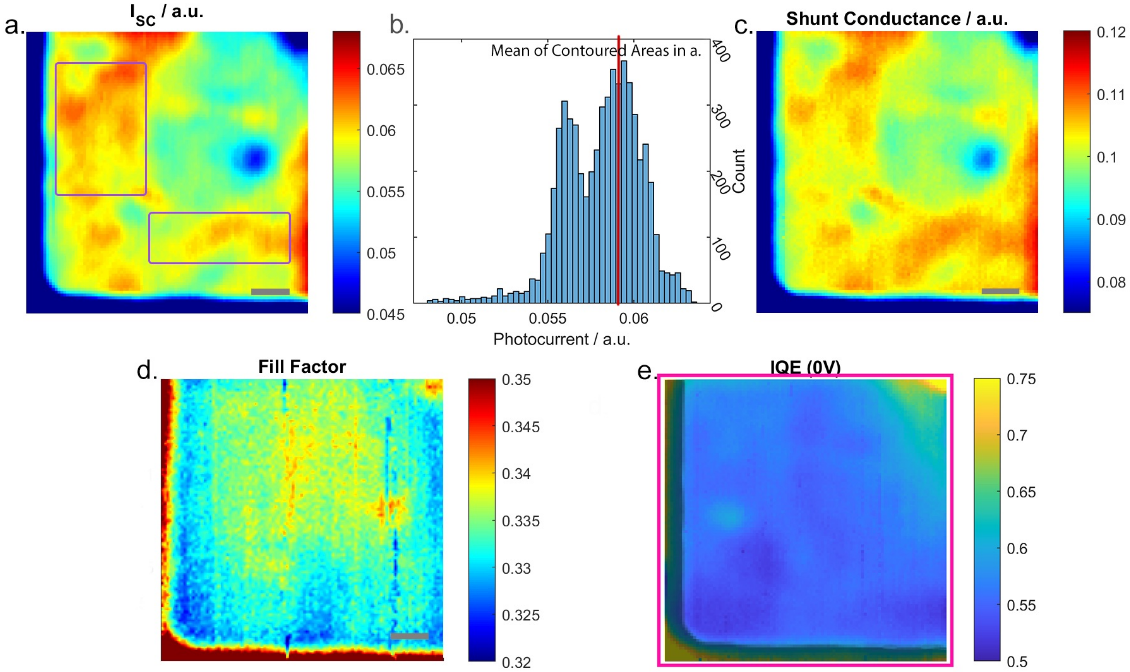

Figure 4-9. Characterization of another solution-phase exchanged PbI_2-passivated device. The grey scale bars are 0.2 mm. **a.** Short circuit current map of the device. **b.** Histogram of the short circuit current for the entire scanned device area. The mean of the photocurrent distribution for the areas indicated by rectangles in a is indicated by a red line. **c.** Shunt Conductance map derived from the IV curves near zero bias under laser excitation, as calculated by $S_{\text{shunt}} = \frac{dJ}{dV}(0V)$. **d.** Fill factor map extracted from full I-V curves of the device under laser excitation. **e.** IQE at zero bias, estimated by $IQE\,(0V) = \frac{EQE(0V)}{A} = \frac{EQE(0V)}{EQE(V_{\text{REV}})/IQE(V_{\text{REV}})} = \frac{EQE(0V)}{EQE(V_{\text{REV}})} = \frac{I_{\text{SC}}}{I(V_{\text{REV}})}$, assuming that at sufficiently high reverse bias, $VREV$ all photogenerated carriers contribute to the current.

iodine, or, more generally, halide-passivated PbS CQD films and could be due to the nature of the mid-gap or interface recombination processes associated with these materials. Exceptions such as Device 2, therefore, could provide critical insight into the fundamental origins of this behavior. Although these mechanisms are still under investigation, it is clear that devices in which the V_{OC} increases at high rates with illumination intensity are good candidates for applications requiring high power output, such as concentrated PV, even if this behavior is not necessarily beneficial for device performance under normal operating conditions. Our method, therefore, could be used as a diagnostic tool for identifying promising devices and device architectures for high-power or concentrator

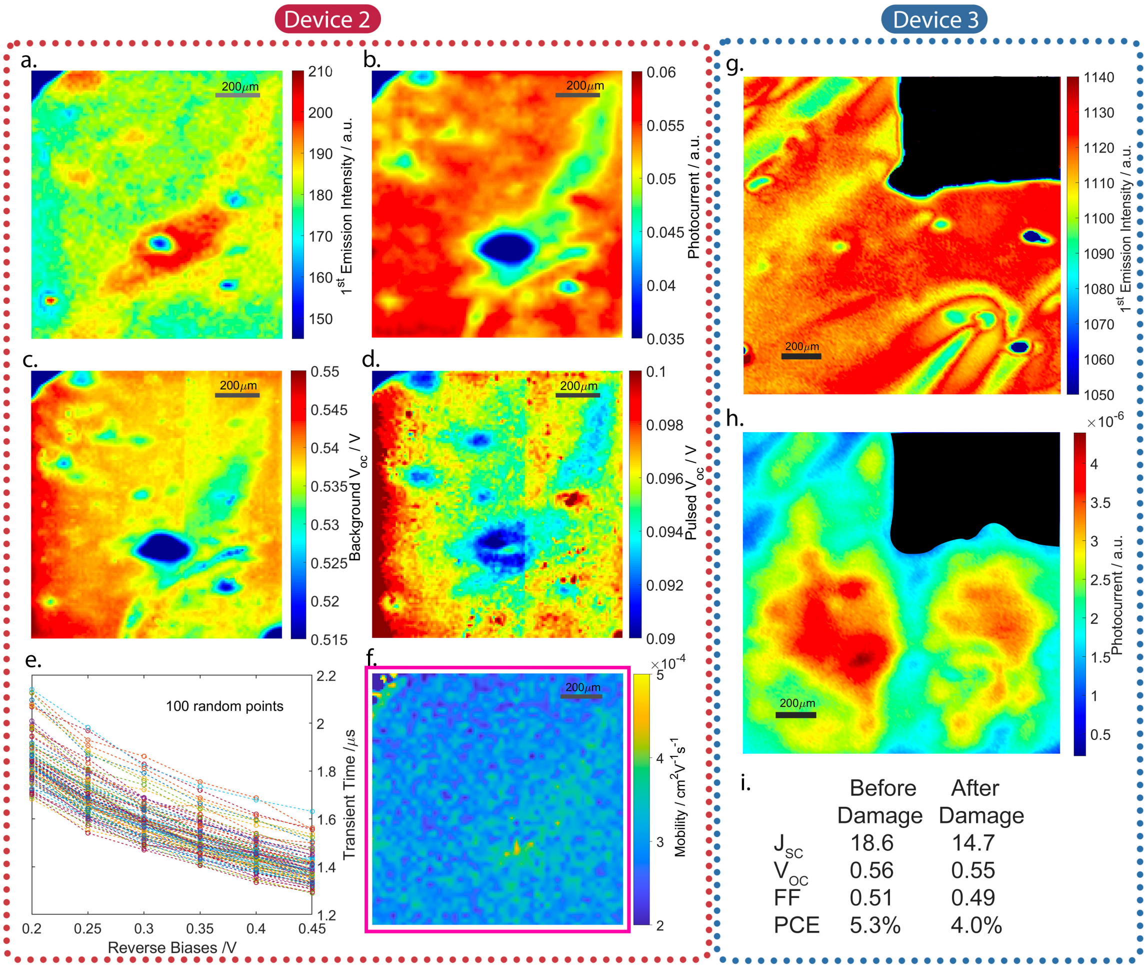

	Before Damage	After Damage
J_{SC}	18.6	14.7
V_{OC}	0.56	0.55
FF	0.51	0.49
PCE	5.3%	4.0%

Figure 4-10. a–f. Device 2 and **g–i.** Device 3 maps and statistics. Device 2 figures of merit: $J_{\text{SC}} = 20.7\,\text{mA/cm}^2$, $V_{\text{OC}} = 0.57\,\text{V}$, $FF = 0.53$, $PCE = 6.3\%$. **a.** Core state photoluminescence intensity map. **b.** Transient photocurrent amplitude map. **c.** Background transient photovoltage amplitude map. **d.** Pulsed transient photovoltage amplitude map. **e.** Charge carrier transit time extracted from transient photocurrent measurements as a function of reverse bias, from 100 random points within the same area. **f.** Carrier mobility map obtained from the transient photocurrent measurements. **g.** Core state photoluminescence intensity map for a device (Device 3) that was intentionally damaged via high intensity laser irradiation in the upper right corner, indicated by the black region. **h.** Photocurrent amplitude map for Device 3. **i.** Solar cell figures of merit for the entirety of Device 3 before and after the intentional laser irradiation-induced damage.

applications. We summarize the observed correlations between all of the primary observables that we have reported on so far in **Table** 4.2 , in order to provide a concise guide to the insights obtained by our simultaneous mapping method.

	Photoluminescence Intensity	**Photocurrent Amplitude**	**Background Photovoltage Amplitude**	**Pulsed Photovoltage Amplitude**
Photoluminescence Intensity	-	No apparent correlation	weak (–) correlation	weak (+) correlation
Photocurrent Amplitude	No apparent correlation	-	Medium (+) correlation	Medium (–) correlation
Background Photovoltage Amplitude	Weak (–) correlation	Medium (+) correlation	-	Strong (–) correlation
Pulsed Photovoltage Amplitude	Weak (+) correlation	Medium (–) correlation	Strong (–) correlation	-

Table 4.2. Correlations between primary observables for the majority of devices tested. (+) and (-) denote positive and negative correlation coefficients, respectively.

We also produced carrier mobility maps for Device 2, based on the extraction of carrier transit times for a series of reverse biases. **Figure 4-10e** shows the relationship between the transit times and reverse biases for a random choice of points within the measurement area. The full 2D mobility map is shown in **Figure 4-10f**. It is marked with a purple outline to indicate that it represents a quantity derived from two or more direct measurements; **Figure 4-7d** and **Figure 4-9e** are similarly marked. The range of measured mobilities within the map is in good agreement with hole mobilities measured for CQD solar cells from previous reports[11, 14, 27, 39]of $\approx 10^{-4}\,\mathrm{cm}^2\mathrm{V}^{-1}\mathrm{s}^{-1}$. We measured an $\approx 50\%$ variation in the mobility across the device area, with no apparent correlation with the variation in photocurrent and photovoltage. This implies that carrier mobility is a relatively uniform property within a CQD film and supports the theory that it is primarily determined by microscopic characteristics such as ligand character and electronic trap state density rather than macroscopic features associated with fabrication and handling defects.

Finally, we intentionally introduced a macroscopic defect in order to isolate the effects of a single macroscopic defect on device performance. **Figure 4-10g–i** shows the photocurrent map and current density–voltage characteristics for Device 3 (PbI_2-PbS), in which a square area corresponding to roughly 25% of the total device area was irradiated by high-intensity laser illumination. This type of irradiation is expected to lead to strong local heating and consequent ligand loss and CQD fusion and oxidation. The severity of the damage can be seen by eye in the photograph in **Figure 4-1c**. The photocurrent generation capability is completely destroyed in the damaged area; however, it remains active outside of the immediate vicinity of the defective area, with almost no apparent transition region in between. J–V testing revealed that there was a decrease in the total device short-circuit current proportional to the area of the damage after irradiation, with no obvious impact on the overall device fill factor (FF) and V_{OC}. This is a promising result in terms of device robustness and implies that macroscopic defects of this type, if spatially confined, are not fatal for device performance.

Further, this suggests that cases of complete device failure, manifested, e.g., as high shunt conductance, do not originate from conducting pathways of limited area associated with defects, but instead are more likely due to band alignment issues arising from unfavorable film compositions, which can still present as morphologically smooth structures.

We note that the measurements presented here still does not fully cover the capabilities of our system. **Table 4.3** summarizes the specific observables that we can measure using our method, the relationships between the measurement observables and parameters that can be derived from them, and the underlying device and materials properties that can be extracted from the measurements. We note that this is only a partial list relevant to the discussion in this report.

Although some of the individual properties, such as photoluminescence intensity or transient photocurrent amplitude, can be obtained with existing methods including the ones discussed in the introduction, the uniqueness of our method lies in the combinations and interactions of a rich set of multi-dimensional data enabled by our simultaneous measurement technique. Our technique allows for the extraction and analysis of more advanced physical quantities, such as 2D carrier mobility, quantum efficiency, and, potentially, electronic trap state density. Moreover, we achieve a 2D resolution and range that are not accessible to other methods, allowing for the correlation of multiple device parameters across large areas that shed light on both micrometer-scale optoelectronic materials behavior and millimeter-scale device behavior. We expect our method to yield additional compositional and optoelectronic insights in the future due to the large variety of simultaneous optical and electronic measurements that our system is capable of collecting.

Additionally, there are a number of promising analysis techniques from disparate fields concerned with large data sets that we plan to apply to our multi-modal data. These include recursive partitioning methods such as the "random forest" approach[40] that have been used for prediction, classification and correlation assessment in multiple scientific fields[41], well as regression, cross-correlation, and supervised learning algorithms[42].

4.3 Summary

We demonstrated a multi-modal spatial mapping system for optoelectronic material properties and used it to investigate local defects in PbS CQD photovoltaic thin films and their effect on device behavior. Although the hardware requirements of our system are minimal, the method produces rich, correlated, and spatially resolved information on photoluminescence, transient photocurrent, and transient photovoltage, along with derived properties such as carrier lifetimes and mobilities. Here, we analyzed the correlations between these measurements to gain both qualitative and quantitative understanding of the interplay between film absorption, carrier density, and recombination strength. We generated a carrier mobility map based on transient photocurrent measurements, which revealed that average mobility across large areas, specifically, is unaffected by complicated spatial variations in other macroscopic properties, and, therefore, that strategies to increase mobility should focus on microscopic engineering of the nanoparticle films.

In addition, by analyzing both random and intentionally introduced film variations, we found that the morphological defects introduced during the CQD film fabrication process have an impact that is limited to their close vicinity, and, therefore, are not fatal for device performance. These findings validate the common strategy of using characterization techniques that essentially average over the entire area of a device. We also provide evidence that device failures, which are usually ascribed to localized electronic shunt pathways, are more likely the result of microscale electronic variations in parameters such as energy band alignments. On the other hand, we found large spatial variations in critical device properties such as photocurrent density in areas where other properties appear uniform, suggesting that further optimization, especially in fabrication techniques and starting solution purification, is still necessary to fully realize the potential of the underlying material, due to the high sensitivity of such properties to inconspicuous physical changes.

Finally, we note that although the results presented here had a spatial resolution of $\approx$10 μm and a total area of 2 × 2 mm, our initial study was a proof-of-concept test of a configurable system and method that could potentially have much higher capabilities with the addition of more advanced optical and electrical testing accessories. With slight modifications, the system could be configured to measure a wide range of additional optoelectronic properties, including electroluminescence, electronic trap state densities, radiative recombination rates, and so on. Additionally, our system is capable of producing the large data sets required to build a training library for input into machine learning algorithms, as evidenced by the preliminary statistical clustering analysis demonstrated here. Future work will involve using machine learning techniques on the data produced by our scanning method to further probe the physical origins of phenomena such as open-circuit- voltage loss and electronic trap states in optoelectronic films.

Direct measurement modality	**Potential associated 2D maps**	**Associated derived parameters**	**Associated figures in this chapter**	**Related materials and device properties**
1. Steady-state photoluminescence (PL) spectra	Primary and secondary peak intensity, width, wavelength	Emissivity, PL quantum efficiency, V_{OC} deficit (with 3)	4-2a-d; 4-5; 4-10a,g	Film absorptivity, extent of CQD agglomeration or fusion, presence and distribution of emissive sub-band-gap states
2. Transient photocurrent	Photocurrent amplitude and carrier transit time, as a function of light and electronic bias	Carrier mobility, electronic trap state density (with 3)	4-4a–d; 4-5; 4-6; 4-8d; 4-10b,e,f,h	Electronic transport mechanisms, carrier diffusion lengths, electronic trap state distribution, device capacitance, depletion width
3. Transient photovoltage	Background and pulsed photovoltage amplitude, pulsed photovoltage decay time, as a function of light bias	Recombination lifetime, V_{OC} deficit (with 1), electronic trap state density (with 2)	4-4e–g; 4-8; 4-7a,b,d; 4-10c,d	Electronic trap state distribution, recombination mechanisms, quasi-Fermi level splitting and saturation
4. Current–voltage characteristics	Current as a function of voltage (including J_{SC}, J_{MPP}, V_{OC}, V_{MPP}), shunt conductance, series resistance, fill factor	Internal quantum efficiency	4-9; 4-10i	Solar cell figures of merit, built-in potential, recombination mechanisms

Table 4.3. Summary of direct measurements that can be made by our instrument with their associated 2D maps, potential derived parameters, associated figures in this report, and a partial list of related materials and device properties.

References

[1] Y. Lin, T. Gao, X. Pan, M. Kamenetska, and S. M. Thon, "Local Defects in Colloidal Quantum Dot Thin Films Measured via Spatially Resolved Multi-Modal Optoelectronic Spectroscopy," Advanced Materials **32**, 1906602 (2020).

[2] J. A. Christians, P. Schulz, J. S. Tinkham, T. H. Schloemer, S. P. Harvey, B. J. Tremolet de Villers, A. Sellinger, J. J. Berry, and J. M. Luther, "Tailored interfaces of unencapsulated perovskite solar cells for $>$1,000 hour operational stability," Nature Energy **3**, 68–74 (2018).

[3] N. J. Jeon, H. Na, E. H. Jung, T.-Y. Yang, Y. G. Lee, G. Kim, H.-W. Shin, S. Il Seok, J. Lee, and J. Seo, "A fluorene-terminated hole-transporting material for highly efficient and stable perovskite solar cells," Nature Energy **3**, 682–689 (2018).

[4] H. Tsai, R. Asadpour, J.-C. Blancon, C. C. Stoumpos, O. Durand, J. W. Strzalka, B. Chen, R. Verduzco, P. M. Ajayan, S. Tretiak, J. Even, M. A. Alam, M. G. Kanatzidis, W. Nie, and A. D. Mohite, "Light-induced lattice expansion leads to high-efficiency perovskite solar cells," Science **360**, 67–70 (2018).

[5] C.-H. M. Chuang, P. R. Brown, V. Bulović, and M. G. Bawendi, "Improved performance and stability in quantum dot solar cells through band alignment engineering," Nature Materials **13**, 796–801 (2014).

[6] M. Liu, O. Voznyy, R. Sabatini, F. P. García de Arquer, R. Munir, A. H. Balawi, X. Lan, F. Fan, G. Walters, A. R. Kirmani, S. Hoogland, F. Laquai, A. Amassian, and E. H. Sargent,

"Hybrid organic–inorganic inks flatten the energy landscape in colloidal quantum dot solids," Nature Materials **16**, 258–263 (2017).

[7] R. Wang, X. Wu, K. Xu, W. Zhou, Y. Shang, H. Tang, H. Chen, and Z. Ning, "Highly Efficient Inverted Structural Quantum Dot Solar Cells," Advanced Materials **30**, 1704882 (2018).

[8] B. Kippelen and J.-L. Brédas, "Organic photovoltaics," Energy & Environmental Science **2**, 251–261 (2009).

[9] J. Hou, O. Inganäs, R. H. Friend, and F. Gao, "Organic solar cells based on non-fullerene acceptors," Nature Materials **17**, 119–128 (2018).

[10] L. Meng, Y. Zhang, X. Wan, C. Li, X. Zhang, Y. Wang, X. Ke, Z. Xiao, L. Ding, R. Xia, H.-L. Yip, Y. Cao, and Y. Chen, "Organic and solution-processed tandem solar cells with 17.3% efficiency," Science **361**, 1094–1098 (2018).

[11] J. Tang, K. W. Kemp, S. Hoogland, K. S. Jeong, H. Liu, L. Levina, M. Furukawa, X. Wang, R. Debnath, D. Cha, K. W. Chou, A. Fischer, A. Amassian, J. B. Asbury, and E. H. Sargent, "Colloidal-quantum-dot photovoltaics using atomic-ligand passivation," Nature Materials **10**, 765–771 (2011).

[12] X. Lan, O. Voznyy, A. Kiani, F. P. G. de Arquer, A. S. Abbas, G.-H. Kim, M. Liu, Z. Yang, G. Walters, J. Xu, M. Yuan, Z. Ning, F. Fan, P. Kanjanaboos, I. Kramer, D. Zhitomirsky, P. Lee, A. Perelgut, S. Hoogland, and E. H. Sargent, "Passivation Using Molecular Halides Increases Quantum Dot Solar Cell Performance," Advanced Materials **28**, 299–304 (2016).

[13] K. W. Kemp, C. T. O. Wong, S. H. Hoogland, and E. H. Sargent, "Photocurrent extraction efficiency in colloidal quantum dot photovoltaics," Applied Physics Letters **103**, 211101 (2013).

[14]D. Zhitomirsky, O. Voznyy, L. Levina, S. Hoogland, K. W. Kemp, A. H. Ip, S. M. Thon, and E. H. Sargent, "Engineering colloidal quantum dot solids within and beyond the mobility-invariant regime," Nature Communications **5**, 3803 (2014).

[15]Q. Chen, H. Zhou, T.-B. Song, S. Luo, Z. Hong, H.-S. Duan, L. Dou, Y. Liu, and Y. Yang, "Controllable Self-Induced Passivation of Hybrid Lead Iodide Perovskites toward High Performance Solar Cells," Nano Letters **14**, 4158–4163 (2014).

[16]J. S. Yun, A. Ho-Baillie, S. Huang, S. H. Woo, Y. Heo, J. Seidel, F. Huang, Y.-B. Cheng, and M. A. Green, "Benefit of Grain Boundaries in Organic–Inorganic Halide Planar Perovskite Solar Cells," The Journal of Physical Chemistry Letters **6**, 875–880 (2015).

[17]Y. Kutes, Y. Zhou, J. L. Bosse, J. Steffes, N. P. Padture, and B. D. Huey, "Mapping the Photoresponse of CH $_3$ NH $_3$ PbI $_3$ Hybrid Perovskite Thin Films at the Nanoscale," Nano Letters **16**, 3434–3441 (2016).

[18]S. Y. Leblebici, L. Leppert, Y. Li, S. E. Reyes-Lillo, S. Wickenburg, E. Wong, J. Lee, M. Melli, D. Ziegler, D. K. Angell, D. F. Ogletree, P. D. Ashby, F. M. Toma, J. B. Neaton, I. D. Sharp, and A. Weber-Bargioni, "Facet-dependent photovoltaic efficiency variations in single grains of hybrid halide perovskite," Nature Energy **1**, 16093 (2016).

[19]J. L. Garrett, E. M. Tennyson, M. Hu, J. Huang, J. N. Munday, and M. S. Leite, "Real-Time Nanoscale Open-Circuit Voltage Dynamics of Perovskite Solar Cells," Nano Letters **17**, 2554–2560 (2017).

[20]M. Stolterfoht, C. M. Wolff, J. A. Márquez, S. Zhang, C. J. Hages, D. Rothhardt, S. Albrecht, P. L. Burn, P. Meredith, T. Unold, and D. Neher, "Visualization and suppression of interfacial recombination for high-efficiency large-area pin perovskite solar cells," Nature Energy **3**, 847–854 (2018).

[21]C. Jiang and P. Zhang, "Crystalline orientation dependent photoresponse and heterogeneous behaviors of grain boundaries in perovskite solar cells," Journal of Applied Physics **123**, 083105 (2018).

[22] J. Hieulle, C. Stecker, R. Ohmann, L. K. Ono, and Y. Qi, “Scanning Probe Microscopy Applied to Organic-Inorganic Halide Perovskite Materials and Solar Cells,” Small Methods **2**, 1700295 (2018).

[23] J. Chae, Q. Dong, J. Huang, and A. Centrone, “Chloride Incorporation Process in CH3NH3PbI3−xClx Perovskites via Nanoscale Bandgap Maps,” Nano Letters **15**, 8114–8121 (2015).

[24] Y. Yoon, J. Chae, A. M. Katzenmeyer, H. P. Yoon, J. Schumacher, S. An, A. Centrone, and N. Zhitenev, “Nanoscale imaging and spectroscopy of band gap and defects in polycrystalline photovoltaic devices,” Nanoscale **9**, 7771–7780 (2017).

[25] L. Hu, Z. Yang, A. Mandelis, A. Melnikov, X. Lan, G. Walters, S. Hoogland, and E. H. Sargent, “Quantitative Analysis of Trap-State-Mediated Exciton Transport in Perovskite-Shelled PbS Quantum Dot Thin Films Using Photocarrier Diffusion-Wave Nondestructive Evaluation and Imaging,” The Journal of Physical Chemistry C **120**, 14416–14427 (2016).

[26] L. Hu, M. Liu, A. Mandelis, Q. Sun, A. Melnikov, and E. H. Sargent, “Colloidal quantum dot solar cell electrical parameter non-destructive quantitative imaging using high-frequency heterodyne lock-in carrierography and photocarrier radiometry,” Solar Energy Materials and Solar Cells **174**, 405–411 (2018).

[27] C. R. Kagan and C. B. Murray, “Charge transport in strongly coupled quantum dot solids,” Nature Nanotechnology **10**, 1013–1026 (2015).

[28] M. S. Gaponenko, A. A. Lutich, N. A. Tolstik, A. A. Onushchenko, A. M. Malyarevich, E. P. Petrov, and K. V. Yumashev, “Temperature-dependent photoluminescence of PbS quantum dots in glass: Evidence of exciton state splitting and carrier trapping,” Physical Review B **82**, 125320 (2010).

[29] J. Gao and J. C. Johnson, “Charge Trapping in Bright and Dark States of Coupled PbS Quantum Dot Films,” ACS Nano **6**, 3292–3303 (2012).

[30] G. F. Burkhard, E. T. Hoke, and M. D. McGehee, “Accounting for Interference, Scattering, and Electrode Absorption to Make Accurate Internal Quantum Efficiency Measurements in Organic and Other Thin Solar Cells,” Advanced Materials **22**, 3293–3297 (2010).

[31] E. S. Arinze, B. Qiu, N. Palmquist, Y. Cheng, Y. Lin, G. Nyirjesy, G. Qian, and S. M. Thon, “Color-tuned and transparent colloidal quantum dot solar cells via optimized multilayer interference,” Optics Express **25**, A101–A112 (2017).

[32] Z. Yang, Z. Yu, H. Wei, X. Xiao, Z. Ni, B. Chen, Y. Deng, S. N. Habisreutinger, X. Chen, K. Wang, J. Zhao, P. N. Rudd, J. J. Berry, M. C. Beard, and J. Huang, “Enhancing electron diffusion length in narrow-bandgap perovskites for efficient monolithic perovskite tandem solar cells,” Nature Communications **10**, 1–9 (2019).

[33] R. Hamilton, C. G. Shuttle, B. O’Regan, T. C. Hammant, J. Nelson, and J. R. Durrant, “Recombination in Annealed and Nonannealed Polythiophene/Fullerene Solar Cells: Transient Photovoltage Studies versus Numerical Modeling,” The Journal of Physical Chemistry Letters **1**, 1432–1436 (2010).

[34] R. Azmi, S.-H. Oh, and S.-Y. Jang, “High-Efficiency Colloidal Quantum Dot Photovoltaic Devices Using Chemically Modified Heterojunctions,” ACS Energy Letters **1**, 100–106 (2016).

[35] G. H. Carey, A. L. Abdelhady, Z. Ning, S. M. Thon, O. M. Bakr, and E. H. Sargent, “Colloidal Quantum Dot Solar Cells,” Chemical Reviews **115**, 12732–12763 (2015).

[36] W. van Roosbroeck and W. Shockley, “Photon-Radiative Recombination of Electrons and Holes in Germanium,” Physical Review **94**, 1558–1560 (1954).

[37] H. Spath, *The Cluster Dissection and Analysis Theory FORTRAN Programs Examples* (Prentice-Hall, Inc., USA, 1985).

[38] D. Arthur and S. Vassilvitskii, “K-means++: the advantages of careful seeding,” in In Proceedings of the 18th Annual ACM-SIAM Symposium on Discrete Algorithms (2007).

[39] A. Mandelis, L. Hu, and J. Wang, “Quantitative measurements of charge carrier hopping transport properties in depleted-heterojunction PbS colloidal quantum dot solar cells from temperature dependent current–voltage characteristics,” RSC Advances **6**, 93180–93194 (2016).

[40] L. Breiman, “Random Forests,” Machine Learning **45**, 5–32 (2001).

[41] C. Strobl, J. Malley, and G. Tutz, “An Introduction to Recursive Partitioning: Rationale, Application and Characteristics of Classification and Regression Trees, Bagging and Random Forests,” Psychological methods **14**, 323–348 (2009).

[42] J. Schmidt, M. R. G. Marques, S. Botti, and M. A. L. Marques, “Recent advances and applications of machine learning in solid-state materials science,” npj Computational Materials **5**, 1–36 (2019).

Chapter 5

Solar Concentrator Technologies for Thin Film Solar Cells

5.1 Integrated Concentrators for Scalable High-Power Generation from Colloidal Quantum Dot Solar Cells

This section is partially adapted from Ref[1]. Reprinted with permission from ACS Applied Energy Materials 2018, 1, 6, 2592–2599, "Integrated Concentrators for Scalable High-Power Generation from Colloidal Quantum Dot Solar Cells", by Yida Lin, Garrett Ung, Botong Qiu, Gary Qian, and Susanna M. Thon, copyright © 2018.

5.1.1 Introduction

Colloidal quantum dots (CQD) have been studied extensively in recent years as a promising candidate for next-generation thin film solar cells[2–5]. Specifically, the ease of chemical synthesis and solution processing, along with the ability to tune the absorption into the near-infrared region through the quantum confinement effect, make CQD solar cells an enticing technology due to their low cost, fast fabrication cycle, and promise for flexible color-tuned photovoltaics compared with their crystalline inorganic counterparts. The designs and architectures for PbS-based CQD solar cells have evolved remarkably in the past few years with improvements in surface treatments[6, 7] and materials for charge transport layers [8–11] as well as fine control over layer thicknesses leading to devices with power conversion efficiencies (PCEs) exceeding 10% that are capable of remaining stable in air for months[12, 13]. In addition, there has been increasing interest in fabricating CQD solar cells on flexible substrates [14, 15] and patterning solar cell pixels into more complicated shapes and larger sizes for specific applications.

Although solution processability has many advantages, it also comes with several challenges in producing large-area high-quality thin films. Typically, high-efficiency CQD solar cells are still demonstrated on impractically small-area devices. Inhomogeneities in CQD and other types of thin films, including those arising from impurities in the starting solution and those introduced during the fabrication process, all contribute to possible recombination centers, shunt paths, and the breakdown of well-defined layered structures. These qualities decrease the performance of solution-processed optoelectronic devices and ultimately lead to device failure. Therefore, the active solar cell pixels are usually limited to very small areas to allow for the best possible uniformity and efficiency. Nearly all reported high-PCE values for PbS CQD devices, for example, have come from active areas of 0.1–0.01 cm^2 in area [8, 12, 13, 16, 17] corresponding to less than 1mW output power per device, assuming approximately 10% PCE at 1 sun equivalent illumination power. Some of these powers are listed in **Table 5.1**. This figure is inarguably small for practical applications when the required control electronics and complexity of wiring together enough pixels to produce a kilowatt level system are considered.

We took the view that instead of scaling up active film areas in CQD and other solution-processed solar cells, we could take advantage of the flexible processing conditions to integrate light concentration directly into the cell design itself, as a route to scaling up power output to practical levels. We achieved a maximum power of 3.2 mW

ref	PCE(%)	area (cm^2)	power output(mW)
[18]	11.3	0.049	0.55
[8]	10.3	0.052	0.54
[17]	8.4	0.054	0.45

Table 5.1. PCE, Active Areas, and Output Power from Some High Efficiency CQD Solar Cell.

from a single CQD solar cell which is an approximately 5-fold improvement over typical values reported for high efficiency cells (**Table** 5.1). Concentrator strategies based on external focusing mirrors have been widely employed in photovoltaics and solar thermal systems as a means to collect light from a large area and focus it down onto a smaller area, thereby saving on active material and increasing the light intensity at the point of energy conversion[19–21]. For example, adding a concentrator to a state-of-the-art single crystalline Si cell adds 2% PCE to the baseline of 25.6% PCE at a concentration power equivalent to 92 suns[22] Furthermore, utilization of concentrators has been crucial in record-breaking 3- and 4-junction III–V cells[23] The concentrators used for these devices are precisely optimized and manufactured to control the irradiance distribution across the different cell layers and aim to produce highly concentrated light at up to 500 suns. Many of these systems use primary and secondary lenses with large device air gaps necessary to achieve desired concentration levels and additional delicate mounting components to ensure accurate alignment [24], which compromise the cost-effectiveness and deployability of the systems.

A good solar concentrator should focus solar radiation from a large area uniformly onto a much smaller area, with acceptably small losses due to absorption and reflection in the concentrator itself. Ideally, concentrators can scale up the short circuit current proportionally to the ratio of input and output areas. Furthermore, because the open circuit voltage V_{OC} roughly scales with current as $V_{\text{OC}} = \frac{nkT}{q} \ln\left(\frac{J_{\text{SC}}}{J_0} - 1\right)$, where n is the diode ideality factor, k is the Boltzmann constant, T is temperature, q is the elementary charge, J_{SC} is the short circuit current density, and J_0 is the dark saturation current density, increases in illumination density under concentration can improve not only the total power output but also the power conversion efficiency if the fill factor (FF) of the device remains approximately constant.

Although current commercial concentrator systems have successfully increased cell efficiencies and power outputs, they come with the downsides of bulky optical elements and accessories, as described above. Solution-processed solar cell materials such as CQDs are of most interest for flexible applications such as building integrated photovoltaics (BIPV); conventional concentration systems would negate these benefits. Instead, we devised an efficient and economical method to fabricate compact, flexible arrays of concentrating lenses that can be readily bonded to the CQD solar cell substrates and effectively increase the cell collection area and power output while achieving 100% aerial light collection coverage. We numerically designed, simulated, and optimized lens geometries and used 3D printing to manufacture custom lens array molds. We then fabricated our lenses out of polydimethylsiloxane (PDMS), a transparent, flexible, organosilicon polymer, and achieved nearly 20-fold enhancement in the power output under 1 sun, and even higher enhancement under the lower illumination levels likely to be encountered in BIPV applications, after bonding to a CQD solar cell.

5.1.2 Flexible Concentrator Design and Fabrication

Microlenses, mirrors, and similar components have been incorporated into a wide variety of optoelectronic devices and are particularly fundamental to modern image sensor technologies[25, 26]. Polymer- based microlens arrays for LED out-coupling[27] related light trapping techniques for solar cells [28, 29] have been demonstrated. There has also been work on direct-contact compact lens arrays for III–V multijunction solar cells[30, 31]. The strategies used for light trapping or concentration in high-efficiency III–V solar cells are typically not suitable for CQD solar cells due to their low carrier mobilities and consequent pure vertical transport, and concentrator geometries must be more accurately controlled to match the low form factors of CQD devices. Our goal was to design a lens array that could achieve 100% aerial fill factor of a CQD solar cell device patterned with multiple solar cell pixels so that we could collect all of the sunlight impingent upon our solar cells in the same way that planar photovoltaic modules operate, without requiring the entire area of the substrate to function as a photovoltaic cell. The idea is demonstrated in **Figure 5-1a**. We designed lens arrays based on a heterojunction CQD device architecture that provides the platform for one of the highest efficiency cells demonstrated so far, comprising a transparent substrate and contact, solution-processed ZnO as the electron transport layer and tetrabutylammonium iodide (TBAI) and ethanedithiol (EDT) treated PbS CQDs as the active layers. The solar cell active-area pixels share a common bottom (illumination-side) contact and are defined by circular top contacts of 0.038 cm^2 in area.

We carried out ray optics calculations using the commercial optical design software Zemax. We set the input aperture diameter of each lens to be 1.25 cm and the pixel diameter of the solar cells to be 0.22 cm. Given a glass substrate of 1.1 mm in thickness and assuming that the solar power is incident from the back side of the substrate, we adjusted the surface profile of the lens, as well as its thickness, to ensure that the focused output light spot is as close as possible in size and location to the pixel. The lens-coupled device diagram is shown in **Figure 5-1b**.

We designed both spherical and aspherical lenses and simulated light spot uniformity at the pixel plane. To reduce the parasitic absorption inside the PDMS, we aimed at minimizing the total thickness of the lens, given a fixed entrance aperture size and pixel size, leading to hemispherical and prolate elliptical designs.

We found that aspherical lens designs were optimal for eliminating the unevenness

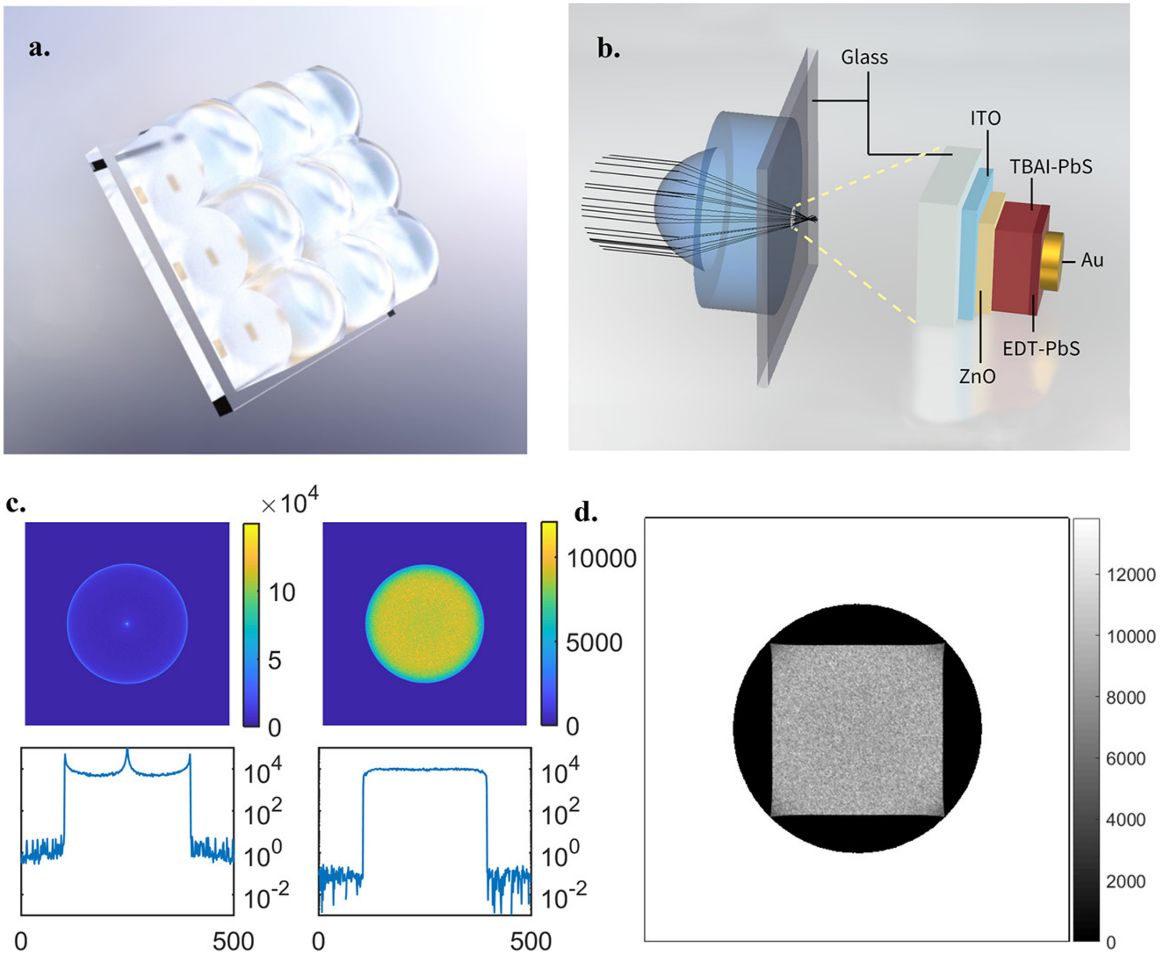

Figure 5-1. **a.** Rendering of an array of 9 PDMS concentrator lenses for integration onto a substrate containing 9 solar cell pixels. **b.** Diagram of an optimized elliptical lens including incoming light rays coupled with a device pixel on a glass substrate (left) and zoom-in of a PbS CQD device architecture diagram (right). **c.** Simulated concentrated beam profile at the solar cell pixel plane: the upper images show the in-plane irradiance distribution (a.u.), and the lower plots are line scans across the center of the pixel for a spherical lens design (left) and an elliptical lens design (right). The circular simulation area has a diameter of 2.2 mm. **d.** Light spot profile of a square sublens overlaid on the beam area of a corresponding round single lens. The circular area has a diameter of 2.2 mm, and the color bar is in arbitrary units of light intensity. The edges are nearly straight lines with a slight inward bending.

in the irradiance distribution. The aspherical lens was an ellipsoid cropped by a plane and connected to a planar slab of the same material. The specific parameters were $R =$

5.0 mm, $\kappa = -0.425$, such that the top surface was formed by rotating the curve:

$$z = \frac{r^2}{R\left[1+\sqrt{1-(1+\kappa)\frac{r^2}{R^2}}\right]}, \quad (r < 6.33\,\text{mm}) \tag{5.1}$$

where z is the surface sag and R is the radius of curvature when $r = 0$. The thickness of the planar part was 6.8 mm so that the thickest part of the lens was 13.1 mm.

As shown in **Figure 5-1c**, the simulated 2D intensity profile at the solar cell pixel plane for the hemispherical lens consists of a bright rim and center spot with irradiance over 10 times the levels of the majority of the beam area. It is important that the concentrated light intensity profile at the pixel should be uniform to avoid open circuit voltage loss due to equivalent parallel connections of subregions with uneven photocurrents. Moreover, this large unevenness could lead to unnecessarily high local carrier density for increased recombination loss and even damages to the solar cell material from intense local heating. Our elliptical lens design flattens the irradiance distribution significantly, with only a slightly weaker intensity at the rim of the beam. The total power received at the pixel plane, considering only reflection loss, was calculated to be 87.8% and 88.8% of the input power for the spherical and elliptical lens designs, respectively. Because of the smaller overall PDMS thickness, we also expect lower parasitic absorption losses in the elliptical lens.

The design and optimization were conducted using the refractive index of PDMS at 550nm in wavelength. Given that the refractive index of PDMS varies from 1.42 to 1.40[32, 33] in the 400–1000 nmregion, combined with dispersion of the glass substrate, simulations showed a variance in the beam radius of approximately ±7 % at the blue and red edges of the spectrum, resulting in an 8% transmitted power spectral density loss at the red edge and no loss at the blue edge, as shown in **Figure 5-2**. The predicted overall loss due to chromatic aberration is well within the experimental measurement uncertainty.

The geometrical concentration ratio, as defined by the ratio of the area of the lens

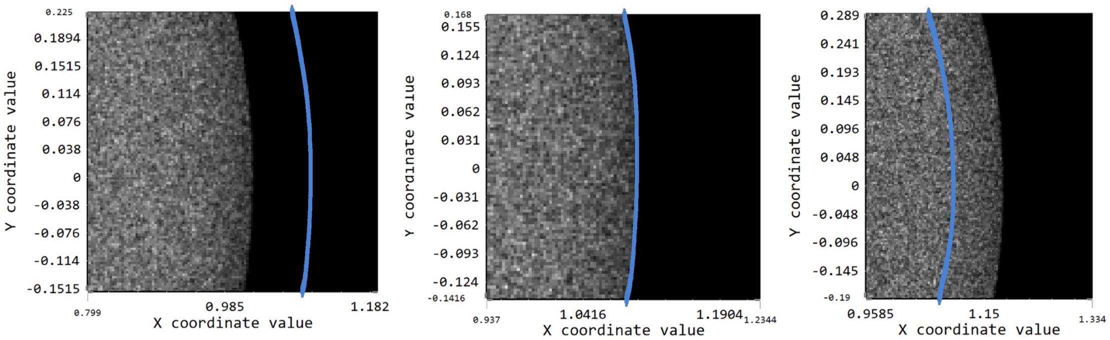

100% 100% 91.8%

Figure 5-2. Zemax simulations showing the edges of the light spots at the solar cell pixel plane for three different refractive indices of PDMS. From left to right n=1.42 (400 nm wavelength), 1.414 (550 nm wavelength), 1.406 (1000 nm wavelength). The blue curves are pixel edges and the percentages refer to the power enclosed inside the pixel.

entrance to the area of the accepting pixel, was about 31 in our optimized single lens design. A unity aerial utilization of the 27 × 27 mm substrate was achieved by designing lens arrays containing 9 identical lens units, which were cut to have square perimeters to leave no gap in light collection between pixels. The sublenses preserved the shape of the single optimized lens, and the resulting light spot had nearly straight edges (**Figure 5-1d**), enabling the simple square pixel design. The square sublenses had geometrical concentration ratios of 31.9, slightly different from the single lens ratio, due to the geometry of the light pattern through the square. The lens array can potentially collect all light impingent on the 27 × 27 mm area and focus the solar power to all 9 pixels with a total area of 22.9 mm^2, corresponding to an over 30-fold power enhancement utilization, without enlarging the standard-size CQD solar cell pixels. This design can also be modified as-needed for any thin film solar cell pixel layout.

We fabricated spherical and elliptical lenses and lens array molds using a Stratasys uPrint SE Plus 3D printer, in acrylonitrile– butadiene–styrene (ABS) plastic. The 3D printer has a z-resolution limited by its layer thickness of approximately 250 µm. Therefore, the as-fabricated molds had visible stairs and crevices, which could lead to imperfect surfaces and defects in the molded PDMS lens, causing undesired scattering and degraded beam quality. A slurry-vapor polishing procedure was used to improve the surface quality of the molds. Specifically, a small amount of ABS plastic powder (residual from the 3D printing process) was dissolved in acetone to create a slurry to fill the largest crevices in the as-printed ABS lens mold. The mold was then exposed to acetone vapor in a stainless-steel chamber for 0.5 h and then placed in air to allow the surface to reharden. This process resulted in a much smoother mold surface while preserving the critical lens geometry.

DMS concentrators and lens arrays were formed inside the ABS molds, first by combining a Dow Corning Sylgard 184 silicone elastomer base with its corresponding curing agent at a 10:1 ratio. The mixture was degassed in a mild vacuum environment for 15 min. The mixture was then transferred into the ABS mold, covered with a clean glass slide, and placed in an oven for 30 min at 80 °C to cure. The concentrators were then removed from the molds. For bonding to solar cell substrates, a thin layer of uncured PDMS elastomer and curing agent mixture was placed in between the surface of the lens and the substrate. The concentrator was aligned to specific solar cell pixels by illuminating the system with a white light source and maximizing the overlap of the beam with the solar cell pixel through the lens. The bonded system was cured on a hot plate at 70 °C for 2 h. The PDMS bonding layer thickness was negligible compared to the total lens and base thicknessThe lenses can be temporarily attached to a device for testing or can be semi-permanently bonded to the substrate, forming a stable and air-gap-free integrated system. The bonded lens elements can still be easily peeled off for replacement or reuse, without damaging either surface. Our fabrication process flow for a single lens is shown in **Figure** 5-8; the fabrication procedure for a lens array is analogous.

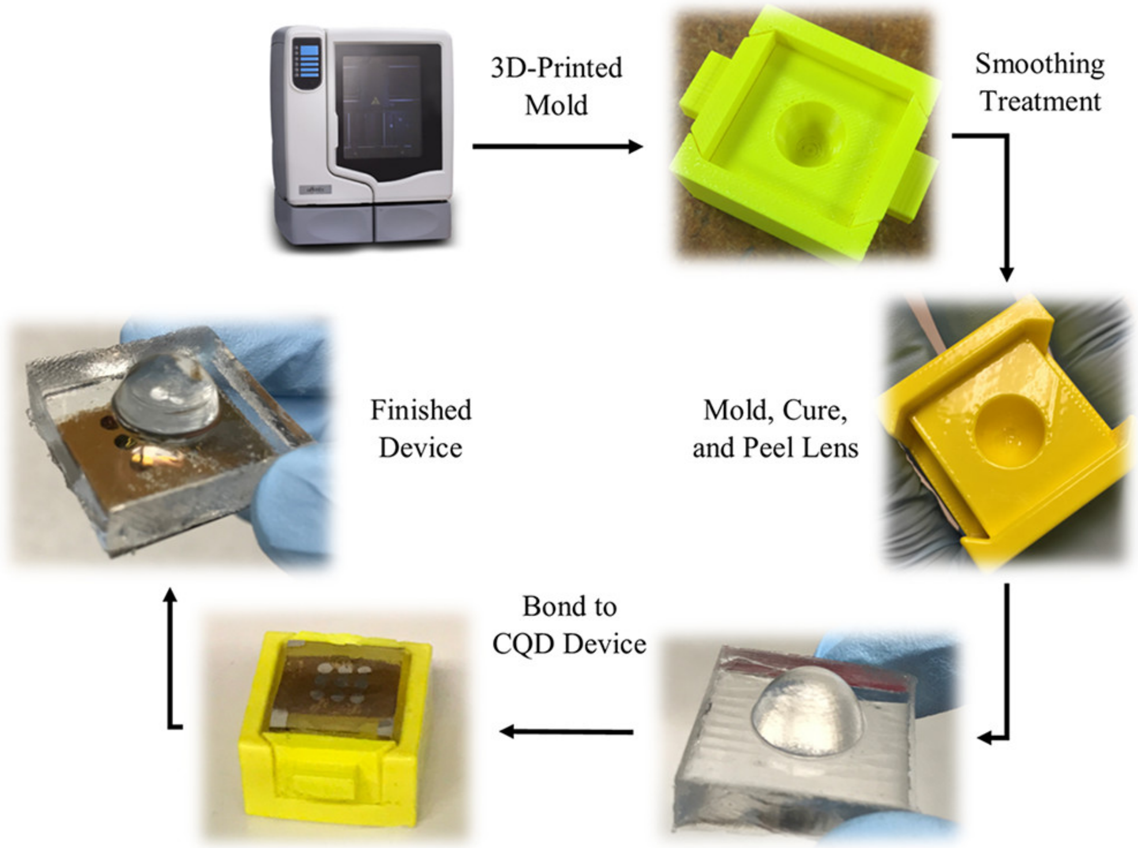

Figure 5-3. Fabrication flowchart for PDMS lens manufacturing and bonding to the solar cell device shown for a single concentrator lens (the procedure is the same for the 9-lens array).

5.1.3 Experimental Performance of the Integrated System

As shown in **Figure 5-4a**, the elliptical PDMS lens had a transmissivity of 85 %–95 % across most of the solar spectrum, indicating relatively low absorption losses in the lens material. The spherical lens had very similar transmission, as was predicted by the ray tracing simulations. The physical concentration ratio, as defined by the irradiance magnification of the concentrator, is estimated to be about 24. The Zemax simulations predicted the efficiency of the lens to be 89%, considering reflection losses. If we include the 7% absorption losses from our measurements, the predicted concentration ratio is 25. The actual concentration ratio that we measured is 24 ± 2, which matches the predictions

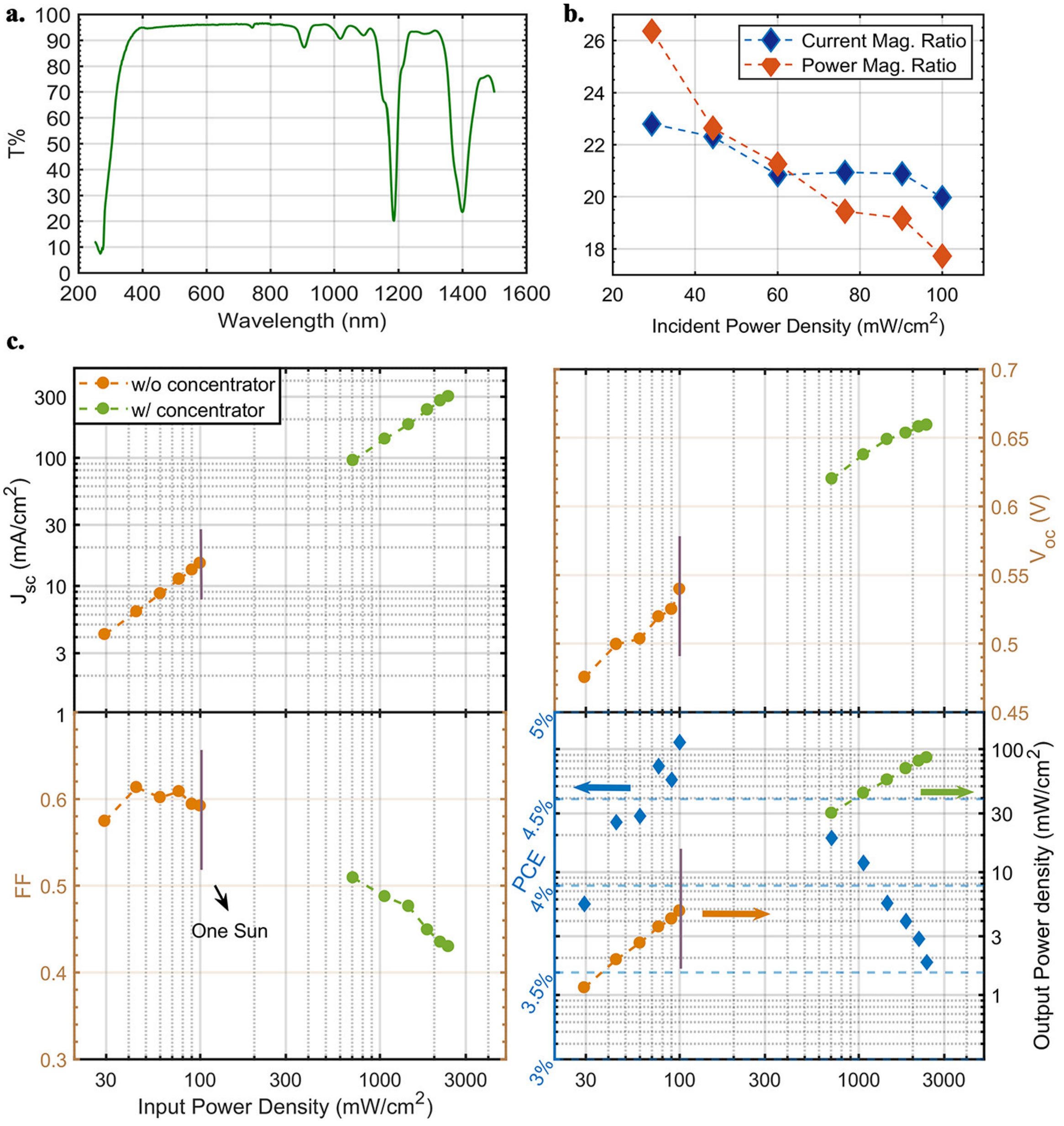

Figure 5-4. a. Optical transmission spectrum of a single elliptical PDMS lens measured in an integrating sphere, showing high transmittance across the visible spectral range. **b.** Short circuit current magnification ratio and power magnification ratio with concentrators attached at various incident power densities. An input power of 100 mW/cm^2 corresponds to 1 sun illumination. **c.** Solar cell figures of merit (J_{SC}, V_{OC}, FF, PCE, and output power density) plotted as a function of actual incident irradiance at the pixel plane. The 1 sun level is the same for all four plots. In panel **c**, the PCE is indicated by the blue diamonds in the bottom right subpanel.

from the Zemax simulations to within our experimental uncertainty.

To test the performance of the solar cells integrated with the concentrators, we measured current–voltage characteristics under simulated solar illumination applied through the same 1.25 cm diameter aperture to the front of the integrated system. Different input power levels were achieved by adjusting the output of the solar simulator as well as by testing with and without the concentrator lens. We observed a significant increase in the short circuit current after attaching the concentrator to the solar cell. The current magnification (ratio of the device short circuit current with and without the concentrator lens) is stronger when the incident power density is below 1 sun (100 mW/cm^2), reaching a value of 22.8 at an incident power of about 0.3 sun, as shown in **Figure 5-4b**. The concentrated current density at 1 sun illumination was 302 mW/cm^2, 20 times that from same solar cell pixel without concentration. The power magnification ratio is also shown in **Figure 5-4b**, indicating an overall 20-fold power enhancement with the concentrator, with a maximum at an illumination level of 0.3 sun.

The integrated system also produced up to a $4kT$ increase in V_{OC}, approaching a value of 0.67V under a concentration ratio of 24×, as shown in **Figure 5-4c**. The fill factor, however, decreased monotonically under concentration beyond 1 sun and, under most conditions, inhibited any potential for PCE improvement. Nonetheless, the output power increased monotonically with the input power density, exceeding 3.2 mW from a single pixel, equivalent to 850 W/m^2 at 1 sun illumination with the concentrator, or under an effective concentrated power of 24 suns. The test results are summarized in **Figure 5-4c**. It is worth noting that the power magnification ratio under 0.3 suns is greater than 24 (the irradiance magnification), indicating an actual PCE improvement at low light levels. The magnification trend indicates that PCE improvements can be expected for illumination intensities below 0.3 sun under concentration as well. This is advantageous for realistic applications, since solar power in most deployment locations averages much less than 100 mW/cm^2, and solar radiation levels can be under 0.3 sun for 30–40% of the daytime hours on sunny days and for even larger proportions under imperfect weather conditions.

Despite a small loss in power scaling at high illumination levels, our integrated-concentrator system was successful in harvesting solar power from an area 31 times the pixel area, resulting in 18–26 fold boosts in both current and power output at different irradiance levels.

5.1.4 Discussion of Limiting Factors

Limiting factors, including reflection (11%) and absorption (7%) losses associated with the concentrator lenses, non-ideal scattering due to imperfect surface quality, aberrations in the solar simulator beam, and misalignment between the device and the center of the beam, may account for approximately 20% power loss on the input side, as is implied by the difference between the geometrical (30.5) and physical concentration ratios (24). Further optimization of the materials and fabrication procedures could make up this gap and allow us to approach the absorption-loss limit.

Given that the J_{SC} scales almost linearly with concentration level, with a monotonic increase in V_{OC}, the decreasing power magnification ratio and PCE are caused by a drop in the fill factor at high irradiance. The most critical contribution to this drop is the series resistance contributed by the transparent conductive oxide layer (ITO). Series resistance in a solar cell causes a voltage deficit proportional to the photocurrent and effectively shifts all points in the fourth quadrant of a J-V curve leftward, eventually "straightening" the J-V curve and suppressing J_{SC}, as illustrated in **Figure 5-5a**. While the effect is minimal when photocurrents are relatively low under 1 sun illumination, it can become severe under concentration or for large-area cells, when photocurrents increase by 1-2 orders of magnitude. The ITO films commonly used as the transparent contact material typically have sheet resistance values on the order of 10–100 $\Omega\,\square^{-1}$. In the device geometry used here, consisting of a common ground, the series resistance is limited by and approxi-

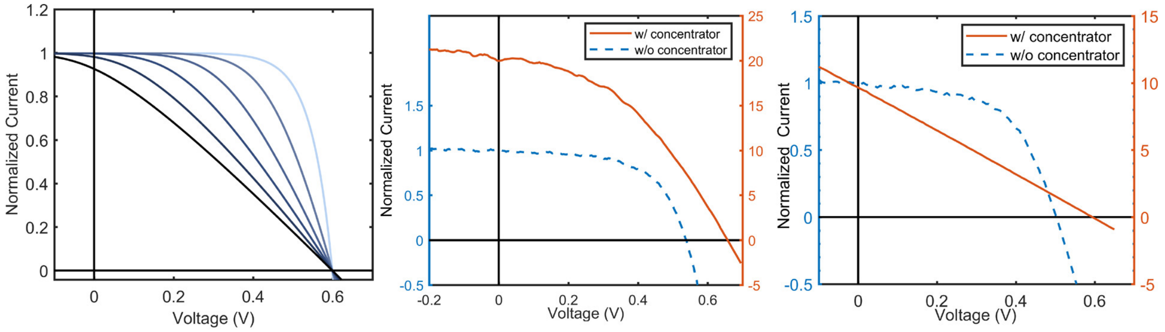

a. **b.** **c.**

Figure 5-5. **a.** Calculation showing the effect of series resistance on J-V curves. The series resistance increases from $3\,\Omega\text{cm}^2$ (lightest color) to $15\,\Omega\text{cm}^2$ (darkest color). **b.** J-V curves measured for a device using low sheet resistance $25\,\Omega\,\square^{-1}$ ITO with and without concentration. The dotted curve represents a PCE of 4.6% under sun, and the solid curve represents a PCE of 3.5% under 24 suns concentration. **c.** J-V curves measured for a device using high sheet resistance $100\,\Omega\,\square^{-1}$ ITO with and without concentration. The dotted curve represents a PCE of 5.7% under 1 sun, and the solid curve represents a PCE of 1.2% under 24 suns concentration.

mately the same as the ITO sheet resistance. Considering an active area of $0.038\,\text{cm}^2$, a maximum power point near 0.5 V, and a $25\,\Omega\,\square^{-1}$ ITO sheet resistance, the short circuit current density is limited to approximately $0.5\text{V}/0.038 \times 25\,\Omega/\text{cm}^2 \sim 550\,\text{mA/cm}^2$. For optimized PbS CQD solar cells with $J_{\text{SC}} \sim 25\,\text{mA/cm}^2$, this corresponds to a maximum concentration ratio of ~ 20. If PCE instead of total power output is maximized, the concentration ratio should be limited even further.

We experimentally verified the importance of using low-sheet resistance transparent contacts in our concentrating system. We measured J-V characteristics under different concentration levels on devices with low ($25\,\Omega\,\square^{-1}$) and high ($100\,\Omega\,\square^{-1}$) sheet resistance ITO; the results are shown in **Figure 5-5b** and **c**, respectively. Under concentration, the device with high series resistance displayed a flattened J-V curve and a J_{SC} restricted to much lower values than predicted by the concentration ratio alone.

A secondary effect can also be discerned from the J-V curve comparisons at different illumination levels. A nonzero slope at short circuit conditions, due to finite shunt resistance, is noticeable with increasing concentration. This effect can lead to J_{SC} loss when a finite series resistance is present, even if the series resistance by itself is not large enough to limit J_{SC} (See 4.5). We observed a consistent monotonic decrease in the shunt resistance with increasing solar irradiance in our experiments at all illumination levels. This could be due to the combined effects of low carrier mobilities and high recombination center density in the active CQD film. The phenomena can be qualitatively understood as follows: total current in a given solar cell device can generally be expressed as $J = J_{\text{Gen}} - J_{\text{Rec}}(V, \Phi)$, where the generation current (J_{Gen}) depends only on the integrated photogeneration rate, and can be regarded as a constant, whereas the recombination current (J_{Rec}) depends on both the applied bias, V, and the illumination level, Φ. Intuitively, J_{Rec} is nonzero at zero bias and increases with illumination level. Low carrier mobilities combined with high recombination rates cause carrier build up across the active layer and can result in a large J_{Rec}. However, J_{Rec} is still several orders of magnitude smaller than J_{Gen}, so its existence is only noticeable at high concentration level, as seen in **Figure 5-4b**. On the other hand, the derivative of J_{Rec} at zero bias reflects the shunt resistance. While the magnitude of J_{Rec} at high concentration levels has only a weak effect on the overall performance, the derivative of J_{Rec} with respect to V at zero bias can be large in a device with low carrier mobility and/or high recombination center density, resulting in slopes large enough to significantly affect the device fill factor.

In our experiment, we measured the shunt resistance at a concentration level of 24 suns to be approximately 10 Ωcm^2. We can approximate the recombination current, assuming:

$$J_{\text{Rec}} \sim \exp\left(\beta \frac{qV}{2kT}\right), \qquad \text{if } V \sim 0 \tag{5.2}$$

such that,

$$\frac{1}{R_{\text{shunt}}} = \frac{dJ}{dV}(V=0) = \frac{dJ_{\text{Rec}}}{dV}(V=0) = J_{\text{Rec}}(V=0)\frac{\beta qV}{2kT} \tag{5.3a}$$

$$\therefore \quad J_{\text{Rec}}(V=0) = \frac{2kT}{\beta qV R_{\text{shunt}}} \tag{5.3b}$$

where β is a coefficient describing how much the average Fermi level splitting scales up with applied voltage V, and is usually less than 1 at high incident illumination levels. In our case, we obtained a $J_{\text{Rec}}(V=0) = 5.2\text{–}20.8\,\text{mA cm}^{-2}$ if $\beta = 0.25\text{–}1$. Given that $J_{\text{SC}} = 302\text{mA/cm}^2$ in our experiment at 24 suns, this suggests that a recombination current of 1 or 2 orders of magnitude smaller than the generation current can lead to a shunt conductance significant enough to affect device performance. On the other hand, the recombination current is also responsible for the declining increase in or even saturation of V_{OC} at high illumination levels, as seen in **Figure 5-4c**. This is hypothesized to result from increased rates of Auger recombination at high carrier concentrations that outpace increases in the generation rate, combined with a distortion of the band bending in the CQD layer that results in lower drift currents and increased recombination rates at high irradiance. This effect is illustrated in **Figure 5-6** using SCAPS photovoltaics simulation. When the irradiance increases, the band tilting, and hence the favorable electric field near the PbS(PbI$_2$)-PbS(EDT) interface is reduced or flattened, and even with reverse bending formed at even higher illumination levels, in which case the photogenerated charge carriers rely on inefficient partial diffusion to the preferred directions, accumulate, and induce excessive recombination near this region.

5.1.5 Conclusion

We successfully tested a flexible integrated concentrator lens system and fabrication method on CQD solar cells and can, in theory, apply this technology to any thin-film solar cell architecture that suffers from scalability issues. Using an initial proof-of- con-

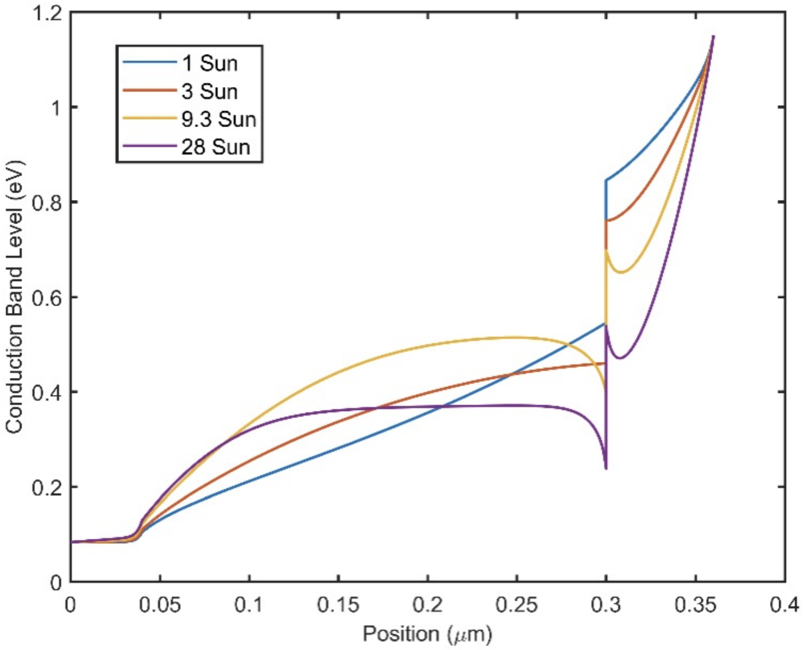

Figure 5-6. SCAPS simulation results showing the conduction band levels (ZnO-PbS(PbI_2)-PbS(EDT)), from left to right.) of a CQD solar cell under different illumination levels. Interfaces are located at 0.04 μm and 0.3 μm. Band bending at higher illumination levels becomes more unfavorable for charge extraction and hence recombination rates increase at these levels.

cept system, we were able to increase the current and power output from CQD test cells by 20 and 18 times at 1 sun, respectively, revealing the limiting factors for performance at new high illumination regimes. This work represents an immediate solution to the low-surface-area utilization in CQD solar cells and provides a method to produce practical amounts of power from these devices. We found the highest possible short circuit current densities to be limited by the sheet resistance of the ITO electrodes as well as fill factor drops caused by increasing recombination currents at high illumination levels. This suggests an optimal concentration level for thin film solar cells using similar transparent electrodes to be less than 30. Also, PbS CQD solar cells could benefit even further from enhanced carrier transport and limited recombination under high illumination levels.

Our integrated concentrator system provides a promising and practical solution to scalability issues in thin film solar cells while maintaining their essential fabrication and flexibility benefits for building-integrated and next-generation photovoltaics. Future work includes design and optimization of concentrators with large-angle acceptance capabilities to collect diffuse light and the adoption of emerging TCO materials such as solution-processed ITO and Ag nanowires, in pursuit of better transmittance and conductance compared to conventional ITO. Metal-grid electrodes are also a potential alternative [34] although the specific line widths and spacings of the grid lines, as well as the manufacturing process must be carefully adjusted and optimized to achieve substantial improvements over traditional TCOs in low-diffusion-length platforms such as CQD solar cells. Additionally, utilizing high-resolution 3D printing technology will help reduce scattering losses, allow for the integration of complex photonic light-trapping structures, and enable high-resolution Fresnel lens designs with better compactness. In addition to CQD-based solar cells, our flexible concentrator systems can be readily integrated with other types of thin-film solution-processed solar cells, including organic photovoltaics and perovskites, enabling practical scale-up and manufacturing of high-power low-cost solar cells.

5.2 Diffuse Solar Micro-concentrators Using Dielectric Total Internal Reflection with Tunable Side and Top Profiles

Photovoltaics (PV) is one of the most promising renewable energy technologies thanks to the ubiquitous access to solar radiation around the globe as well as the development in multijunction PV electronics that has increased power conversion efficiency (PCE) above the single junction efficiency limits in the last half century. To fully realize the power production potential of PV, solar cells with higher PCEs and deployment in greater areas are required. Although the costs of silicon solar cells have been dramatically reduced in recent years, multi-junction solar cell technologies based on III-V semiconductors with the highest PCEs still suffer from high unit costs due to expensive materials and complicated fabrication processes[35], and are therefore used almost exclusively in space applications or small installations that are impractical for large-scale terrestrial power production [36]. Concentrator PV (CPV) systems have long been regarded as a potential solution to such difficulties. The implementation of optical concentrators allows for the harvesting of solar radiation from a much larger area than that of the PV device, by replacing expensive semiconductor materials with less expensive materials for the optics. Moreover, it is well known that solar cells made from high-mobility crystalline materials can benefit from higher incident radiation intensities to create higher PCEs at increased open circuit voltages (V_{OC}), making concentrators almost a necessary component for large-scale commercialization and terrestrial deployment of III-V high PCE multijunction solar cells [23, 37].

Building Integrated Photovoltaics (BIPV) is a popular implementation of PV systems. Direct integration of PV into the building envelope enables utilization of a large amount of existing surface area to generate power and reduces costs associated with electricity transportation and distribution. CPV can provide more flexibility to BIPV technologies by reducing the usage of sensitive and expensive electronic materials, and integrated concentrators can perform a dual role as encapsulants for environmental protection. However, traditional CPV is highly directional and requires bulky external tracking elements that are not compatible with BIPV. Here, we develop a novel design for dielectric total internal reflection concentrators (DTIRCs) [38] that uses a tunable phase shift to increase both the acceptance angle and concentration ratio over conventional designs, potentially exceeding the limit imposed by *etendue* conservation[39]. Using our design, we calculate the annual solar power our concentrators could collect and compare this to traditional direct concentrator and standard DTIRC designs. The ability of our concentrators to collect diffuse light while maintaining high concentration factors makes them a good candidates for BIPV and other applications requiring high efficiency, low cost PV technology.

Although the basic concept of all concentrator systems involves directing light from a large area to a smaller area, concentrators come in many different types. Early work focused on using external Fresnel lenses to direct light to a small-area solar cell as a straightforward solution[40]. Later, concentrator optics evolved to enable more accurate control of the direction of the light and, more importantly, to allow for some finite-acceptance-angle and diffuse-light-collection capabilities. These included compound parabolic concentrators (CPC) [41] dielectric total-internal-reflection concentrator (DTIRC)[38]. Conventional concentrators are designed only for normal-incidence radiation, and thus the power accepted by the solar cell drops sharply outside of a narrow acceptance angle of 1-2 degrees. CPCs and DTIRCs, on the other hand, are able to maintain a power multiplication ratio that is close to the geometric concentration ratio of the design over a much wider angular range up to the specified acceptance angle. DTIRC concepts were first described in the 1980s and have more flexibility in their geometric profile to accommodate for different combinations of acceptance angle, concentration ratio and overall aspect ratio. They usually have a higher concentration ratio for the same angular acceptance than CPCs, due to the incorporation of refractive media and the higher sidewall reflectance due to total internal reflection (TIR). Moreover, design and generation processes for DTIRCs have been developed to enable two-axis wide-angle acceptance and concentration[42, 43], thus made possible thus making it possible for them to operate fully without tracking systems.

The fundamental aspects of DTIRCs have been studied extensively. Recent work has mostly focused on specific applications without major efforts to re-evaluate the basic principles. Here, we demonstrate that it is possible to improve the concentration ratio for a given acceptance angle in a DTIRC by careful re-evaluation of the relationship between the top surface and sidewall geometries. We modified the traditional DTIRC design by using a top surface profile with an inherent sharp turning point, an additional phase, and an associated intermediate segment gradient inserted between the top and bottom segments of the traditional DTIRC sidewall, effectively enlarging the upper portion of the concentrator. We note that in deriving the sidewall profile of the DTIRC, *etendue* conservation is assumed in the conserved-phase method[39] While the maximum concentration method yields very similar results, an increased concentration ratio at a given acceptance angle in the designs resulting from our method means that the limit imposed by *etendue* conservation can be at least nominally overcome. We also found that additional optimization is required to generate the intermediate segment geometry to avoid incident light at lower angles of incidence (AOI) from being reflected out of the structure due to the sudden change in the slope of the sidewall.

In our design, the top surface profile (the entrance aperture) that involves a turning point at the center, can be either a flat surface, a conical surface, or a macroscopically-flat surface containing concentric sloped micro-rings, resembling the surface of a Fresnel lens. The generation process for the full 3D sidewall profiles is based on the sequential generation of planar sidewall contours of the cross-sections rotated about the central z-axis, all of which share the same top surface profile. In this way, an axially symmetric top surface is guaranteed and is smooth with only a central angled point if the conical-type option is chosen. This reduces the challenges in fabrication compared with traditional DTIRCs that contain complicated curvilinear structures or ridges in the top surface [43].

5.2.1 Design Methods and Results

The design process for our DTIRC concentrators starts by considering the cross-section with respect to one of the principal axes perpendicular to the solar cell plane. The (half) acceptance angle θ_A is predefined, along with the shape of the top surface profile, which can, in theory, be any shape with axial–symmetry, such as an arc of a circle, an ellipse, or a combination of straight lines. Specific cases will be considered in the following sections.

Due to the scalability of DTIRC structures, the width of the output plane (i.e., the solar cell width), d_0, can be assigned any value. All other structural parameters are defined in relationship to d_0 and thus can be scaled proportionally. **Figure 5-7a** shows a diagram of a cross-sectional slice through the center axis of a generic DTIRC with a spherical top surface. The relevant lengths are labeled. In this case, before the numerical generation of the entire profile, only the angle subtended by the top surface arc, 2ϕ, needs to be pre-defined, and the radius or size of the circular top is mathematically determined as a result of the design generation process.

Following the principles of DTIRC profile generation[38, 39], the light rays incident at θ_A are first refracted by the top surface, at an angle determined by the refractive index of the material. When the refracted rays reach the sidewall and undergo TIR, the upper portion of the rays are directed to the bottom corner of the opposite wall of the structure while the rest are distributed across the bottom surface. The lower portion of the sidewall can be defined in 2 different ways [38, 39]: The former requires the corresponding rays to propagate in parallel after hitting the lower segment of the sidewall, while the latter requires that each ray hit the lower sidewall at exactly the TIR critical angle. It has been shown in previous work that the MCM usually yields a slightly better (1-2%)[38, 43] geometric concentration ratio. We will base our calculations on the PCM because of its higher efficiency in calculation, noting that our strategy of improvement can readily adapt to either method.

Using the PCM for conventional DTIRCs allows simplification of the generation process by defining one piece of additional critical information: the size of the entrance surface, $d1$, by applying the rule of *etendue* conservation nominally [39, 41], so that:

$$d_1^2 \sin^2 \theta_A = n d_0^2 \sin^2 \theta_0 \tag{5.4}$$

where θ_0 is the tilt angle of parallel rays exiting the bottom surface. *Etendue* conserva-

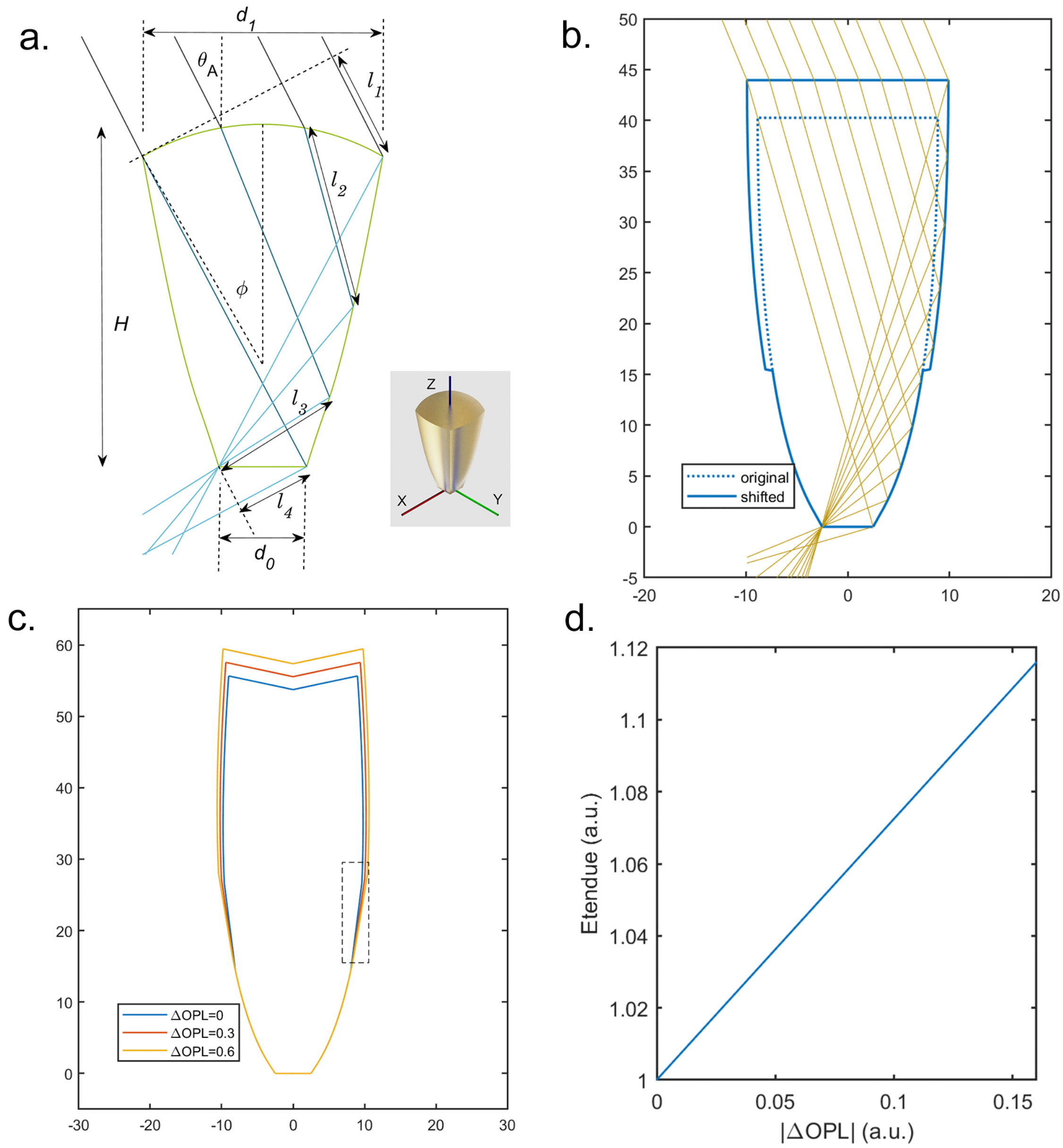

Figure 5-7. a. Diagram of the cross-section of a conventional DTIRC with a spherical top. The insert shows a 3D rendering of the same cross-section, with the coordinate system labeled used later in this section. **b.**Cross section illustrating the effects of a staggered sidewall profile (solid) that increases the OPLs of some of the rays, without changing the propagation directions of the rays in the original design (dashed). **c.** Cross- sections of three DTIRCs with a turning point in the entrance surface combined with a corresponding ΔOPL on the sidewall. The outlined region indicates the straight-line connection points for the upper and lower profiles.**d.** Normalized nominal *etendue* as a function of ΔOPL computed by $\frac{d_1 \sin\theta_A}{n d_0 \sin\theta_0}$.

tion, as the fundamental principle that governs illumination optics under certain circumstances, also conceptually indicates here, the trade-off between the geometric concentration ratio (roughly equals to d_1^2/d_0^2) and the acceptance angle θ_A.

As shown in **Figure** 5-7**a**, the path length of a given ray is divided into 4 segments. When phase conservatio method is assumed, a ray either hits the bottom corner or reaches a linear wavefront that intersects the bottom corner. This condition can be satisfied if all rays have an identical sum of optical path lengths (OPLs) of the 4 segments, as described by Fermat's principle. If this is true, a smooth top surface should only result in smooth changes in all 4 segments of the OPLs during the calculation, and naturally leads to a continuous and smooth sidewall profile. However, rays propagating between two wavefronts do not need to have equal path lengths. A common example is rays that are focused by different rings from a Fresnel lens. In **Figure** 5-7**b**, we show a DTIRC with a flat top surface, that has an OPL difference assigned for part of the rays that travel with a longer OPL than the rest, creating a discontinuous staggered sidewall. In the figure, a design generated from the same input parameters but with a constant OPL is overlaid for comparison. The modified structure still satisfies the requirement for rays incident at θ_A to be exactly contained in the bottom segment, along with other predictions from PCM, as illustrated by the ray diagram, but this time the upper part expands over the original design for a larger entrance surface size, and a correspondingly higher geometric concentration ratio.

However, this design does not necessarily yield better overall optical performance. The discontinuous offset in the side profile produces a gap, and there is a chance that rays can hit the gap, either after they enter the structure or after they are first reflected by the upper sidewall (i.e., the case for rays with small AOIs). The rays will then be redirected away from the bottom plane and contribute to collection loss. The situation is worse for rays with incident angles much smaller than θ_A, in which case a larger percentage of the rays is subject to hitting the gap. This is not a concern for the original DTIRC design, as ideally all rays with incident angles smaller than θ_A are guaranteed to be directed to the bottom plane

TThe gap in this example arises solely from the arbitrary OPL differences that are assigned to rays entering through an initially smooth (flat) entrance surface. Straightforwardly, in contrast, an entrance surface that has a sharp turning point will create a corresponding turning point in the sidewall profile, so that the profiles will have discontinuous slopes, and hence become non-smooth across the turning point. If at the same time, the OPL difference is intentionally introduced exactly at the turning point, then by carefully tuning the combination of the entrance surface profile and the OPL difference, the resulting sidewall gap can be designed to posses a less abrupt and more monotonic transition between the upper and lower part of the rays, lessening or eliminating the problem in the previous ex- ample. For this purpose, we have found that for the top surface profile, a simple two-piece line segment (effectively a cone in 3D) is a good candidate. As shown in **Figure 5-7c**, we generated a series of DTIRC cross-section profiles with different OPL differences based on this type of entrance surface with a 12° symmetric inclination. The intermediate segments here, or the gaps, are simply straight lines connecting the upper and lower parts of the sidewall. A non-negative $DeltaOPL$ corresponds to a longer OPL for rays hitting the right portion of the entrance surface. Note that all side profiles in **Figure 5-7c** show relatively less drastic changes compared with the examples shown in **Figure 5-7b**, and thus avoid excessive abnormal ray paths, while maintaining an increasing entrance surface size with a greater ΔOPL. An important property is that in all of these examples, the ratio of the projected lengths, d_1/d_0, exceeds the limit defined by the nominal *etendue* conservation, as all profiles share the same set of parameters except d_1. **Figure 5-7d** shows the relationship between ΔOPL and the normalized nominal *etendue*, which should be unity as indicated by the conservation law.

However, even with this design, the ΔOPL cannot be set arbitrarily large before severely compromising the optical efficiency. It can be understood intuitively that not

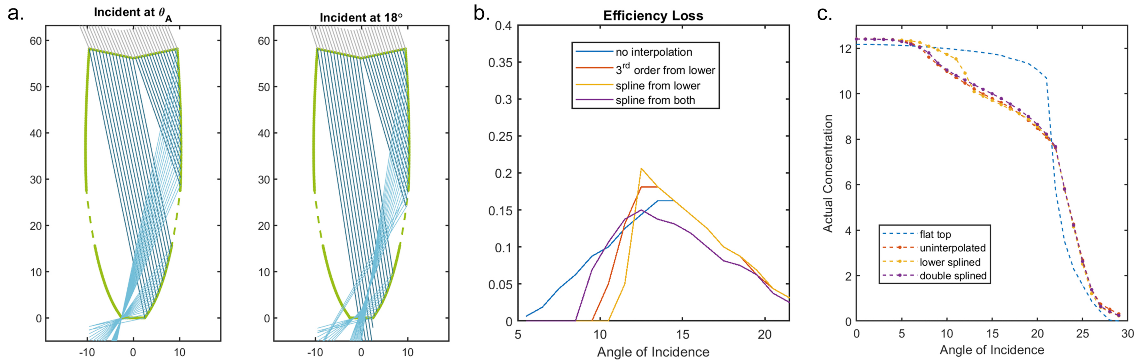

Figure 5-8. **a.** and **b.** Diagrams showing the behaviors of rays incident at θ_A and at smaller angles, respectively. **c.**Comparison of the efficiencies for different interpolation methods calculated at the cross-section plane. **d.** Concentration ratios as a function of AOI calculated from ray simulations of full 3D DTIRCs for different geometries.

only the slopes of the sidewalls, but also the behavior of the curvature over the intermediate segment, determines if rays are reflected at undesirable angles and ultimately not collected at the bottom plane. In **Figure 5-7c**, it can be seen that as ΔOPL increases, the slope of the intermediate segment becomes closer to that of the lower portion and diverges more from that of the upper. If this segment was interpolated, it would undergo a flatter transition downward, while the curvature near the connection point with the upper portion would eventually become too large for rays hitting this part to still be reflected to the bottom plane, again causing efficiency loss. This effect is demonstrated in **Figure 5-8a** and **b** with the intermediate segment interpolated as described in the caption. In **Figure 5-8a** the rays incident at exactly θ_A can avoid hitting the sidewall gap and are received by the bottom plane. However, in **Figure 5-8b**, some of the rays at AOIs less than θ_A, hit the interpolated portion of the sidewall, and exit through the opposite sidewall. This implies that the magnitude of the ΔOPL and the way the intermediate segment is interpolated are critical in limiting the efficiency at angles smaller than θ_A.

In **Figure 5-8c**, the approximate 2D cross-sectional optical efficiencies of the DTIRCs with the same ΔOPL but intermediate segments interpolated using different methods are plotted against the AOIs. These efficiencies are obtained by taking the percentage of the rays exiting through the sidewalls. The behaviors of the DTIRCs resulting from different sidewall interpolation methods are compared. We find that the efficiencies for vertical incidence rays and rays incident at θ_A are maintained at near unity for all methods. The exact interpolation method primarily affects efficiencies in the middle AOI range between these two extremes. Compared with straight-line connections, interpolation reduces the loss of rays after hitting the gap due to a sudden change in the sidewall slope, and interpolation towards the endpoints of both the upper and lower profiles further reduces losses for incidence angles of around 15–20°, yet at the cost of an earlier drop in the efficiency curve.

The full 3D structure for our DTIRC design must be generated to accurately evaluate and understand its performance. We apply the generation procedure described above for 2D cross-sections at each azimuthal angle (angle along the z-axis in **Figure 5-7a inset**), given the projected d_0 at each angle from a predefined bottom solar cell contour, and impose the condition that the shape of the top entrance surface must be preserved and continuous for all azimuthal angles. The examples shown in **Figure 5-82** will therefore have a conical top surfaces in their corresponding 3D structures. This method ensures that the entire DTIRC structure bears the symmetry of the bottom solar cell plane. Here, we consider a recipient solar cell with a square shape - d_0 is equal on the two major axes x and y, and so is the θ_A for the DTIRC on these axes. For all generated 3D profiles, we then test the single-axis angular dependent actual concentration ratio, defined as the total power received at the solar cell plane at a certain angle divided by that received without any concentrator at normal AOI. As a comparison, the method used to generate the 2D efficiency plot in **Figure 5-8c** should be considered as a quick test of the effects of the interpolated segment before completing the full 3D simulation, which is necessary to obtain the true efficiency of a 3D structure as well as the concentration ratio. In **Figure 5-8d**, efficiency results for the concentrator with a conical top with a 12 degree inclination angle, and a θ_A of 22.5° on both major axes with different interpolation methods are presented. We chose a material refractive index n of 1.42, for the lens material, corresponding to the value for PDMS, to demonstrate the potential of our designs when made from a flexible, affordable and environment-friendly, yet relatively low-indexed polymer material. For a baseline, we include the result for conventional DTIRC with a flat entrance surface and a $\theta_A = 21°$ because its nominal geometric concentration ratio of 12.5 is close to 12.7, the concentration of our improved design.

All of the DTIRC designs explored so far have efficiencies close to unity at low AOIs. The conventional design maintains this efficiency at AOIs close to θ_A, while the efficiency curves of our new designs start to decline at smaller AOIs due to the aforementioned issues with the intermediate segment continuity, but have wider angular acceptance ranges as predicted by a 1.5° larger design θ_A. The efficiency differences at intermediate AOIs between the different interpolation methods are qualitatively consistent with the 2D cross-sectional efficiency test shown in **Figure 5-8c**. Simplistically, the conventional design seems to outperform all new designs if the enclosed area under the efficiency curve is taken as the overall ability of the DTIRC to receive and concentrate solar power from a moving source traversing a dome of angles. This is true when only single-axis acceptance is considered. However, if we consider the movement of the sun across the celestial sphere over the course of a year, incidence at larger AOIs should contribute considerably more to the total received solar power at the concentrator input, thus favoring structures with wider acceptance capabilities.

To calculate the annual collectible power of different DTIRC designs, the sun's position at all times of the year must be known. Given the latitude of the location of interest on the surface of the earth, the time of day and time of year, the obliquity of 23.5°, and ignoring anomalous motion of the earth's revolution and rotation, the sun's course in terms of the polar angle θ and azimuthal angle ϕ with respect to the local terrestrial normal vector can be analytically solved. The results are shown in **Figure 5-9a**, for a latitude of 39.3°, corresponding roughly to Baltimore, Maryland. The sun's trajectory is sampled with a constant interval of 15 min within each day and 10 days throughout the year. For a static concentrator mounted perpendicular to the ground, the figure shows the range of angles that it will receive solar power from. It can be straightforwardly determined that the orientation that maximizes light collection for a static concentrator is the angle corresponding to the sun's location at noon on the equinox, i.e., directed to the centroid of the sun's annual course. In this case, the full angular acceptance range of the concentrator can be better utilized. The results of the (θ, ϕ) for this orientation are shown in **Figure 5-9b**. Note that for terrestrial locations not on the equator, the sun's trajectory is not exactly symmetric about this orientation due to the relative lengthening and shortening of the daytime in the summer and winter, respectively. However, this has no effect on the concentrator efficiency because the imbalance only occurs for small elevation angles corresponding to $\theta \sim 90^\circ$, well outside of the acceptance range of any practical concentrator.

We calculated the annual collectible solar power by considering the average annual concentration ratio for different DTIRC designs assuming that the concentrators are oriented at the optimum angle. For this step, instead of obtaining 2D concentration maps in the local angular space (θ, ϕ), we found it more convenient to sample the maps over constant intervals. Because of the varying angular velocity of the sun in (θ, ϕ) space, sampling at constant temporal intervals allows us to calculate the total average annual concentration ratio via direct summation of the sampled data, as long as the sampling grid is sufficiently fine. The angular position of the solar source at a specific time can then be derived, by successive rotation about X-axis by the declination angle $\delta = \arcsin\left(\sin 23.5^\circ \sin\left(2\pi \frac{d}{a}\right)\right)$ and rotation about Y-axis by the hour angle $HRA = \frac{\pi t}{12\,\mathrm{h}}$, where a stands for the total number of days in a year, d for the number of days past the equinox, and t for the time past noon. The angle of solar radiation along X-axis never exceeds 23.5° and that is the reason we have chosen 21° and 22.5° respectively, for θ_A in the conventional and new designs, in order to fully utilize the diminishing but still finite

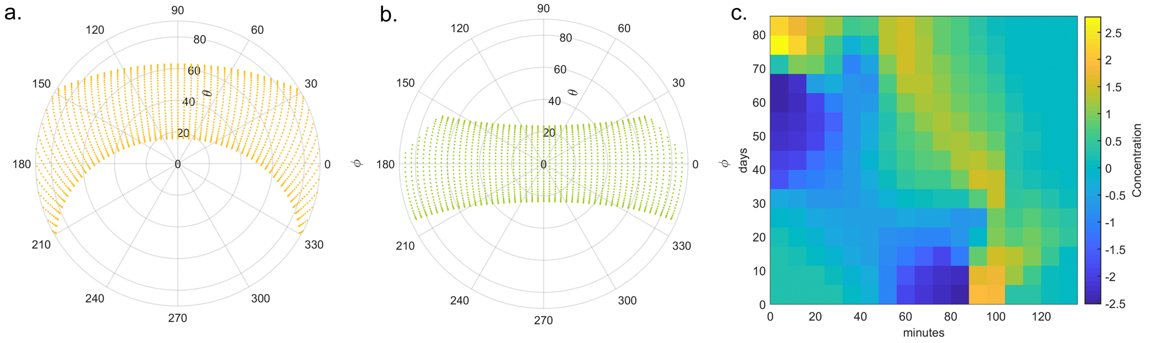

Figure 5-9. **a.** The sun's position throughout the year in the local terrestrial angular space (θ, ϕ). **b.** The sun's position relative to the concentrator for optimal orientation. **c.**Difference in concentrations between the original and new DTIRC design as a function of time day and year relative to noon and the equinox.

angular acceptance beyond the designed θ_A. We also found that a 16×16 grid for a quarter of the fourfold-symmetric 2D concentration map (equivalent to a 31×31 grid for the full range) yields sufficiently accurate results. In **Figure 5-9c**, a full year time-dependent concentration difference map between the improved DTIRC design and the conventional DTIRC design are shown. The results agree with the 1D line scan in that the new design outperforms the conventional design on the edges and the center. The total annual average power is hence calculated to be 1.035 suns for the conventional design and 1.056 suns for the new design. The new design provide approximately 2% more power overall for the recipient solar cell despite its disadvantages at intermediate AOIs. In comparison, a static flat panel receives only 0.305 suns on average annually, indicating that utilizing a DTIRC can enable at least a 3.5-fold increase in power per unit area over the course of a year.

We also carried out optical simulations to calculate the efficiency of different DTIRC designs in collecting diffuse solar power. The simulations are set up similarly to those described in [44], with a diffusive hemispherical light source that is much larger than the dimensions of the concentrators imitating an isotropic celestial background, with the entrance surface of the DTIRCs placed near the origin of the hemisphere. In terms of power, the conventional DTIRC receives 1.91 times the power while the improved design receives 1.93 times the power that can be otherwise collected by a receiving area identical to the bottom plane of the DTIRCs (i.e., a static solar cell). Typically, the diffuse background light component on a clear day can make up 10% of the total solar radiation received by a horizontal surface. This percentage is also implied by the difference between the total power in the AM1.5 global horizontal irradiance and the AM1.5 direct normal irradiance spectra. This amount of diffuse solar power could be significantly higher under inclement weather conditions. Hence, we have shown that the improved DTIRC design offers advantages over a comparable conventional design for both direct and diffusive solar radiation collection.

5.2.2 Conclusion

We proposed an improved DTIRC design by inserting an optical path length difference between the upper and lower portion of the sidewall profiles, paired with a sharp turning point on the top entrance surface. By choosing a proper shape for the top surface and tuning the associated ΔOPL, the upper portion of the DTIRC structure can be expanded to result in a larger concentration ratio, while still allowing collection of rays at the original design acceptance angle. Interpolation is used to smooth the intermediate sidewall segment, allowing us to maintain collection efficiency for rays with angles of incidence in the middle of the acceptance range. Due to the enlarged entrance surface dimensions, the structure nominally overcomes the conventional limit imposed by *etendue* conservation, and can simultaneously achieve a higher concentration factor and acceptance angle compared to the best performing conventional DTIRC with a flat top surface.

It is worth noting that although the improvements in our new DTIRC design may appear marginal, due to efficiency loss arising from the interpolated sidewall segments, a more complex or hand-tuned interpolation process is likely to provide a smoother transition and even smaller curvature change, leading to better results than we can achieve with generic interpolation algorithms. We note, however, that the efficiency loss is also a fundamental consequence of the law of total *etendue* conservation, which applies not only to the extreme rays (rays incident at θ_A, in our case), but also to the collection of rays from all directions. Therefore, an increase in the input *etendue* from larger acceptance angles leads to a "leakage" penalty for rays at intermediate acceptance angles which are detected to a larger receiving area, so as to compensate for the output *etendue*, given that the rays from angles near θ_A are still contained within the bottom surface area. This is the reason that we refer to the limit exceeded by our new design as the "nominal *etendue* conservation" as opposed to "total *etendue* conservation."

Nonetheless, we have shown that, due to their higher concentration of nearly vertical rays, as well as an extended acceptance angle range, the new designs incorporating a conical top and ΔOPL on the sidewalls are indeed capable of delivering more annual collectible solar power than the comparable conventional designs, in the absence of any tracking system. Our new designs also out-perform conventional DTIRCs in collecting fully diffuse solar power. Our modified DTIRCs are therefore a promising enabling technology for the deployment of high-efficiency small-area solar cells for power generation in the practical circumstances found throughout the world outside of the tropics, where the majority of Earth's population lives.

References

[1]Y. Lin, G. Ung, B. Qiu, G. Qian, and S. M. Thon, “Integrated Concentrators for Scalable High-Power Generation from Colloidal Quantum Dot Solar Cells,” ACS Applied Energy Materials **1**, 2592–2599 (2018).

[2]M. Yuan, M. Liu, and E. H. Sargent, “Colloidal quantum dot solids for solution-processed solar cells,” Nature Energy **1**, nenergy201616 (2016).

[3]C. R. Kagan, E. Lifshitz, E. H. Sargent, and D. V. Talapin, “Building devices from colloidal quantum dots,” Science **353**, `10.1126/science.aac5523` (2016).

[4]G. H. Carey, A. L. Abdelhady, Z. Ning, S. M. Thon, O. M. Bakr, and E. H. Sargent, “Colloidal Quantum Dot Solar Cells,” Chemical Reviews **115**, 12732–12763 (2015).

[5]Y. Cheng, E. S. Arinze, N. Palmquist, and S. M. Thon, “Advancing colloidal quantum dot photovoltaic technology,” Nanophotonics **5**, 31–54 (2016).

[6]R. Wang, Y. Shang, P. Kanjanaboos, W. Zhou, Z. Ning, and E. H. Sargent, “Colloidal quantum dot ligand engineering for high performance solar cells,” Energy & Environmental Science **9**, 1130–1143 (2016).

[7]Y. Cao, A. Stavrinadis, T. Lasanta, D. So, and G. Konstantatos, “The role of surface passivation for efficient and photostable PbS quantum dot solar cells,” Nature Energy **1**, nenergy201635 (2016).

[8] R. Azmi, S.-H. Oh, and S.-Y. Jang, "High-Efficiency Colloidal Quantum Dot Photovoltaic Devices Using Chemically Modified Heterojunctions," ACS Energy Letters **1**, 100–106 (2016).

[9] T. Zhao, E. D. Goodwin, J. Guo, H. Wang, B. T. Diroll, C. B. Murray, and C. R. Kagan, "Advanced Architecture for Colloidal PbS Quantum Dot Solar Cells Exploiting a CdSe Quantum Dot Buffer Layer," ACS Nano **10**, 9267–9273 (2016).

[10] G.-H. Kim, F. P. García de Arquer, Y. J. Yoon, X. Lan, M. Liu, O. Voznyy, Z. Yang, F. Fan, A. H. Ip, P. Kanjanaboos, S. Hoogland, J. Y. Kim, and E. H. Sargent, "High-Efficiency Colloidal Quantum Dot Photovoltaics via Robust Self-Assembled Monolayers," Nano Letters **15**, 7691–7696 (2015).

[11] K. W. Kemp, A. J. Labelle, S. M. Thon, A. H. Ip, I. J. Kramer, S. Hoogland, and E. H. Sargent, "Interface Recombination in Depleted Heterojunction Photovoltaics based on Colloidal Quantum Dots," Advanced Energy Materials **3**, 917–922 (2013).

[12] M. Liu, F. P. G. de Arquer, Y. Li, X. Lan, G.-H. Kim, O. Voznyy, L. K. Jagadamma, A. S. Abbas, S. Hoogland, Z. Lu, J. Y. Kim, A. Amassian, and E. H. Sargent, "Double-Sided Junctions Enable High-Performance Colloidal-Quantum-Dot Photovoltaics," Advanced Materials **28**, 4142–4148 (2016).

[13] M. Liu, O. Voznyy, R. Sabatini, F. P. García de Arquer, R. Munir, A. H. Balawi, X. Lan, F. Fan, G. Walters, A. R. Kirmani, S. Hoogland, F. Laquai, A. Amassian, and E. H. Sargent, "Hybrid organic-inorganic inks flatten the energy landscape in colloidal quantum dot solids," Nature Materials **16**, 258–263 (2017).

[14] I. J. Kramer, G. Moreno-Bautista, J. C. Minor, D. Kopilovic, and E. H. Sargent, "Colloidal quantum dot solar cells on curved and flexible substrates," Applied Physics Letters **105**, 163902 (2014).

[15] X. Zhang, J. Zhang, J. Liu, and E. M. J. Johansson, "Solution processed flexible and bending durable heterojunction colloidal quantum dot solar cell," Nanoscale **7**, 11520–11524 (2015).

[16] X. Lan, O. Voznyy, A. Kiani, F. P. G. de Arquer, A. S. Abbas, G.-H. Kim, M. Liu, Z. Yang, G. Walters, J. Xu, M. Yuan, Z. Ning, F. Fan, P. Kanjanaboos, I. Kramer, D. Zhitomirsky, P. Lee, A. Perelgut, S. Hoogland, and E. H. Sargent, "Passivation Using Molecular Halides Increases Quantum Dot Solar Cell Performance," Advanced Materials **28**, 299–304 (2016).

[17] C.-H. M. Chuang, P. R. Brown, V. Bulović, and M. G. Bawendi, "Improved performance and stability in quantum dot solar cells through band alignment engineering," Nature Materials **13**, 796–801 (2014).

[18] M. Liu, O. Voznyy, R. Sabatini, F. P. García de Arquer, R. Munir, A. H. Balawi, X. Lan, F. Fan, G. Walters, A. R. Kirmani, S. Hoogland, F. Laquai, A. Amassian, and E. H. Sargent, "Hybrid organic–inorganic inks flatten the energy landscape in colloidal quantum dot solids," Nature Materials **16**, 258–263 (2017).

[19] F. Muhammad-sukki, R. Ramirez-iniguez, S. G. Mcmeekin, B. G. Stewart, B. Clive, F. Muhammad-sukki, R. Ramirez-iniguez, S. G. Mcmeekin, B. G. Stewart, and B. Clive, *Solar Concentrators* ().

[20] T. Cooper, G. Ambrosetti, A. Pedretti, and A. Steinfeld, "Theory and design of line-to-point focus solar concentrators with tracking secondary optics," Applied Optics **52**, 8586–8616 (2013).

[21] R. Bitterli, T. Scharf, and F. J. Haug, "Miniaturized concentrator arrays as compact angle transformers for light collection and distribution," in , Vol. 8620 (2013), pp. 86201X-86201X–12.

[22] Slade A and Garboushian V, "27.6% Efficient Silicon Concentrator Cell for Mass Production.," in (Oct. 2005).

[23] F. Dimroth, T. N. D. Tibbits, P. Beutel, C. Karcher, E. Oliva, G. Siefer, M. Schachtner, A. Wekkeli, M. Steiner, M. Wiesenfarth, A. W. Bett, R. Krause, E. Gerster, M. Piccin, N. Blanc, M. M. Rico, C. Drazek, E. Guiot, J. Wasselin, C. Arena, T. Salvetat, A. Tauzin, T. Signamarcheix, and T. Hannappel, "Development of high efficiency wafer bonded 4-junction solar cells for concentrator photovoltaic applications," in 2014 IEEE 40th Photovoltaic Specialist Conference (PVSC) (June 2014), pp. 0006–0010.

[24] Antonio L. Luque Viacheslav M. Andreev, "Concentrator Optics," in *Concentrator Photovoltaics*, edited by William T. Rhodes (Springer), pp. 113–132.

[25] Y.-K. Fuh and Z.-H. Lai, "A fast processing route of aspheric polydimethylsiloxane lenses array (APLA) and optical characterization for smartphone microscopy," Optics Communications **385**, 160–166 (2017).

[26] M. Zaboub, A. Guessoum, N.-E. Demagh, and A. Guermat, "Fabrication of polymer microlenses on single mode optical fibers for light coupling," Optics Communications **366**, 122–126 (2016).

[27] S. Möller and S. R. Forrest, "Improved light out-coupling in organic light emitting diodes employing ordered microlens arrays," Journal of Applied Physics **91**, 3324–3327 (2002).

[28] K. Tvingstedt, S. D. Zilio, O. Inganäs, and M. Tormen, "Trapping light with micro lenses in thin film organic photovoltaic cells," Optics Express **16**, 21608–21615 (2008).

[29] L. van Dijk, E. A. P. Marcus, A. J. Oostra, R. E. I. Schropp, and M. Di Vece, "3D-printed concentrator arrays for external light trapping on thin film solar cells," Solar Energy Materials and Solar Cells **139**, 19–26 (2015).

[30] N. Hayashi, D. Inoue, M. Matsumoto, A. Matsushita, H. Higuchi, Y. Aya, and T. Nakagawa, "High-efficiency thin and compact concentrator photovoltaics with micro-solar cells directly attached to a lens array," Optics Express **23**, A594–A603 (2015).

[31] H. Arase, A. Matsushita, A. Itou, T. Asano, N. Hayashi, D. Inoue, R. Futakuchi, K. Inoue, T. Nakagawa, M. Yamamoto, E. Fujii, Y. Anda, H. Ishida, T. Ueda, O. Fidaner, M. Wiemer, and D. Ueda, "A Novel Thin Concentrator Photovoltaic With Microsolar Cells Directly Attached to a Lens Array," IEEE Journal of Photovoltaics **4**, 709–712 (2014).

[32] C. Meichner, A. E. Schedl, C. Neuber, K. Kreger, H.-W. Schmidt, and L. Kador, "Refractive-index determination of solids from first- and second-order critical diffraction angles of periodic surface patterns," AIP Advances **5**, 087135 (2015).

[33] M. Querry, *Optical Constants of Minerals and Other Materials from the Millimeter to the Ultraviolet*, CRDEC-CR-88009 (CHEMICAL RESEARCH DEVELOPMENT AND ENGINEERING CENTER ABERDEEN PROVING GROUNDMD, CHEMICAL RESEARCH DEVELOPMENT AND ENGINEERING CENTER ABERDEEN PROVING GROUNDMD, Nov. 1987).

[34] B. S. Mashford, M. Stevenson, Z. Popovic, C. Hamilton, Z. Zhou, C. Breen, J. Steckel, V. Bulovic, M. Bawendi, S. Coe-Sullivan, and P. T. Kazlas, "High-efficiency quantum-dot light-emitting devices with enhanced charge injection," Nature Photonics **7**, 407–412 (2013).

[35] P. Chiu, D. Law, R. Woo, S. Singer, D. Bhusari, W. Hong, A. Zakaria, J. Boisvert, S. Mesropian, R. King, and N. Karam, "35.8% space and 38.8% terrestrial 5J direct bonded cells," in 2014 IEEE 40th Photovoltaic Specialist Conference (PVSC) (June 2014), pp. 0011–0013.

[36] M. A. Green, E. D. Dunlop, J. Hohl-Ebinger, M. Yoshita, N. Kopidakis, and A. W. Y. Ho-Baillie, "Solar cell efficiency tables (Version 55)," Progress in Photovoltaics: Research and Applications **28**, 3–15 (2020).

[37] J. F. Geisz, M. A. Steiner, N. Jain, K. L. Schulte, R. M. France, W. E. McMahon, E. E. Perl, and D. J. Friedman, "Building a Six-Junction Inverted Metamorphic Concentrator Solar Cell," IEEE Journal of Photovoltaics **8**, 626–632 (2018).

[38] X. Ning, R. Winston, and J. O'Gallagher, "Dielectric totally internally reflecting concentrators," Applied Optics **26**, 300–305 (1987).

[39] O. Cruz-Silva, O. Jaramillo, and M. Borunda, "Full analytical formulation for Dielectric Totally Internally Reflecting Concentrators designs and solar applications," Renewable Energy **101**, 804–815 (2017).

[40] "Concentrator Optics," in *Concentrator Photovoltaics*, edited by A. L. Luque and A. Viacheslav, Springer Series in Optical Sciences (Springer, Berlin, Heidelberg, 2007), pp. 113–132.

[41] R. Winston, J. C. Miñano, and P. Benítez, "4 - NONIMAGING OPTICAL SYSTEMS," in *Nonimaging Optics*, edited by R. Winston, J. C. Miñano, and P. Benítez (Academic Press, Burlington, Jan. 1, 2005), pp. 43–68.

[42] F. Muhammad-Sukki, S. H. Abu-Bakar, R. Ramirez-Iniguez, S. G. McMeekin, B. G. Stewart, A. B. Munir, S. H. Mohd Yasin, and R. Abdul Rahim, "Performance analysis of a mirror symmetrical dielectric totally internally reflecting concentrator for building integrated photovoltaic systems," Applied Energy **111**, 288–299 (2013).

[43] F. Muhammad-Sukki, S. H. Abu-Bakar, R. Ramirez-Iniguez, S. G. McMeekin, B. G. Stewart, N. Sarmah, T. K. Mallick, A. B. Munir, S. H. Mohd Yasin, and R. Abdul Rahim, "Mirror symmetrical dielectric totally internally reflecting concentrator for building integrated photovoltaic systems," Applied Energy **113**, 32–40 (2014).

[44] D. Freier, F. Muhammad-Sukki, S. H. Abu-Bakar, R. Ramirez-Iniguez, A. Abubakar Mas'ud, R. Albarracín, J. A. Ardila-Rey, A. B. Munir, S. H. Mohd Yasin, and N. A. Bani, "Software simulation and experimental characterisation of a rotationally asymmetrical concentrator under direct and diffuse solar radiation," Energy Conversion and Management **122**, 223–238 (2016).

Chapter 6

Summary and Outlook

This thesis focuses on providing ideas and strategies to address some of the challenges in the field of nano-material based thin film optoelectronics, specifically for renewable energy harvesting and light detection. Our discussion is primarily based on devices made with PbS colloidal quantum dots, due to their appealing properties such as band-gap tuning as well as their potential for economically scalable processing and production. Nonetheless, most of the methods and solutions proposed in the thesis have wide applicability to related materials, such as organic semiconductors and hybrid perovskites, and can potentially be adapted to other optoelectronic technologies such as light-emission devices and lasers.

In Chapter 2, we proposed strategies to enhance the functionalities of thin film photovoltaics based on a systematic study and optimization of multi- layer interference effects, as well as the idea to utilize photonic band structures in patterned optoelectronic thin films to realize simultaneous tuning of different optical spectrum components. The methods are of particular interest for applications relying on absorption and photogeneration. They could also potentially benefit other processes such as the tuning of density-of-states and input/output light-coupling which are critical for lasers and LEDs.

Next, we proposed and demonstrated the capabilities of a novel 2D multi-modal optoelectronic microscopy system. The system can provide large amounts of data based on parallel measurements of multiple device properties for thin-film optoelectronic devices. We analyzed initial data sets to elucidate the connections between multiple physical properties of PbS QD photovoltaics. Due to the versatility of the system, there are still many more capabilities left to explore. We hope to gather more insights and findings that can only be accessed with an intercorrelated multi-dimensional perspective afforded to us by this novel measurement system.

We also worked on extending the adaptability and functionality of solar concentrators used for thin film solar cells. We made improvements in concentrator optical designs to allow for more compactness, better economy and better performance in terms of the combination of the concentration factor and wide-angle acceptance. We optimized concentrator designs for specific application and circumstances, using methodologies applicable to a wide range of scenarios. Some variants of these concentrator designs are playing an important role in illumination optics, which have spurred advances in modern optoelectronic-based solid state lighting and display technologies. We plan to extend our experience and findings to these areas as well.

The field of optoelectronics has been constantly incorporating the most advanced achievements from all major fields of science, allowing it to develop a non-stop flow of innovations that keep changing the world. The aim of the work described in this thesis is to contribute to one of the greatest technological journeys of this era.

Appendix A

Experimental Methods

A.1 PbS CQD Synthesis and PbI_2 Passivation

PbS CQD were synthesized based on literatures mentioned in 2.2. The materials used were lead oxide (PbO), bis(trimethylsilyl) sulphide (TMS), oleic acid(OA), 1-octadecene (ODE) purchased from suppliers including Alfa Aesar, Millipore Aldrich, Fischer Science, etc. ODE was firstly prepared in large amounts by degassing under vacuum at 80 °C for 16 h using the Schlenk line, which could be then used for 8+ batches of syntheses. For each batch,aA Pb oleate stock solution was prepared by mixing one unite of oleic acid (1.5 ml), PbO (0.45 g), and ODE (3 ml) in a flask connected to the Schlenk line, which are then heated to ∼105 °C under vacuum for 16 h. After this, 15 ml of ODE was injected to the stock solution, and the mixture was stirred, and heated to 120°C under the N^2 flow, during which time the TMS/ODE precursor was prepared by adding 210 µl of TMS into 10 ml of ODE inside a inert atmosphere glovebox. The TMS/ODE mixture was then injected into the reaction flask when the desired temperature was stabilized. Immediately after injection, the heating equipment was quickly removed and the flask was allowed to cool gradually to ∼36 °C. The mixture containing the PbS CQDs were then precipitated with sufficient amount of distilled acetone and centrifuged. After discarding the supernatant, the precipitate was re-dispersed in toluene and precipitated again with acetone, centrifuged, dried, and finally dispersed in toluene at a concentration ~50 mg ml^{-1}.

For each synthesis, all chemicals can be used in double or triple units to allow for more efficient production. The yield was usually >90 % regardless of the number of units of the chemicals. For CQDs of different sizes, the ratio of OA to Pb and the injection temperature were adjusted according to literatures in 2.2.

The toluene-dispersed PbS CQDs were stored in the glove box before ligand-exchange and treatment. For PbI_2 solution-phase ligand exchange, PbI_2 (0.1M), $PbBr_2$ (0.02M) and NH_4Ac (0.04 M) were fully dissolved in dimethylformamide (DMF). 5 ml of CQD in octane solution (10 mg ml^{-1}) was added to the equi-volume DMF solution and was then vigorously agitated to ensure the complete phase transfer. The DMF solution was washed three times with octane and was then precipitated via the addition of toluene. The mixture were separated by centrifugation. After drying,the CQDs were re-dispersed in butylamine(230 mg ml^{-1}). The CQD films were deposited by spinning the solution at 2500 rpm onto the substrates and was then transferred to the glove box for annealing at 70 °C for 20 min.

A.2 Synthesis of ZnO Nanoparticles and Deposition of the Oxide Film

The ZnO nanoparticle solution was synthesized following the methods widely used in reports of PbS CQD Devices[1]. Zinc acetate dihydrate ($Zn(OAc)_2$ 3.00 g, 13.7 mmol) was added to 2-methoxyethanol (200 ml) and dissolved completely. In a separate vial, Tetramethylammonium hydroxide (TMAH, 4.5 g, 25 mmol) and 2-methoxyethanol (20 ml) were combined. Under constant stirring, the methoxyethanol solution was kept at 60 °C, while the TMAH solution added to it dropwisely over 10 min. The solution was allowed to stir for an additional 2 h. After this, 2-ethanolamine (4 ml) was added to stabilize the particles.

Each 10 ml of ZnO nanocrystals solutions were purified by adding toluene (20 ml) and hexane (10 ml) to precipitate the nanoparticles, followed by centrifugation. After decanting the colorless supernatant, the powder was re-dispersed in a mixture of 2-isopropanol (2 ml) and methanol (1 ml). Both the unpurified ZnO solution and the purified dispersion were stored at $-30\,^{\circ}\mathrm{C}$.

Alternative methods were also used when desired, which were primarily based on the same or similar precursors with different solvents and anti- solvent. In most variants, the molar-ratio of Zn:OH was kept close to 1.75 for optimal yield and quality[2]. For example[3], in many cases the solvent for $Zn(OAc)_2$ is replaced by methanol, and KOH dissolved also in methanol is used as the base precursor. The mixture is centrifuged without adding anti-solvent, and was re-dispersed in chloroform or a mixture of methanol and chloroform.

The TCO substrates were thoroughly cleaned in saturated NaOH solution, acetone and isopropanol inside an ultrasonic cleaner before deposition of ZnO film. The ZnO solution was usually adjusted to a concentration of $\sim 20\,\mathrm{mg\,ml^{-1}}$ and was filtered through 0.25 µm syringe filter. The ZnO film was formed by spin coating the ZnO solution onto the TCO substrates at ~1500 rpm. It was also found that the acceleration can have a great impact on the performance of the final device, so an acceleration of 6000 to 11 000 rpm/s was usually used.

Appendix B

Computation and Optimization Methods

B.1 Transfer-Matrix-Method for Multi-Colored Thin Film Solar Cells

In Matlab, GPU computation can be incorporated by converting matrix data to `gpuarray` and in Matlab to improve the speed.

```
function output= ObjectivePbI2_Au(x)
n=load('materials_nk.mat').n;
% load the refractive index data of all layers
t = [0 x(1) x(2) x(3) x(4) x(5)];
tic
% thickness of each corresponding layer in nm thickness of the first layer is irrelivant)
lambda=300:1200;
% Wavelengths over which field patterns are calculated
h=6.626e-34; % Js Planck's constant
c=2.998e8; %m/s speed of light
q=1.602e-19; %C electric charge

output=struct();
% Calculate Incoherent power transmission through the glass substrate
R_glass=abs((1-n(1,:))./(1+n(1,:))).^2;
T_glass=abs(4*1*n(1,:)./(1+n(1,:)).^2);
t_cumsum=(cumsum(t)); %create thickness coordinates array

```

```
thickness=sum(t);
x_pos=((1/2):1:thickness);%positions to evaluate field
E=zeros(length(x_pos),length(lambda));
x_mat= (sum(repmat(x_pos,length(t),1)>repmat(t_cumsum',1,length(x_pos)),1)+1);
%x_mat specifies what layer number the corresponding point in x_pos is in:
%Initialize 2x2 transfer matrix element for each wavelength (2x2x#wavelength)
S11=(ones(1,length(lambda)));
S12=(zeros(1,length(lambda)));
S21=S12;
S22=S11;
S11p=S11;
S12p=S12;
S21p=S21;
S22p=S22;
for m=2:length(t)
    tr=2*n(m-1,:)./(n(m-1,:)+n(m,:));%Fresnel coefficients from left to right
    r=(n(m-1,:)-n(m,:))./(n(m-1,:)+n(m,:));
    A11=S11.*(1./tr)+S12.*(r./tr); %2x2matrix multiplication
    A12=S11.*(r./tr)+S12.*(1./tr);
    A21=S21.*(1./tr)+S22.*(r./tr);
    A22=S21.*(r./tr)+S22.*(1./tr);
    L11=exp(-1i*2*pi*n(m,:)./lambda*t(m)); %propagation matrix, diagonal
    L22=exp(1i*2*pi*n(m,:)./lambda*t(m));
    S11=A11.*L11; %matrix multiplication
    S12=A12.*L22;
    S21=A21.*L11;
    S22=A22.*L22;
    if m==length(t) %Last layer in contact with air
        tr=2*n(m,:)./(n(m,:)+1);
        r=(n(m,:)-1)./(n(m-1,:)+1);
        S11=S11.*(1./tr)+S12.*(r./tr);
        S12=S11.*(r./tr)+S12.*(1./tr);
        S21=S21.*(1./tr)+S22.*(r./tr);
        S22=S21.*(r./tr)+S22.*(1./tr);
    end
    j=length(t)-m+3;
    %Fresnel coefficients from the reverse direction
    if j>length(t)
        rp=(n(j-1,:)-1)./(n(j-1,:)+1);
        trp=1+rp;
    else
        rp=(n(j-1,:)-n(j,:))./(n(j-1,:)+n(j,:));
        trp=1+rp;
    end
    %Backpropagate the matrix multiplication
    A11p=S11p.*(1./trp)+S21p.*(rp./trp);
    A12p=S22p.*(rp./trp)+S12p.*(1./trp);
    A21p=S21p.*(1./trp)+S11p.*(rp./trp);
    A22p=S12p.*(rp./trp)+S22p.*(1./trp);
```

```
    k=2*pi*n(j-1,:)./lambda;
    L11p=exp(-1i*k*t(j-1));
    L22p=exp(1i*k*t(j-1));
    S11p=A11p.*L11p;
    S12p=A12p.*L11p;
    S21p=A21p.*L22p;
    S22p=A22p.*L22p;
    if j>2
        %Calculate electric field at each position
        indices= x_mat==j-1;
        x=((x_pos(indices)-t_cumsum(j-2)))';
        E(indices,:)=repmat(A11p,length(x),1).*exp(1i*(x-t(j-1))*k)+repmat(A21p,length(x),1).*exp(1i*(t(j-1)-x)*k);
    end
end
reff=S21./S11;  %r and t coefficients excluding the glass substrate.
R=abs(reff).^2;
teff=1./S11;
tTot=2./(1+n(1,:))./sqrt(1-R_glass.*R).*teff; %transimission amplitude through all layers.
E=E.*repmat(tTot,length(x_pos),1);
output.field=E;
% Absorption coefficient
a=4*pi*imag(n)./repmat(lambda*1e-7,length(t),1);
Absorptivity=zeros(length(t),length(lambda));
%The absorptivity (Percentage of light absorbed) of each layer.
AbsProb=zeros(thickness,length(lambda));
%The probability of absorption (generation) absorbed per unit length (#/nm)
for matindex=2:length(t)
    Pos=x_mat == matindex;
    AbsProb(Pos,:)=repmat(a(matindex,:).*real(n(matindex,:)),sum(Pos),1).*(abs(E(Pos,:)).^2);
    Absorptivity(matindex,:)=sum(AbsRate,1)*1e-7; %Absorptivity from each layer - dimensionless
end
output.AbsProb=AbsProb;
output.Absorptivity=Absorptivity;
% Load in 1sun AM 1.5 solar spectrum in mW/cm2nm
AM15_data= load('AM15.dat').n;
AM15=interp1(AM15_data(:,1), AM15_data(:,2), lambda, 'linear', 'extrap');
ActivePos=(x_mat ==4|(x_mat==5)); %Choose the active layer
AM15ph=1e-3*AM15.*lambda/(h*c)*1e-9; %AM1.5 Photon flux spectral density #/(sec*cm^2*nm);
%Generation rate spectral density #/(sec*cm^3*nm)
Gen=AbsProb(ActivePos,:).*repmat(AM15ph,sum(ActivePos),1);
output.GenDensity=Gen;
GenX=sum(Gen,2); %Gneration rate profile #/(sec*cm^3)
output.GenProfile=GenX;
Reflection=R_glass+T_glass.^2.*R./(1-R_glass.*R);
output.Reflection=Reflection;
output.Jsc=-sum(GenX)*1*1e-7*q*1e3; %in mA/cm^2
%To optimize RGB
```

```
xyz_5=load('xyzMatrices.mat');
AM15=load('AM15.dat').n;
RefSpec = Reflection(1,91:441);
RefSpec_5=RefSpec(1:5:351)'; % At 5 nm intervals
AM15_5=AM15(1:5:351);
LumSpec=RefSpec_5.*AM15_5; %The reflected solar spectrum
XYZ= xyz_5'*AM15_5; %XYZ trimulus of the reflected spectrum.
xyz=XYZ/sum(XYZ);
output.Chromacity=xyz;
```

B.2 Fourier-Modal Method for Solving the Transmission Coefficients of 2D Photonic Crystal Slab

GPU computation can be enabled by storing most of the matrices using `gpuarray`. Intermediate arrays with excessive large sizes were cleared frequently inside the function to free up the graphics card memory, which was necessary for calculation with a large order of Fourier series

```
function [ita_T,ita_R,T_Total,R_Total,T00,R00]=SlabEigenModesF_TinaEdit(M,alpha0,beta0,lambda0,h,r,phi)
%M=Fourier Series nuber
%alpha0=AOI on x axis
%beta0=AOI on y axis
%lambda0 = wavelength, normalized by a
%h=slab height
%r=radius of lattice, normalized by a
%phi==Lattice type (pi/6 = hexagonal, pi/4 = square)

N=M; %the number of Fourier series ... resolutioun from diffraction order
k0=2*pi/(lambda0); %wave vector in vacuum
mu=1; % permeability (Gaussian Unit)
x=0:0.005:1;
y=x;
Ngrid=length(x)*length(y);
[xx,yy]=meshgrid(x,y);%define the real space grid
yyp=yy*cos(phi); %define the oblique coordinates
xxp=xx+yy*sin(phi);
idx_middle=floor(length(x)/2)+1;
yp_center=cos(phi)/2;
ay=2*yp_center;
%Create the 2D epsilon profile with a predefined hole (or cylinder) and
%make sure it extends correctly from nearby unit cells
```

```
epsilon=((xxp-0.75).^2+(yyp-yp_center).^2<r^2)*(13)+((xxp-0.75).^2+(yyp-yp_center).^2>=r^2)*(1);
epsilon((xxp+0.25).^2+(yyp-yp_center).^2<r^2)=1;
epsilon((xxp-1.75).^2+(yyp-yp_center).^2<r^2)=1;
epsilon((xxp-0.25).^2+(yyp-yp_center+ay).^2<r^2)=1;
epsilon((xxp-1.25).^2+(yyp-yp_center-ay).^2<r^2)=1;
epsilonF=fftshift(fft2(epsilon))/Ngrid; %Fourier series coefficients of the 2D epsilon.
epsilonInvF=fftshift(fft2(1./epsilon))/Ngrid;%Fourier series coefficients of the inverse of epsilon
aMax=(2*M+1)*(2*N+1);
alpha=alpha0+(-M:M)*2*pi;
beta=beta0+(-N:N)*2*pi;  %generating all in-plan k vectors (alpha in x, beta in y)
%a and b are normalized length scale vectors within a unit cell modulated
epsilonF_ab=zeros(aMax); %Initialie empty matrices
epsilonInvF_ab=zeros(aMax);
alpha_ab=zeros(aMax);
beta_ab=zeros(aMax);
epsilonInvF_ab_vector=zeros(aMax,1); %vectorize the Fourier coefficients matrices with linear indexing
epsilonF_ab_vector=zeros(aMax,1);
disp('initializing finished');
fprintf('Calculating Matrices..\n');
checkTopilatz=zeros(aMax);

%Fourier transfrom of the inverse of epsilon on the y-axis only
epsilonInvFy=fftshift(fft(1./epsilon),1)/length(epsilon);
% x-axis only
epsilonInvFx=fftshift(fft(1./epsilon,length(x),2),2)/length(epsilon);
% 3-D matrices for intermediate convolution ((2M+1)*(2N+1)*l)
epsilonInvFy_M=zeros(2*M+1,2*N+1,size(epsilonInvFy,1));
epsilonInvFx_M=epsilonInvFy_M;
epsilonInvFy_MInv=zeros(2*M+1,2*N+1,size(epsilonInvFy,1));
epsilonInvFx_MInv=epsilonInvFx_M;
for m=-M:M
    %Load Fourier coefficients of x-only (or y) transforms into 'M' matrices
    for n=-N:N
        epsilonInvFy_M(m+M+1,n+N+1,:)=epsilonInvFy(m-n+idx_middle,:);
        epsilonInvFx_M(m+M+1,n+N+1,:)=epsilonInvFx(:,m-n+idx_middle);
    end
end
for l=1:length(epsilon)
    %2D matrix inverse to create 'MInv' matrices from 'M'
    epsilonInvFy_MInv(:,:,l)=epsilonInvFy_M(:,:,l)^(-1);
    epsilonInvFx_MInv(:,:,l)=epsilonInvFx_M(:,:,l)^(-1);
end
%Fourier transform the remaining axes of M matrices
epsilonInvFy_MInv_Fx=fftshift(fft(epsilonInvFy_MInv,length(x),3)/length(x),3);
epsilonInvFx_MInv_Fy=fftshift(fft(epsilonInvFx_MInv,length(x),3)/length(x),3);
```

```
%Initializing final matrices with (a,b) indexing.
epsilonInvFy_MInv_Fx_ab=zeros(aMax);
epsilonInvFx_MInv_Fy_ab=zeros(aMax);
for a=1:aMax   %Generating the Fourier series of epsilon and epsilon^-1 with a and b indexing.
    %(na,ma) correspond to zero-centered a index
    na=floor((a-1)/(2*M+1))-N;
    ma=mod((a-1),(2*M+1))-M;
    %fill the vectoized Fourier coefficients of epsilon (and its inverse)
    epsilonInvF_ab_vector(a)=epsilonInvF(na+idx_middle,ma+idx_middle);
    epsilonF_ab_vector(a)=epsilonF(na+idx_middle,ma+idx_middle);
    for b=1:aMax
        %(nb,mb) correspond to zero-centered b index
        nb=floor((b-1)/(2*M+1))-N;
        mb=mod((b-1),(2*M+1))-M;
        checkTopilatz(a,b)=na-nb;
        %fill the a,b indexed Fourier coefficients of epsilon (and its inverse)
        epsilonF_ab(a,b)=epsilonF(na-nb+idx_middle,ma-mb+idx_middle);
        epsilonInvF_ab(a,b)=epsilonInvF(na-nb+idx_middle,ma-mb+idx_middle);
        %fill the other set of imbalanced a-b indexed matrix
        epsilonInvFy_MInv_Fx_ab(a,b)=epsilonInvFy_MInv_Fx(na+N+1,nb+N+1,ma-mb+idx_middle);
        epsilonInvFx_MInv_Fy_ab(a,b)=epsilonInvFx_MInv_Fy(ma+M+1,mb+M+1,na-nb+idx_middle);
        %a,b indexed in-plane k vectors.
        alpha_ab(a,b)=alpha(ma+M+1)*(a==b);
        beta_ab(a,b)=beta(na+N+1)*(a==b);
    end
end

length_1u=aMax; %sizes of single block matrix
I_mono=eye(length_1u);
e_inv=epsilonF_ab^(-1);
aeb=alpha_ab*e_inv*beta_ab;
bea=aeb';
F11=aeb-mu*k0^2*sin(phi)*I_mono;
F12=mu*k0^2*I_mono-alpha_ab*e_inv*alpha_ab;
F21=beta_ab*e_inv*beta_ab-mu*k0^2*I_mono;
F22=mu*k0^2*sin(phi)*I_mono-bea;
F=[F11 F12; F21 F22]; %obtain F matrix
einv_inv=epsilonInvF_ab^(-1);
ab=alpha_ab*beta_ab;
a2=alpha_ab^2;
b2=beta_ab^2;
G11=mu*k0^2*sin(phi)*einv_inv-ab;
G12=a2-mu*k0^2*(cos(phi)^2*epsilonInvFy_MInv_Fx_ab+sin(phi)^2*einv_inv);
G21=mu*k0^2*(cos(phi)^2*epsilonInvFx_MInv_Fy_ab+sin(phi)^2*einv_inv)-b2;
G22=-G11;
G=[G11 G12; G21 G22]; %obtain G matrix
```

```
% F=gpuArray(F);
% G=gpuArray(G);
fprintf('matrices obtained\n');
fprintf('calculating eigenmodes\n');

[E,D]=eig(F*G);
gamma=(sqrt(D/(mu*k0^2*cos(phi)^2)));
%gamma(imag(gamma)<0)=-gamma(imag(gamma)<0); %<- dispersive?
gamma(real(gamma)+imag(gamma)<0)=-gamma(real(gamma)+imag(gamma)<0);
%Amplitudes of eigen fields.
H=1/(mu*k0*cos(phi))*G*E*gamma^(-1);
W2=[E E;H -H];
E3=eye(length(E));
G3=[k0^2*sin(phi)*I_mono-ab, a2-k0^2*I_mono;k0^2*I_mono-b2, -k0^2*sin(phi)*I_mono+ab];
gamma3_s=sqrt(k0^2*I_mono-1/cos(phi)^2*(a2+b2-2*ab*sin(phi)));
gamma3=[gamma3_s zeros(length(gamma3_s)); zeros(length(gamma3_s)) gamma3_s];
%Amplitudes of eigen fields.
H3=1/(cos(phi)*k0)*G3*E3*gamma3^(-1);
W3=[E3,E3;H3,-H3];
W1=W3;
fprintf('Eigenmodes obtained\n');
fprintf('Calculating S-matrix and coefficients\n');

T2=W3\W2; %this is inv(W3)*W2 where W3 is a more top layer than W2
clear F11 F12 F21 F22 G11 G12 G21 G22;
clear E H E3 H3 W3 F G G3 D gamma3;
[T2_11,T2_12,T2_21,T2_22]=quadsubmatrices(T2);
T2crit=T2_22^(-1);
Kappa=diag(exp(1i*diag(gamma)*h));
%Conversion from transfer matrix T to scattering matrix S
s2_tilde=[(T2_11-T2_12*T2crit*T2_21)*Kappa, T2_12*T2crit; -Kappa*T2crit*T2_21*Kappa, Kappa*T2crit];
clear gamma Kappa;
clear T2_11 T2_22 T2_21 T2_22 T2crit;
fprintf('s2 obtained\n');
fprintf('s2 tilde obtained\n');
T1=W2\W1;
[T1_11,T1_12,T1_21,T1_22]=quadsubmatrices(T1);
T1crit=T1_22^(-1);
s1=[T1_11-T1_12*T1crit*T1_21, T1_12*T1crit; -T1crit*T1_21, T1crit]; %S-matrix with 4 quadrants
clear T1_11 T1_12 T1_21 T1_22 T1crit;
clear W1 W2 T1;
fprintf('S1 obtained\n');
[ ~,Rud1,~,Tdd1]=quadsubmatrices(s1);
%only care about Rud1 and Tdd1 because they apply to light coming down on slab from topmost layer
[tuu2,rud2,rdu2,tdd2]=quadsubmatrices(s2_tilde);
clear s1 s2_tilde;
IS=eye(2*aMax);
M2=(IS-rdu2*Rud1)\tdd2;
```

```
Rud2=(rud2+tuu2*Rud1*M2); %% gives the reflection of waves coming down from top layer
Tdd2=(Tdd1*M2); %% gives the transmission of waves coming down from bottom layer
fprintf('S obtained\n');

%initialize the reflectance and transmittance for each m,n order
ita_R=zeros(M,N);
ita_T=zeros(M,N);
prop_range=zeros(M,N);
for a=1:aMax
    m=mod((a-1),(2*M+1))+1;
    n=floor((a-1)/(2*M+1))+1;
    E1R=Rud2(a,(2*M+1)*N+M+1);
    E2R=Rud2(aMax+a,(2*M+1)*N+M+1);
    E1T=Tdd2(a,(2*M+1)*N+M+1);
    E2T=Tdd2(aMax+a,(2*M+1)*M+M+1);
    prop_range(m,n)=isreal(gamma3_s(a,a)); %find the order with real propagation wave vectors
    beta=beta_ab(a,a);
    alpha=alpha_ab(a,a);
    ita_R(m,n)=1/gamma3_s(a,a)/k0*((k0^2-beta^2)*abs(E1R)^2+(k0^2-alpha^2)...
        *abs(E2R)^2+(alpha*beta-k0^2*sin(phi))*2*real(E1R*conj(E2R)));
    ita_T(m,n)=1/gamma3_s(a,a)/k0*((k0^2-beta^2)*abs(E1T)^2+(k0^2-alpha^2)...
        *abs(E2T)^2+(alpha*beta-k0^2*sin(phi))*2*real(E1T*conj(E2T)));
end
%Total reflectance or transmission of all orders
T_Total=sum(sum(ita_T.*prop_range));
R_Total=sum(sum(ita_R.*prop_range));
disp(T_Total);
disp(R_Total);
%reflectance or transmission of the center (zeroth) order
T00=ita_T(N+1,M+1);
R00=ita_R(N+1,M+1);

function [a11,a12,a21,a22]=quadsubmatrices(a)
    %divide a larger matrix into 2x2 sub block matrices
    NN=length(a);
    a11=a(1:NN/2,1:NN/2);
    a12=a(1:NN/2,NN/2+1:NN);
    a21=a(NN/2+1:NN,1:NN/2);
    a22=a(NN/2+1:NN,NN/2+1:NN);
end
end
```

B.3 Generation of 3D DTIRCs Profiles with Conical Top Surfaces

```
PC=[]; %The coordinates of the pointCloud to be generated.
dome_area=0; % The xy plane projected area of the top surface
x_top=[]; % top surface coordinates on the computation plane.
y_top=[];
n=1.41;
thetaa1=pi/7.2; % acceptance angle
pAngle=-pi/15; % ramp angle
d00=5.0; %
d0=d00;
d1=15; % attepted d1
thetaa=thetaa1;
Theta=asin(sin(thetaa1-pAngle)/n)+pAngle; %Vertical inclination of the
%extreme ray hitting the left corner of the top surface
H0=0.5*(d1+d0)*cot(Theta)+d1/2*tan(pAngle); %The height at the center,
%consistent for side profiles of all angles to form a continuous top ↩
    dome shape

%Solve for H and d1 from all the input parameters
func=@(x) DTIRCtrialParameters(n,d0,x(1),pAngle,thetaa1,x(2));
sol=fsolve(func,[d1,H0]);
d1=sol(1);
H0=sol(2);
H=0.5*(d1+d0)*cot(Theta);

%generate the x,y coordinates
[diff,points,idx]=DTIRCtrialParameters(n,d0,sol(1),pAngle,thetaa1,sol↩
    (2));
x=points{1}(:,1);
z=points{1}(:,2);
xp=points{2}(:,1);
zp=points{2}(:,2);
[X,XP]=meshgrid(x,xp); %find the intersection of 2 choices of segment ↩
    2
[Z,ZP]=meshgrid(z,zp);
D=(X-XP).^2+(Z-ZP).^2;
Dmin=min(min(D));
[~,t]=find(Dmin==D);
z0=z(t); % the intersection
%generate xf, zf final coordinates
xf=[(z>z0).*x+(z<=z0).*xp];
zf=[(z>z0).*z+(z<=z0).*zp];
% xfi=xf;
% zfi=zf;

%interpolation of the sidewall
zfi_upper=linspace(zf(idx),zf(end),260-idx+1);
xfi_upper=interp1(zf(idx:end),xf(idx:end),zfi_upper,'spline','extrap')↩
```

```
    ;
xfi=[xf(1:idx-1);xfi_upper'];
zfi=[zf(1:idx-1);zfi_upper'];

%side profile coordinates stored in surface matrix
x3d=xfi;
z3d=zfi;
y3d=zeros(1,length(x3d))';

%generate the top coordinates
xtop=linspace(0.02,xf(end),20)';
ytop=zeros(size(xtop,1),size(xtop,2));
xfztop=H0-sqrt(xtop.^2+ytop.^2)*tan(pAngle);

%Generate the side profiles for all azimuthal angles
for alpha=pi/4/16:pi/4/16:pi/2 %rotation angle
    d0=d00*sqrt(1+tan(alpha)^2); % exit aperture
    if(alpha>pi/4)
        d0=d00*sqrt(1+cot(alpha)^2);
    end
    func=@(x) DTIRCtrialParameters(n,d0,x(1),pAngle,x(2),H0);
    sol=fsolve(func,[d1,thetaa]);
    [diff,points,idx]=DTIRCtrialParameters(n,d0,sol(1),pAngle,sol(2),↩
       H0);
    fprintf('alpha=%f, d0=%f, \n.', alpha/pi*180,d0);
    d1=sol(1);
    thetaa=sol(2);
    x=points{1}(:,1);
    z=points{1}(:,2);
    xp=points{2}(:,1);
    zp=points{2}(:,2);
    [X,XP]=meshgrid(x,xp); %findin the intersection of 2 choices of ↩
       segment 2
    [Z,ZP]=meshgrid(z,zp);
    D=(X-XP).^2+(Z-ZP).^2;
    Dmin=min(min(D));
    [~,t]=find(Dmin==D,1);
    z0=z(t); % the intersection
    xf=(z>z0).*x+(z<=z0).*xp;
    zf=(z>z0).*z+(z<=z0).*zp;
%     xfi=xf;
%     zfi=zf;
    zfi_upper=linspace(zf(idx),zf(end),260-idx+1);
    xfi_upper=interp1(zf(idx:end),xf(idx:end),zfi_upper,'spline','↩
       extrap');
    xfi=[xf(1:idx-1);xfi_upper'];
    zfi=[zf(1:idx-1);zfi_upper'];
    x3d=[x3d,xfi*cos(alpha)];
    z3d=[z3d,zfi];
    y3d=[y3d,xfi*sin(alpha)];
    r_top=linspace(0.02,xf(end),20)';
    xtop_new=r_top*cos(alpha);
    ytop_new=r_top*sin(alpha);
    ztop_new=H0-sqrt(xtop_new.^2+ytop_new.^2)*tan(pAngle);
```

```
    xtop=[xtop,xtop_new];
    ytop=[ytop,ytop_new];
    ztop=[ztop,ztop_new];
end
%Organize the point cloud
x3d=[fliplr(x3d),x3d,fliplr(-x3d),-x3d];
y3d=[-fliplr(y3d),y3d,fliplr(y3d),-y3d];
z3d=[fliplr(z3d),z3d,fliplr(z3d),z3d];



%calculate concentration ratio
[S,~]=alphavol([reshape(xtop,[],1),reshape(ytop,[],1)],1,1);
C_ratio=4*S/d00^2;
%process the data for stl file conversion
P1=1:length(x3d)/2;
P2=(length(x3d)/2+1):length(x3d);
[F,V]=surf2patch(x3d,y3d,z3d,'triangles');
[F1,V1]=surf2patch(x3d(P1,:),y3d(P1,:),z3d(P1,:),'triangles');
[F2,V2]=surf2patch(x3d(P2,:),y3d(P2,:),z3d(P2,:),'triangles');

%The function to solve for a consistent set of parameters
function [diff,points,idx]=DTIRCtrialParameters(n,d0,d1,pAngle,thetaa,H0_trial)
Theta=asin(sin(thetaa-pAngle)/n)+pAngle; % maximum vertical ray angle
thetac=asin(1/n);  %critical angle of the material
theta0=pi-Theta-2*thetac;
%Angle of reflected ray from the extreme ray hitting the left corner of the top surface

xd=linspace(-d1/2,d1/2,160); %the locations of rays hitting the top plane
%the REAL locations of rays hitting the top surfaces.
xdpl=(xd+d1/2)/(1-tan(-pAngle)*tan(thetaa))-d1/2;
ydpl=-(xd+d1/2)*tan(-pAngle)/(1-tan(-pAngle)*tan(thetaa));
xdpr=d1/2-(d1/2-xd)/(1+tan(-pAngle)*tan(thetaa));
ydpr=-(d1/2-xd)*tan(-pAngle)/(1+tan(-pAngle)*tan(thetaa));
xdc=d1/2*tan(pAngle)*tan(thetaa);
%the location of the ray (in terms of xd) hitting exactly the center of the top surface
idx=sum(xd<xdc);
xdp=[xdpl(1:idx),xdpr(idx+1:end)];
ydp=[ydpl(1:idx),ydpr(idx+1:end)];

pA=sign(xdp)*(-pAngle);
thetap=asin(sin(thetaa-pA)/n)+pA;%Vertical inclination angles of all rays
l1=((xdp+d1/2)*tan(thetaa)-ydp)*cos(thetaa);
H=0.5*(d1+d0)*cot(Theta);
C=d1*sin(thetaa)+n*(d1+d0)/(2*sin(Theta));
%The total OPL: constant optical path for ray hitting the left corner (coming from left)
dC=-0.6; %OPL difference across the center of the top surface
deltaC=[dC*ones(1,idx),zeros(1,length(xd)-idx)];
```

```
%deltaC=flip(cumtrapz(d1/2-flip(xd),(n*flip(sin(thetap))-sin(thetaa)))↩
    );
C=deltaC+C;
a=(C-l1)/n;
b=xdp+d0/2;
c=H+ydp;
l2=(a.^2-b.^2-c.^2)./(2*(a+b.*sin(thetap)-c.*cos(thetap))); %segment 2↩
     for rays hitting the same point
x=xdp+l2.*sin(thetap);%Side profile coordinates generated from knowing↩
     l2;
y=H+ydp-l2.*cos(thetap);
l2=(a-b*sin(theta0)-c*cos(theta0))./(2*sin((theta0+thetap)/2).^2); %↩
    segment 2 for rays exiting parallelly
xp=xdp+l2.*sin(thetap);
yp=H+ydp-l2.*cos(thetap);
H0=H+d1/2*tan(pAngle);
d0_new=2*xp(1); %exiting aperture determined by the side profile, ↩
    should be equal to d0
diff(1)=d0-d0_new;
diff(2)=H0-H0_trial;
points={[x',y'],[xp',yp']};
end
```

Yida Lin | Curriculum Vitae

309 Parkin st. – Baltimore, Maryland 21230

☎ (607) 379 4663 • ✉ ylin89@jhu.edu

Education

The Johns Hopkins University
Ph.D in Electrical & Computer Engineering *2015–2020*

The Johns Hopkins University
M.Sci in Electrical & Computer Engineering *2015–2017*

Cornell University
M.Sci in Applied & Engineering Physics *2012–2014*

Peking University
B.Sci in Economics *2009–2012*

Peking University
B.Sci in Physics *2008–2012*

Experience

Research

THE JOHNS HOPKINS UNIVERSITY **Baltimore, MD**
Research Assistant *2015–Present*

Conducted research on semiconductor colloidal quantum dots (QDs) and related optoelectronic devices: solar cells, photodetectors, etc.; Optical engineering to enhance the performance and functionalities of the materials and devices.

- Devised and built Micron-resolution Multi-Modal Microscopy for thin film optoelectronics.
- Designed and optimized wide-angle and diffuse-light collectible concentrators for integrated photovoltaic systems.
- Lead Sulfide QD Optoelectronics Device Fabrication and Optimization.
- Proposed photonic crystal band engineering strategies for spectral selectivity in absorbing materials.
- Optimized and Fabricated multicolor QD solar cells via thin film optical interference control.

CORNELL UNIVERSITY **Ithaca, NY**

Research Assistant *2013–2014*

Optimization of Lead Salt QD Light-Emitting-Diodes.

- Fabricated QD LEDs with dual crystalline oxide charge transport layers.
- Conducted cryogenic experiments to reveal the relaxation and recombination dynamics in QD films.

PEKING UNIVERSITY **Beijing, China**

Undergraduate Research Assistant *2011-2012*

Studied Spin Hall Effect of Light (SHEL) on metallic and magnetic thin films.

Teaching

THE JOHNS HOPKINS UNIVERSITY

Teaching Assistant, ECE 520.627 – Photovoltaics and Energy Devices (graduate) *2016-2018*

CORNELL UNIVERSITY

Teaching Assistant, AEP 431 – Computerized Instrumentation Design (undergraduate) *2013-2014*

THE JOHNS HOPKINS UNIVERSITY

Mentor, STEM Achievement in Baltimore Elementary Schools (SABES) *2015–2018*

Skills

Material Characterization: Confocal Microscopy, Electron Microscopy, Atomic-Force Microscopy, Photoelectron Spectroscopy, X-ray Diffractometry, Profilometry, Ellipsometry

Material Deposition and Patterning: Photolithography, Plasma Etching, Wet Etching, Sputtering Deposition, Thermal and E-beam Evaporation, Spin Coating

Electrical Instrument: Source-Meter, Oscilloscope, Capacitance-Voltage Meter, Digital and Analog Circuits

Scientific Simulation: Lumerical FDTD, Zemax OpticalStudio, COMSOL, SCAPS

Software and Programming: C/C++, Python, MATLAB, Mathematica, AutoCAD, SOLIDWORKS, Fusion 360, Microsoft Office, Adobe Creative Cloud

Journal Publication

1. Chiu, A., Rong, E., Bambini, C., **Lin, Yida**, Lu, C. & Thon, S. M. Sulfur-Infused Hole Transport Materials to Overcome Performance-Limiting Transport in Colloidal Quantum Dot Solar Cells. *ACS Energy Letters* **5,** 2897–2904 (Sept. 11, 2020).

2. **Lin, Yida**, Gao, T., Pan, X., Kamenetska, M. & Thon, S. M. Local Defects in Colloidal Quantum Dot Thin Films Measured via Spatially Resolved Multi-Modal Optoelectronic Spectroscopy. *Advanced Materials* **32,** 1906602. ISSN: 1521-4095 (2020).
3. **Lin, Yida**, Ung, G., Qiu, B., Qian, G. & Thon, S. M. Integrated Concentrators for Scalable High-Power Generation from Colloidal Quantum Dot Solar Cells. *ACS Applied Energy Materials* **1,** 2592–2599 (June 25, 2018).
4. Qiu, B., **Lin, Yida**, Arinze, E. S., Chiu, A., Li, L. & Thon, S. M. Photonic Band Engineering in Absorbing Media for Spectrally Selective Optoelectronic Films. *Optics Express* **26,** 26933–26945. ISSN: 1094-4087 (Oct. 15, 2018).
5. Arinze, E. S., Qiu, B., Palmquist, N., Cheng, Y., **Lin, Yida**, Nyirjesy, G., Qian, G. & Thon, S. M. Color-Tuned and Transparent Colloidal Quantum Dot Solar Cells via Optimized Multilayer Interference. *Optics Express* **25,** A101–A112. ISSN: 1094-4087 (Feb. 20, 2017).
6. Ren, J., Li, Y., **Lin, Yida**, Qin, Y., Wu, R., Yang, J., Xiao, Y.-F., Yang, H. & Gong, Q. Spin Hall Effect of Light Reflected from a Magnetic Thin Film. *Applied Physics Letters* **101,** 171103. ISSN: 0003-6951 (Oct. 22, 2012).

Conference Talks

1. **Lin, Yida**, Gao, T., Pan, X., Kamenetska, M. & Thon, S. *Local Defects in Colloidal Quantum Dot Thin Films Measured via Spatially-Resolved Multi-Modal Optoelectronic Spectroscopy* in. 2020 Conference on Lasers and Electro-Optics (CLEO) (Online, May 2020).
2. **Lin, Yida**, Gao, T., Pan, X., Kamenetska, M. & Thon, S. *Local Defects in Colloidal Quantum Dot Thin Films Measured via Spatially-Resolved Multi-Modal Optoelectronic Spectroscopy* in. 2020 American Association for Advances in Functional Materials (Los Angeles, CA, June 2020).
3. **Lin, Yida**, Qiu, B., Arinze, E., Chiu, A., Li, L. & Thon, S. *Photonic Band Engineering in Absorbing Media for Selective Optoelectronic Films* in. 2019 MRS Spring Meeting & Exhibit (Phoenix, Arizona, Apr. 2019).
4. **Lin, Yida**, Ung, G., Qian, G., Qiu, B. & Thon, S. M. *Integrated Concentrators for Scalable High-Power Generation from CQD Solar Cells* in. 2018 Conference on Lasers and Electro-Optics (CLEO) (San Jose, CA, May 2018), 1–2.